Schools of
Mechanical and Chemical Engineering

The University of Adelaide

Investigating the use of Concentrated Solar Energy to Thermally Decompose Limestone

Richard Alexander Craig

Thesis Submitted for the
Degree of Doctorate of Philosophy
May 2010

Chapter 1

Introduction

1.1 Current Environmental Issues

1.1.1 The Greenhouse Effect

Before reaching the Earth's surface, solar radiation passes through clouds and atmosphere, which reflect, scatter, absorb, and transmit various proportions of the electromagnetic spectrum (energy). The Earth's surface reflects some of the incoming solar radiation and absorbs the remainder. As the surface absorbs the energy, it heats and radiates energy back into the atmosphere. When the rates of absorption and radiation are equal (radiative balance) the Earth's temperature is stable. Atmospheric gases like carbon dioxide, water vapour, ozone, methane and nitrous oxide absorb certain frequencies of the electromagnetic spectrum radiated from the Earth's surface which is described in detail by Ledley *et al.* (1999). These gases warm and re-radiate energy back to the surface. In this way, the atmosphere causes the temperature of the earth's surface to be higher than it would be if the Earth did not have an atmosphere. This process is described as the greenhouse effect by many researchers including Augenbraun *et al.* (1999).

The magnitude of the greenhouse effect is defined as the difference between the upward radiation from the Earth's surface and the outward radiation from the atmosphere into space (Ledley *et al.*, 1999). Increases in the concentrations of greenhouse gases will reduce the efficiency with which the Earth's surface radiates to space. More of the outgoing terrestrial radiation from the surface is absorbed by the atmosphere. This results in a positive radiative forcing that tends to warm the lower atmosphere and Earths surface. Because less heat escapes to space, this is described as the enhanced greenhouse effect.

Human activities are increasing the concentration of carbon dioxide and several other greenhouse gases, resulting in concerns about atmospheric warming (IPCC, 2005).

1.1.2 Global Warming

The potential for the enhanced greenhouse effect to significantly change the earth's environment has been hotly debated over the last few decades. However the current debate is only regarding the exact cause, the scale and the rate to which global warming is occurring, not on whether it is occurring. A warmer atmosphere is known to lead to an

increase in the average temperature of the earth's surface and the oceans. A climate change report by the Intergovernmental Panel on Climate Change, (IPCC, 2001b), concluded that an increase of 0.6 ± 0.2°C has already occurred over the 20th century which has caused sea levels to rise by 0.2m. For a range of scenarios developed by the (IPCC, 2000), the global surface air temperature is predicted to warm between 1.4°C to 5.8°C by 2100 relative to 1990, and as a result, average global sea levels are predicted to rise by up to 0.9m. The rate and magnitude of the sea-level rise could easily exceed the capacity for human and natural systems to adapt. Increases in the atmospheric temperature have already affected many physical and biological systems, and further changes are predicted to have enormous ecological impacts in the not too distant future (IPCC, 2001a; IPCC, 2001b).

A special report on the regional impacts of climate change was presented by the IPCC in 1996 to assess the vulnerability and potential impacts of global climate change. The report assesses the vulnerability of natural and social systems of significant ecological and societal regions of the world to climate change. Here vulnerability was defined as the extent to which a natural or social system is susceptible to sustaining damage from climate change. It was found that the Australasian region, due to its relatively low latitude, is particularly vulnerable to adverse climate effects, especially to already scarce water resources and agriculture. The degree of vulnerability was assessed to be moderate to high, with a greatest risk to ecosystems, hydrology, coastal zones, and human health (IPCC, 1996).

In view of negotiations through The United Nations Framework Convention on Climate Change, the market potential for environmental and 'greenhouse friendly' technologies is anticipated to strengthen to reduce the reliance on carbon-based fuels. One of the negotiations, The Kyoto Protocol to the Climate Change Convention sets out legally binding emission targets and timetables for developed countries that have ratified it. In order to ease compliance, it allows countries to achieve their emission targets through the 'Kyoto Mechanisms'. These mechanisms comprise the International Emissions Trading (ET), Joint Implementation (JI), and a Clean Development Mechanism (CDM), which promote investment in renewable energy technologies, thereby making them an economically viable alternative to current energy systems (Wohlgemuth and Missfeldt, 2000). Australia has only recently ratified the Kyoto protocol and therefore greenhouse gas targets have been set. A mandatory minimum renewable energy target required from the energy sector to offset the current emissions of greenhouse gases is required. Therefore, the economic viability of using renewable energy technology within Australia can be expected to increase (Australian Greenhouse Office (A.G.O.), 2001).

1.1.3 Global Emissions of CO_2

Human activities, primarily the burning of fossil fuels and changes to land use and land cover, are increasing the atmospheric concentrations of greenhouse gases, which alter radiative energy balances and lead to a warming of the atmosphere (IPCC, 1995). Carbon dioxide is the main anthropogenic contributor to the greenhouse effect. The Energy sector[1] is responsible for the largest share of World carbon dioxide emissions with 89.3 per cent (or 16,558 million metric tons of carbon dioxide equivalents[2]) in 2004, among the six sectors within the *common reporting format* of Annex 1 Parties (industrialised countries) (UNFCCC, 2006). Figure 1-1 shows the contribution from each of the six sectors: Energy, Industrial processes, Solvents and other product use, Agriculture, Land Use, Land-Use Change and Forestry (LULUCF), and Waste.

The largest contributor of carbon dioxide within the Energy sector is Energy Industries which include stationary power generation. Power generation produced approximately 10,539 million metric tons of carbon dioxide in 2004, which represents 80% to 85% of the global anthropogenic emission of carbon dioxide (Baird, 1997; IPCC, 2005; and World Meteorological Organisation, 2002).

Australia's carbon dioxide emission from power generation for 2004 was a little over 216.7 million tonnes which is 3.5% of the emissions from Annex 1 Parties (Energy Information Administration (E.I.A.), 2006). Although, in absolute terms this is not a large proportion, its relative significance is large, since Australia represents only 0.31% of the world's population (Statistics, 2001). Australia's net greenhouse gas emissions across all sectors totalled 564.7 million tonnes of carbon dioxide equivalent (Mt CO_2-e)[3] in 2004. Australia is one of the world's highest emitters of greenhouse gases per head of population (UNFCCC, 2006).

---

[1] The energy sector is composed of two parts: a) fuel combustion and b) fugitive emissions, within the common reporting format (CRF). The fuel combustion part includes the following components (or sub-sectors): energy industries, manufacturing industries and construction, transport, agriculture, and other. Emissions resulting from fuel use in ships and aircraft engaged in international transport are categorised within 'International Bunkers'.

[2] Greenhouse gases are indexed according to their ability to trap heat in the atmosphere, relative to an equal amount of carbon dioxide. The Global Warming Potential of each greenhouse gas is readily available from the IPCC inventory guidelines.

[3] Carbon dioxide equivalent, CO2-e, provides the basis for comparing the warming effect of different greenhouse gases. See IPCC (1995) or the Australian Greenhouse Office for further details on specifics on calculations.

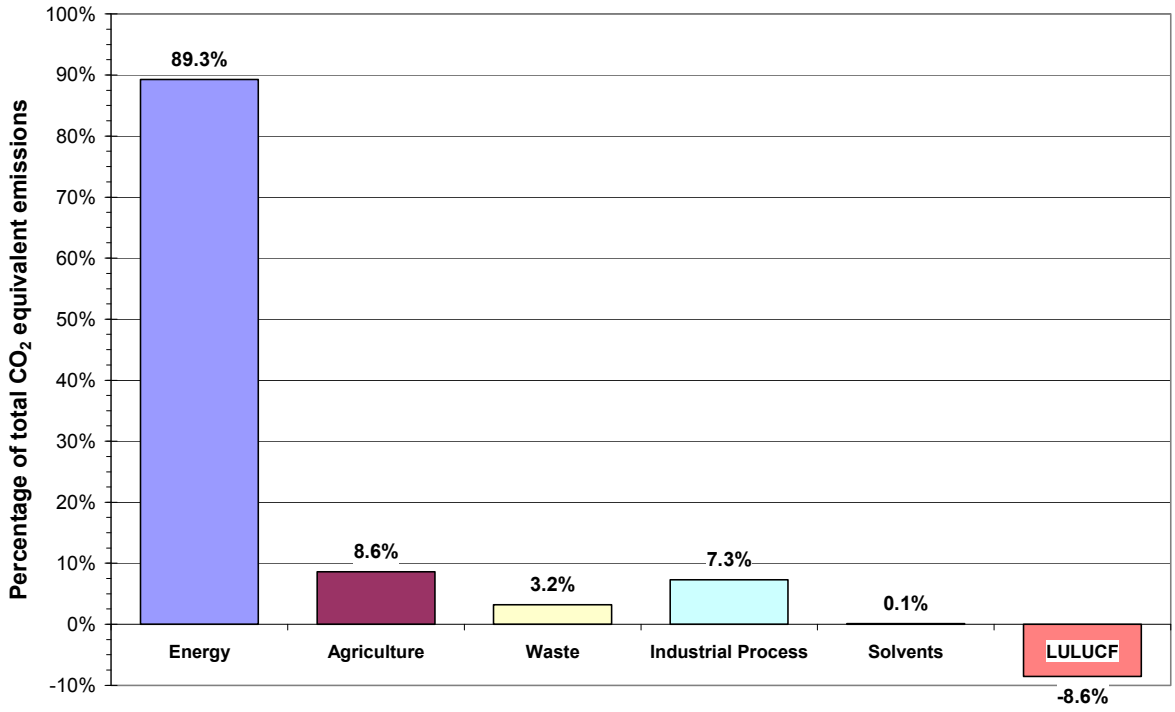

Figure 1-1: Contribution to total CO_2 equivalent emission by sector in 2004.

Source: (UNFCCC, 2006)

1.2 Carbon Sequestration

Predictions by the International Panel on Climate Change (IPCC, 1995) on global energy use in the next century suggest a continued increase in carbon emissions and rising concentrations of CO_2 into the atmosphere unless major changes are made in the way energy is produced and used. The recommendations of scientists to policymakers in the Kyoto Protocol emphasize the immediate need for methods to achieve large-scale decreases in emissions of CO_2 to the atmosphere (Medina *et al*., 2001). Three mutually supporting approaches were identified; the first being to increase the efficiency of primary energy conversion and end use so that fewer units of primary fossil energy are required to provide the same energy service. The second approach is to substitute lower-carbon or carbon-free energy sources for our current sources and the third is carbon sequestration.

Carbon sequestration can be defined as the capture and secure storage of carbon that would otherwise be emitted to or remain in the atmosphere. The idea is to keep carbon emissions produced by human activities from reaching the atmosphere by capturing and diverting them to secure storage, and / or remove carbon from the atmosphere by various means and then store it.

An emphasis has been placed on capture, storage and utilisation of CO_2 from power generation. Capturing and permanently storing CO_2 emissions from fossil-fuel-fired power

plants could provide very large, rapid reductions in carbon emissions and avoid rapid changes away from fossil-fuel-based energy infrastructure (International Energy Agency (I.E.A.), 2000). A research and development study by the I.E.A. reported in 2001 estimated that a new 500-Megawatt natural gas- or coal-fired power plant incorporating CO_2 capture could achieve an 80% reduction in CO_2 emissions to the atmosphere.

Before carbon dioxide gas can be sequestered from power plants or industrial sources, it must be captured as a relatively pure gas. The objective of CO_2 capture is to produce a concentrated stream of CO_2, at high pressure that can then readily be transported to a storage site. Depending on the process, fuel and power plant application, the most likely options identified within a report by the U.S. Department of Energy (1999), as viable CO_2 separation and capture systems include:

- Chemical and physical absorption
- Low-temperature distillation
- Gas-separation membranes
- Mineralisation and bio-mineralisation
- Vegetation absorption and sequestering

Currently, several CO_2 separation and capture plants use one or more of these methods to produce CO_2 for commercial markets. The CO_2 capture options can be used in association with each other as pre- and/or post- combustion system processes. The technology required for pre-combustion capture is widely applied in fertilizer manufacturing and in hydrogen production. Although the initial fuel conversion steps of pre-combustion are more elaborate and costly, the higher concentrations of CO_2 in the gas stream and the higher pressure obtained make the separation easier (IPCC, 2005). Post-combustion CO_2 capture technology is routinely used within industrial processes such as synthetic ammonia production, hydrogen production, and limestone calcination. All of these carbon capture and storage / sequestration options consume energy which increases production cost and further adds to the production of greenhouse gases (U.S. Department of Energy, 1999; and IPCC 2005).

1.2.1 Carbon Sequestration via Mineral Carbonation

One method (among many) being proposed to accomplish CO_2 separation from combustion gases is lime, i.e. CaO, which will be carbonated to form calcium carbonate, $CaCO_3$ at a relatively low flue gas temperature. The $CaCO_3$ can then be removed from the combustion flue gas stream (carbonator) vessel, and decomposed in a separate (cracker) vessel at the higher calcination temperature. The relatively pure and concentrated CO_2 collected within

the cracker vessel can then be compressed and sequestered as desired. The regenerated lime would be returned to the carbonator for further CO_2 collection.

This circular CO_2 collection system requires an appropriate energy source which can supply temperatures high enough for the calcination reaction to occur. The purity of the CO_2 gas within the cracker depends upon the type, and the method of delivery, of the energy required within the calcination cracker vessel. Particular advantages and disadvantages of different lime kilns (cracker vessels) and energy supply systems are discussed within Sections 1.4 and 1.5.

Mineral sequestration does have three advantages over other combustion flue gas scrubbing processes; the first is that carbonates have a lower energy state than CO_2. Therefore the process theoretically requires no energy inputs, and could actually produce energy. The second advantage is that the raw materials are relatively abundant and do not degrade over time. So if the raw limestone material is not available locally, it could be readily transported without special considerations. The final advantage is that the CO_2 sequestration could be relatively permanent. Transportation of the sequestered CO_2 is simple and devoid of leakage concerns that could pose environmental, health or safety risks (Herzog, 2002). The lime kiln (cracker vessel) could therefore be located external to the power station.

1.3 The Thermal Decomposition of Limestone

The production of lime involves the thermal dissociation (or decomposition) of calcium carbonate ($CaCO_3$, limestone) to produce calcium oxide (CaO, quicklime or 'lime') and carbon dioxide (CO_2). On a molar basis, the reversible reaction describing this process has the form:

$$\underset{100g}{CaCO_3} + \text{Heat} \Leftrightarrow \underset{56g}{CaO} + \underset{44g}{CO_2}$$

The theoretical amount of heat required is approximately 3010 kJ per kg of CaO produced, at a calcination temperature of approximately 898°C and one atmosphere of pressure of CO_2 (Oates, 1998). On a mass basis, 1 kg of CaO is produced from 1.786 kg of $CaCO_3$ with 0.786 kg of CO_2 being released. Recarbonation readily occurs when the CaO is below the disassociation temperature and above 400°C or if the partial pressure of CO_2 is high enough (refer to Figure 2-2). Percentage of recarbonation varies depending on particle size and porosity of quicklime, with greater CO_2 absorption occurring in the smaller particles and the more porous quicklime (Boynton, 1966, pg 191).

To produce the heat required, typically fuels are burnt within the vicinity of the limestone. The fuels used in modern lime producing plants are mostly pulverised coal, coke, fuel oil and natural gas (Boynton, 1980). The type of fuel used has usually been determined by the type of kiln (or furnace[4]) used, but owing to fuel availability, and cost considerations, a large proportion of kilns can now burn more than one fuel type (Schwarzkopf, 1970; Simonsen and Azarniouch, 1987).

1.4 Conventional Lime Kilns

A very large variety of techniques and kiln designs have been used over the centuries and around the world. Lime kilns fall into two basic categories which are based on the type of the calcination process; either intermittent or continuous feed kilns. The choice for process is usually based on the quantity of product required and or the availability and type of fuel (Oates, 1998). Most intermittent kilns are thermally inefficient because there is little heat recovery within the preheating and cooling zones. Continuous kilns, on the other hand, provide considerably improved thermal efficiencies and improved product consistency because of the ability to monitor lime quality and adjust the fuel input accordingly.

Continuous lime kilns can be classified into three general groups, the vertical kiln, the rotary kiln, and miscellaneous kilns. Within each type, there are literally hundreds of different forms, each kiln being slightly different from another. Boynton, (1980) states that no two kilns are exactly the same, even if constructed on the same site. Figures 1-2 and 1-3 provide cross sectional representations of a vertical shaft kiln and a rotary kiln respectively. These two types of kilns are most commonly found within industry, often at the same location, so that the lime producers can make full use of all grades of quarried limestone, and also produce a range of lime grades and qualities to meet the variety of market demands (Oates, 1998). Figures 1-4 and 1-5 are early conceptual drawings of a flash calciner and a Calcimatic kiln, respectively. Common to all modern kilns are preheating, calcination and cooler / heat recovery sections, which help improve the thermal efficiency and therefore reduce fuel consumption.

The calcination of limestone using the most modern combustion driven kiln processes produce relatively large volumes of exhaust gases (e.g. 3500 to 4000 Nm^3 per tonne lime)[5]

[4] The terms kiln and furnace are interchangeable, within this document. The term furnace will be used when referring to solar applications and the term kiln for combustion applications.

[5] the N term is an abbreviation of norm or normal. Normal, in this connection, means a temperature of 0 degrees Celsius and a pressure of 1.013 bar, the conditions at which one mole of an ideal gas has a volume of 22.413837 litres.

which includes almost 1 tonne of CO_2 per metric tonne of quicklime product (Oates, 1998). That is, 786 kg of CO_2 derived from the thermal decomposition reaction and between 200 kg to 450 kg of CO_2 (depending on composition and calorific value of the fuel and the specific heat consumption of the kiln) derived from the combustion of fuel (Oates, 1998) pp 391, (Imhof, 1997). Generally, the amount of CO_2 released is dependent on the age of the kiln, the thermal efficiency of the kiln system, and the type of fuel being used. Modern technology has substantially increased efficiency thereby reducing the total amount of fuel burnt and subsequently the emissions released (Jenkins, 1990). Nevertheless, on a global scale, the limestone and cement industries contributed approximately 1008 million metric tonnes of the anthropogenic carbon dioxide per annum (Marland *et al.*, 2006)[6]. Within Australia the 2004 figure was 5.5 million metric tonnes of carbon dioxide (Australian Greenhouse Office (A.G.O.), 2006). Cement clinker contributed 3.5 Mt (63.2%) of mineral product subsector emissions and lime contributed 1.1 Mt (19.7%). Limestone and dolomite use generated 0.9 Mt (17.2%) of emissions from the mineral products subsector of the Industrial Process sector. Net emissions from mineral products increased by 0.5 Mt (9.2%) from 1990 to 2004 due to increased production of lime, (Australian Greenhouse Office (A.G.O.), 2006).

The cost of fuel dominates the manufacturing cost for a thermal mineral processing system. Figures of 40% to 75% of the total production costs of mineral products have been attributed to the cost of fuel (Oates, 1998). Furthermore, fossil fuel prices are expected to increase further as the abundance of deposits are reduced and total reserves are decreased, in addition to increases in costs of exploration (Energy Information Administration (E.I.A.), 1998). At the same time, alternative energy sources will become increasingly more viable as economies of scale take effect (Wohlgemuth and Missfeldt, 2000).

[6] Emissions of CO_2 from cement production equals the amount of CO_2 created by the conversion of calcium carbonate to calcium oxide inside the kiln plus the amount of CO_2 created by burning large quantities of carboneous fuels to heat the kilns to the 1450°C necessary for clinker production. The annual estimates of CO_2 emissions from cement production have been derived from energy statistics published by the United Nations and the cement production estimates by the U.S. Department of Interior's Bureau of Mines. These estimations were calculated using the methods of Marland, (2001).

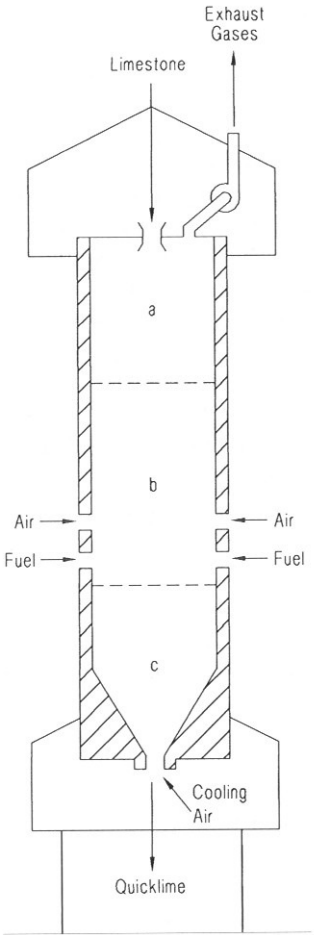

Source: Oates (1998)

Figure 1-2: Cross-section of a continuous vertical shaft kiln.

Section (a): preheater; Section (b): calcination zone; Section (c): cooler and heat recovery.

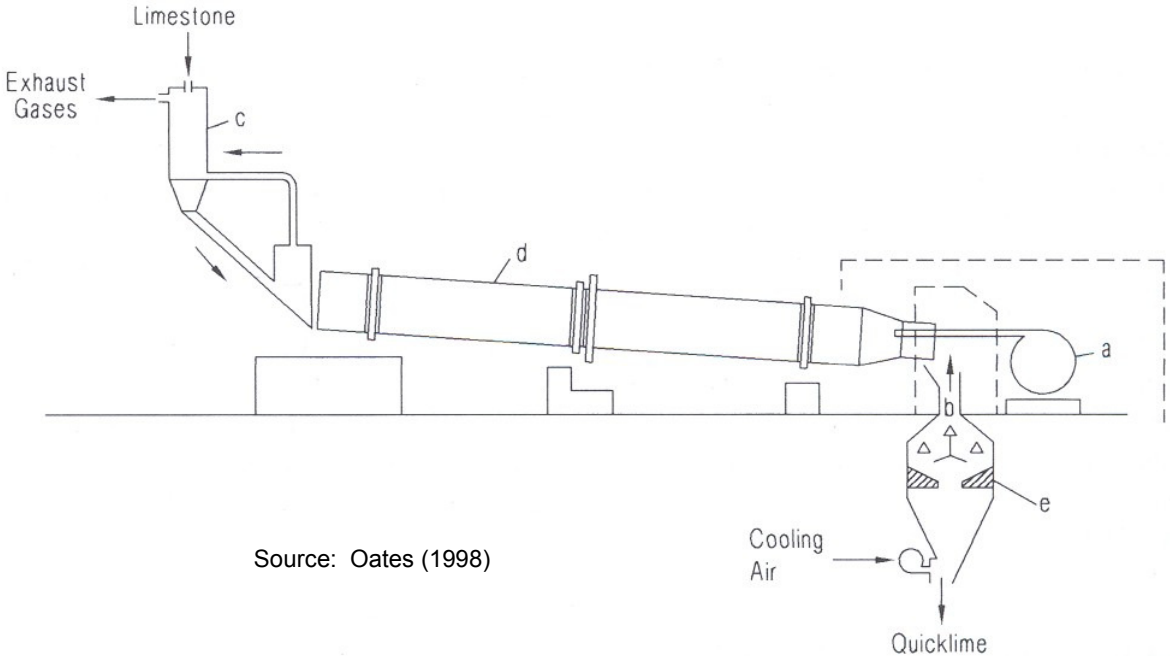

Source: Oates (1998)

Figure 1-3: Cross-section of a preheater short rotary kiln.

(a) fuel and primary air; (b) preheated secondary air; (c) preheater; (d) rotary kiln; (e) cooler

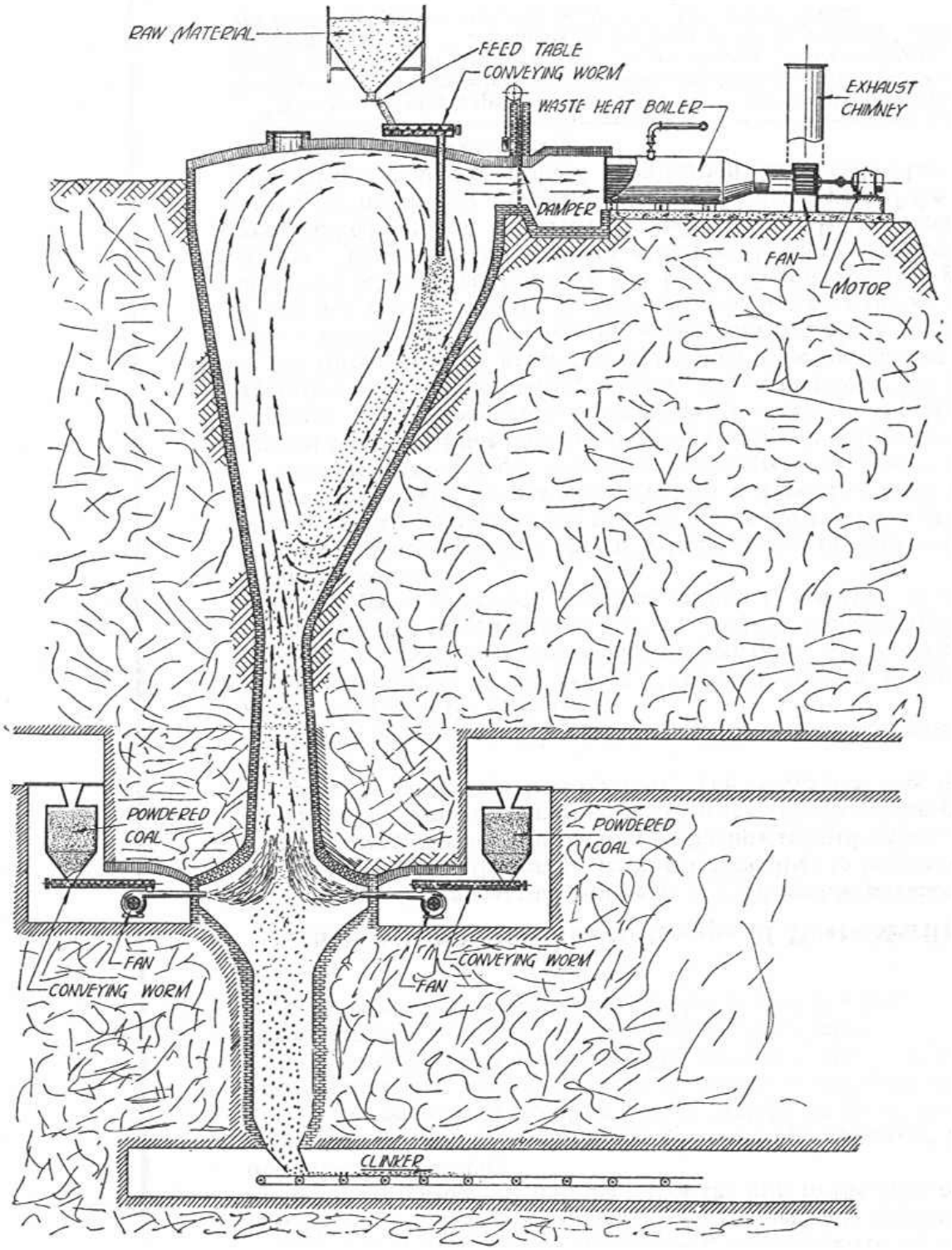

Figure 1-4: An early conceptual design of a flash calciner (floatation kiln).

Source: Martin (1932, pg 28.17)

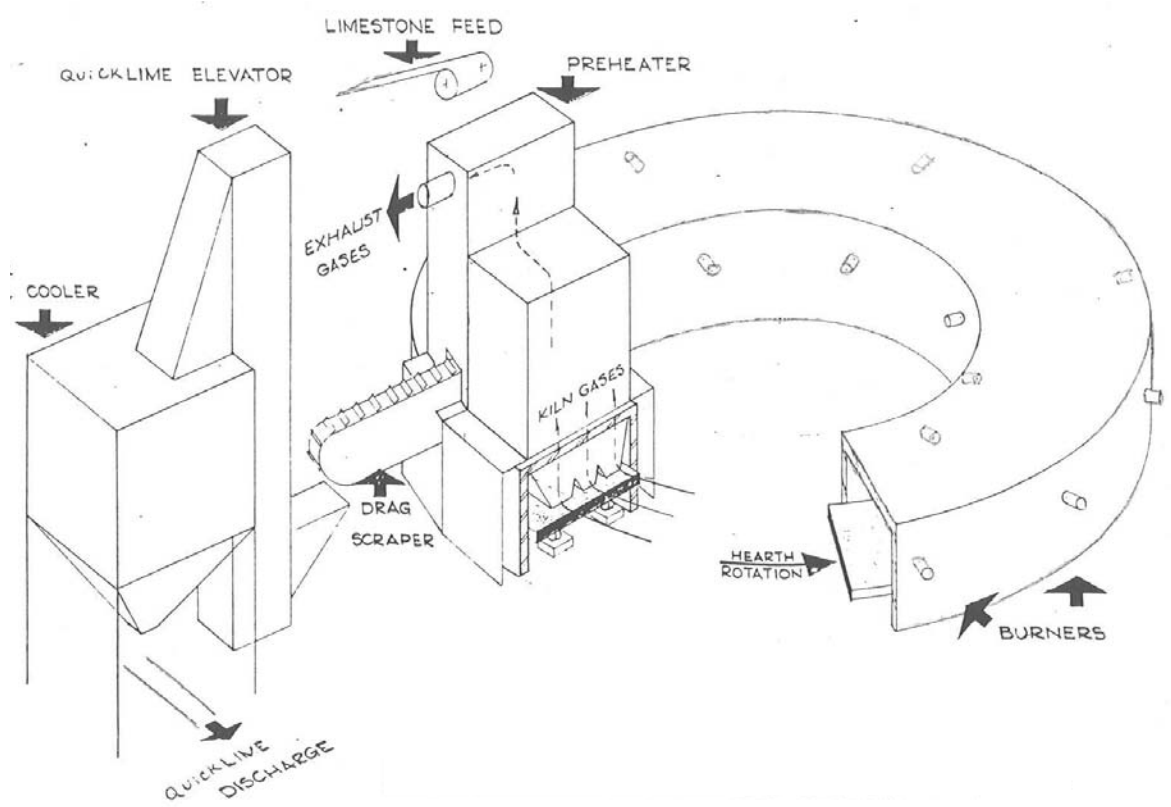

Figure 1-5: A conceptual diagram of a rotating Calcimatic kiln.

Source: Oates (2001)

1.5 The Use of Alternative Energy for Lime Manufacture

Wingate, (1985) points out that the majority of early (pre 1900) lime production kilns were fired using wood or coal, with peat occasionally used. Mason *et al*. (1999) then describe how the industrial age brought advancements in kiln technology with the creation of specialised burners capable of burning either oil, gas and pulverised coal. These conventional fuels have relatively high energy density providing so-called high-grade heat, but as a drawback, produce CO_2 (among other greenhouse gases) when burnt. Owing to the high temperature requirements of the lime burning thermal process, the use of alternative energies for the replacement of fossil fuels is limited.

Two possible forms of alternative energy that could be used for lime manufacture and do not involve fossil fuel combustion were identified by Wentworth and Chen (176) and Wingate (1985), they are electrical energy obtained from nuclear power, and electrical or thermal power sources derived from solar, wave or wind energy. It is extremely unlikely that the electrical power generated using nuclear technology would be cheap enough to make lime burning economical. In addition, supplying thermal energy from nuclear power is a highly complex process requiring close proximity, a highly skilled workforce, and significant

infrastructure. Not to mention the many social issues associated with nuclear power. For these reasons nuclear power is not considered to be a viable alternative energy source for this application.

From the viewpoint of availability of natural resources, the use of solar energy appears very attractive. Solar derived energy follows two paths from the source to the end-use: direct (radiant energy), or indirect (including wind, hydro, wave, tidal, thermal, the biomass cycle and photovoltaic (P.V)).

The indirect path includes one of the more attractive alternatives, biomass. Hall and Scrase (1998) define biomass as “unique”, in that it can provide solid, liquid and gaseous fuels, which can be stored and transported. Biomass can be used as a co-firing fuel or a direct replacement to conventional fuels. It has similar physical characteristics and reasonably similar calorific values to a general-purpose coal, biomass being 17 to 20 MJ/kg (0% water) and bituminous coal 17 to 24 MJ/kg, (Johnson and Auth, 1951; Spitzer, 2001). Typically every tonne of dry biomass directly fired in replacement of a fossil fuel, reduces net CO_2 emissions by just over 1 tonne (Tillman, 2000). It would therefore seem that biomass is an ideal alternative energy source, but it also has numerous short comings. Yamamoto *et al*. (2001) discuss one of the major limitations of biomass, in that it needs somewhere to grow, and so competition for land use becomes a dominant feature of the economic viability of using these fuels. In the past, wood was extensively used, but resulted in widespread deforestation, for example the Burra region of South Australia where wood was used to fuel boilers associated with a copper mine. Another consideration is availability and supply, since there are typically seasonal variations in supply. Additional concerns brought to light by Borjesson (1996) and Hall and Scrase (1998) include those of mono cropping and disease, residue disposal, crop rotation rates, transportation costs and energy consumption. Spitzer (2001) describes that due to these concerns, energy content of biomass and considering available land, the global supply energy from biomass will only ever contribute 15 to 30% of the total required supply. Therefore biomass may be a viable energy alternative in certain regions where plant growth can be sustained. For other regions where this is not possible, other alternative energy sources must be found.

The other indirect energy paths usually result in the production of electrical energy for the end use (Renewable Energy Centre, 2000). Each step of the indirect path from the sun to the supply of electrical energy results in conversion losses that cause the net efficiency of the process to decrease. It is, of course, desirable to minimise the number of energy conversion steps between collection and utilisation. Owing to the size of these losses the use of electrical heating for the calcination of limestone has never been commercially viable.

Typical efficiencies of conversion from solar energy to electrical energy are hard to determine due to the number of different conversion technologies methods used, with equal analysis even more difficult to achieve (Hesse, 2002). Even still, typical conversion values for several indirect solar energy systems range between 10% - 25% for P.V. and wave power, 15% to 25% for solar thermal electric power, 20 to 45% for biomass combustion (depending upon moisture content), 35% to 40% for wind, and up to 90% for hydro energy to electrical conversion (The Australian Cooperative Research Centre for Renewable Energy (A.C.R.C.R.E), 2002; Foundation for Alternative Energy, 1998; Global Energy Concepts, 1995; Pimentel *et al*., 1994; U.S. Department of Energy, 2002; and Weins, 2002). It is therefore desirable to minimise the number of energy conversion steps between collection and utilisation. At the utilisation stage, numerous electrical radiant heaters would be required as the heating elements. These elements are typically very energy intensive. At best, it is estimated that an electrical thermal system could provide only about 20% of the primary energy to the thermal chemical process when considering the total efficiencies of conversion from solar energy to electrical energy and then to final thermal input. Other factors which also need consideration include:

- The economics of using electrical energy for such a 'low value' commodity.
- The distance the lime manufacturing plant is from the solar derived electrical power station considering transmission and distribution losses.
- The guaranteed continual supply of the solar derived electricity.
- The surface area of photovoltaic cells required to achieve the required power.
- The life cycle and productivity of the lime manufacturing plant.
- General environmental considerations associated with the particular planned manufacturing region (U.S. Department of Energy, 2002).

For these reasons electrical heating systems are not currently used for the thermal calcination of limestone within lime producing industries.

From the viewpoint of direct usage and availability of natural resource, the use of solar energy appears very attractive. This is the direct utilisation of concentrated solar radiation as the source of high-temperature process heat. The average daily irradiation on a horizontal surface exposed to solar radiation is between 3 kWh/m^2 (10.8 MJ/m^2) and 6 kWh/m^2 (21.6 MJ/m^2) for any month of the year within most regions of Australia (Renewable Energy Centre, 2000). The amount of solar energy that can be collected is only restricted by the size of the collection area. Currently, solar concentrator systems can achieve radiation flux densities greater than 2 MW/m^2, with process heat above 1500K (Schubnell *et al*., 1991; Steinfeld and Palumbo, 2001). The optimum temperature for a solar receiver is 1500K for a

concentration of 5000 giving a maximum theoretical efficiency of 75 % (Steinfeld and Epstein, 2001). Temperatures well above this process temperature are theoretically achievable, as seen in Figure 1-6, but limitations on concentrator construction material currently exist (SolarPaces, 2001).

NOTE:
This figure is included on page 14 of the print copy of the thesis held in the University of Adelaide Library.

Figure 1-6: Variation of concentrator type with concentration ratio and equilibrium temperatures for earth and space.

Source: Baumeister *et al*. (1996).

There are, of course, availability and consistency issues associated with using concentrated solar radiation. Villermaux (1979) notes that the solar furnace design needs to account for the dynamic thermal input of solar energy on a second-by-second time scale as well as on the daily insolation period. There is therefore a balance between having enough thermal mass to maintain a consistent thermal input and minimising thermal mass to reduce heat up time. The selection of solar reactor construction material is therefore paramount to the life and effectiveness of the system.

For continuous production processing, or on days of reduced solar availability, a supplementary dual process heating system such as an oxy-fuel burner may be desired.

1.6 CO_2 Mitigation using Solar Lime Manufacture

By replacing fossil fuels with concentrated solar energy as the primary energy source, the CO_2 derived from combustion is completely eliminated from the exhaust gas stream. Other fuel constituents, including sulphur and nitrogen would not be present thereby eliminating additional greenhouse gas emissions. At the same time the stoichiometric and excess air required for combustion are no longer required, making it theoretically possible to have a homogeneous carbon dioxide furnace atmosphere. With a fairly pure carbon dioxide atmosphere there is a substantial increase in the cost-effectiveness of collecting the CO_2 for either sequestering, storage or utilisation.

To enhance the effectiveness of the concentrated solar radiation within a solar furnace it is desirable to maintain an optically thin atmosphere within the furnace. It is well known that molecules of water, carbon dioxide and dust absorb solar radiation. A proportion of this absorbed energy will be unavailable for the calcination process and potentially lost from the system. Therefore it is advantageous to minimise the presence of these molecules and dust within the furnace. Preheating the limestone above 100°C before it is fed into the furnace dries the limestone and reduces the presence of water within the furnace enclosure. Carbon dioxide will always be present because it is an element of the calcination reaction and therefore its presence can not be controlled without diluting it, which is not desirable from the capture / collection point of view. Lastly to reduce or eliminate dust formation, the movement of the limestone (and quicklime product) needs to be minimised. This means reducing the amount of rotating, tumbling and falling the stone experiences within the furnace. Reducing the turning of the stone could also provide a decrease in the use of electrical energy and therefore a total reduction in energy usage and environmental impact (footprint) of the lime manufacturing plant.

However there are also some obvious drawbacks with using direct solar radiation, a few of them being the intermittent nature of solar energy, its unpredictability due to cloud cover, dust and pollution, and the number of useful hours that the energy can be collected. The number of usable solar radiation hours within a standard 12hr light, 12hr dark day is estimated to be between 6 to 8hrs under clear skies (Liu and Jordan, 1960; Vardavas and Cannon, 1989). This is due to the elevation and azimuth angle of the sun, and therefore the increased solar radiation path length through the atmosphere and thus increased absorption of the radiation by the atmospheric gases. Other considerations include the uneven distribution of solar energy over the Earths surface, with a dominant ‘sun belt’ falling between 30° north and 30° south of the equator (Imhof, 1997; Imhof, 2000). Also the peak solar

radiation heat fluxes are relatively dilute, being a maximum of approximately 1kW/m^2 at sea level, therefore some type of energy concentration system is required to make it useful for thermal chemistry (Steinfeld and Palumbo, 2001)

Steinfeld and Palumbo (2001) also state that with adequate collection and concentration, solar radiation could provide extensive amounts of energy for use within thermal processing, as seen from the various concentrator systems in Figure 1-6. The proposed research will not assess the pros and cons of using solar energy, but will provide suitable techniques by which its use can be facilitated. The direct use of concentrated solar radiation for use in the calcination of limestone will be considered within this research.

1.7 Scope and Structure of Thesis

Calcination of limestone using a conventional combustion driven lime kiln produces around 1 tonne of CO_2 per tonne of quicklime product. Carbon dioxide emissions could be reduced by more than one third by replacing fossil fuels with concentrated solar energy as the primary energy source. In addition, if solar energy is used and the lime manufacturing system does not use process air for heat recovery, industrially pure carbon dioxide from the calcination reaction could be captured and utilised or sequestered more efficiently. To achieve this, the solar furnace design would consist of an enclosed calcination 'chamber' into which concentrated solar radiation can be delivered and the evolved CO_2 gas stream can be collected.

The present investigation seeks to assess issues regarding the technical viability of a proposed solar thermal minerals processing technology to help reduce the atmospheric release of carbon dioxide. The project will research key elements relating to the design of a solar furnace system which will use concentrated solar radiation as the exclusive energy source, for the thermal dissociation of limestone. In doing so, a reduction in the production and release of carbon dioxide is sought.

The development of a conceptual design for a thermally viable solar furnace is therefore one of the primary objectives of this research. Using first principals, a furnace design, which considers the main thermodynamic principles used within a solar lime furnaces, has been conducted. The proposed design description will take into account the heat transfer processes, the mineral flow and movement, the furnace atmosphere, as well as the calcination of the limestone within the furnace. This thesis reports the furnace design and

then investigates some of the key issues in using concentrated solar radiation for the thermal decomposition of limestone.

1.7.1 Thesis Structure

This thesis is divided into 11 Chapters. An extensive literature review on the use of solar energy for thermochemical reactions is presented in Chapter 2. This chapter provides a knowledge base from which the current studies originate, and then identifies the aims and objectives of the current project.

Chapter 3 presents an investigation of the theoretical energy requirements for quicklime production. A mathematical zero-dimensional zone model is then used for evaluating cross sectional shapes for the proposed solar furnace.

Details of the experimental apparatus used for the experimental investigations are presented in Chapter 4. This includes sample preparation methods, the solar simulator apparatus, the equipment used for the open atmosphere calcination experiments, and the solar lime furnace system.

Chapter 5 describes how heat flux transducers and digital imagery were used for the measurement of the high intensity radiant heat flux. It also describes the calibration processes used to ensure consistent measurements. The chapter includes a detailed error analysis of the heat flux measurement technique.

A detailed experimental campaign is then presented in Chapters 6 which describes the calcination experiments conducted within an electric muffle furnace. These initial experiments provide baseline calcination rate values for comparison with the solar calcination experiments presented in Chapters 7 and 8. They also identify a limestone bed thickness which optimises the calcination rate for the small to medium sized marble.

Chapter 7 discusses the open solar system experiments and the effects of radiation intensity on the calcination rates for three different sized limestone samples.

Enclosed solar furnace calcination experiments are then presented in Chapter 8. The effects of the furnace walls, the size of the limestone and the radiation intensity have on the calcination rate are discussed.

A multi-zone two-dimensional thermal radiation zonal model is then presented within Chapter 9. The model simulates the radiant heat exchange within the solar furnace. Validation of the modelling is through comparison with the experimental measurements in Chapter 5.

A theoretical calcination model is presented in Chapter 10 which calculates the preheating times and calcination rates for various sized limestone exposed to various radiant heat fluxes within either an open solar system or a solar furnace. The results are compared with the experimental results from Chapter 7 and 8.

Chapter 11 draws together the thesis with the overall conclusions from the research as well as providing appropriate suggestions and recommendations for further investigations.

Chapter 2

Literature Review

2.1 Introduction

To effectively utilise solar radiation within a solar lime kiln, its design must be optimised for radiant energy transfer. The kiln needs to accommodate the inflow of limestone feed, minimise heat losses, as well as provide good heat transfer to the limestone for the thermochemical decomposition reaction. This chapter presents an overview of the issues and mechanisms that have been identified as technical constraints to a successful commercial solar lime manufacturing system.

The chapter begins with a comprehensive discussion and analysis of the mechanisms and kinetics of the calcination process, and how best to represent these processes within a mathematical model. This provides a foundation from which to discuss the technical viability of commercial solar lime manufacture. Following this, the mathematical methods used to design and analyse different kilns and the methods for optimising furnace designs are discussed. Finally, the main findings from the literature review are discussed, and areas requiring further investigation are identified. The specific objectives of this research investigation are then presented.

2.2 Limestone

Calcium is the fifth most common element in the earth's crust, at about 3 - 4 % by mass, after oxygen, silicon, aluminium and iron, as provided by Boynton (1966) and Schwarzkopf (1974). Calcium carbonate ($CaCO_3$), the principle constituent of limestone, is the most abundant form of calcium. Limestone is therefore a plentiful raw material, but is very inconsistent in purity. The most common impurities within limestone are silica and alumina, which Oates (1998) says occur in varying amounts depending upon the location of the deposit. Boynton (1980) adds that its colour, texture and crystallinity can vary radically due to impurities between seemingly similar 'seams'. There have therefore been hundreds of different types of limestone identified, each with similar characteristics but varying constituents. One of the most widely admired forms of limestone is marble, which is a highly crystalline metamorphic limestone in which impurity infiltration causes the different colours. Limestone is therefore a very broad term. Operators of conventional lime plants chose their location carefully to

ensure the deposit is suitable for production of good quality lime. Similar constraints will apply to a solar lime plant.

There are two major processes by which limestone is formed:

- Chemically (inorganic) ~ direct precipitation (or crystallisation) from solution; and
- Organically ~ skeletons of animal and vegetable organisms.

Most commercially viable deposits are organic in origin.

Limestone is generally classified into the three types. These are characterised by the presence of carbonate minerals (exclusive of impurities), and physical characteristics. The limestone types are:

(1) **High calcium**, $CaCO_3$: in which the calcium carbonates content is either from Calcite or Argonite; contains no more, and usually less than 5% magnesium carbonate; it may be colourless or white, but is often tinted with impurities.
(2) **Magnesian**, $MgCO_3$: contains both calcium and magnesium carbonates, and has a magnesium carbonate content of 5 – 20%; usually white, tan or brown
(3) **Dolomitic**, $CaMg(CO_3)_2$: contains >20% but not more than 45.6% $MgCO_3$, the exact amount contained in a true, pure, equimolecular dolomite. The balance is $CaCO_3$; usually colourless, but often coloured pink or tan.

High calcium calcite is easily the most abundant of these types, and is the focus of the present research.

2.2.1 Lime

Lime is produced by the thermal dissociation of limestone. The names limestone and lime are often wrongly interchanged due to the number of different industries using the minerals. Lime is commonly known as quicklime, burnt lime, live lime, caustic lime, or un-slaked lime. The term quicklime as described by Francis (1998) results from the fact that when lime is exposed to water, it grows hot and swells (as if alive) - and is derived from the old meaning of the phrase "to quicken - to be alive".

The physical and chemical properties of lime vary considerably depending upon the limestone from which it was derived. Lime derived from the calcination of high calcium calcite is the focus of this research.

2.2.2 Uses for Limestone and Lime

The use of limestone dates back to the Stone Age, where it's usage as a fire surround would have undoubtedly led to the discovery of lime. A report by Bennett (1997) details that one of the earliest surviving examples of the use of lime dates back to between 9000 and 8000 B.C. where it was used as a concrete for the floor of a fisherman cottage on the banks of the Euphrates River. By about 1000 B.C. its use was prevalent in many civilisations including Greeks, Egyptians, Romans, Incas, Mayas, Chinese and Mogul Indians which is discussed by Oates (1998). Its usage was recorded within the Egyptian dynasty when limestone was employed in the construction of the Giza Pyramids. Oates (1998) continues discussing how the Romans were using limestone for road construction, while the Greeks were using marble for building fascia decorations and statues. Since then the usage of both limestone and lime has grown considerably with limestone currently being classified by Mason *et al*. (1999) and Boynton (1980) as one of the world's most useful industrial chemicals. In fact Page 1 of Boynton (1980) lists lime and limestone as among the six most useful basic materials on which industry revolves. He reports that limestone is the mainstay of the construction industry, as well as playing an instrumental role in chemical and metallurgical production, for water treatment in tailings and many other industrial uses.

The largest market segments, identified by the Australian Greenhouse Office (2001), for the sale of limestone are the construction and manufacturing industries. The manufacture of cement and steel are easily the largest consumers within these groups. Within the many thermal industrial processes, like cement manufacture, lime is required within the final product. The raw feed therefore contains limestone, which is calcined during the thermal process. Boynton (1966) discusses how lime is the most widely used and least expensive alkali available and is therefore considered to play a significant roll in many industrial processes. A more detailed review of the use of limestone and lime within industry can be found in numerous publications such as Boynton (1980), Wingate (1985), Freas (1990), Gutschick (1995), Oates (1998), and Miller (2000).

The annual global use of limestone in 1990 was estimated to be $2{,}000 \times 10^6$ metric tonnes by Gutschick (1995). A more updated estimate of the global usage of limestone was $4{,}500 \times 10^6$ metric tonnes in 1998 by Oates (1998). It should be stated that an exact figure for the usage of limestone is not possible due to the large amount of mining and use within remote and regional areas and therefore not being 'registered' on official census.

The Australian Bureau of Statistics (document 8414.0) estimated the production of limestone in Australia over the census year 1998 – 99 to be approximately 80.36 million tonnes (which

includes 64.22 million litres of hydrated lime, used as flux). Within this same period, the South Australian production rate was 2.3 million tonnes. The following year period 1999-00, industrial and agricultural limestone production in South Australia totalled 2.6 million tonnes as reported in Primary Industries and Resources of South Australia (2001). This report also states that limestone, as a raw mineral, accounted for 53.59% of the industrial minerals mined in South Australia in 2000.

2.3 Mechanisms and Kinetics of Calcination

The calcination reaction is described by Boynton (1966) as being one of the most basic and simplest of all chemical reactions, but is certainly not completely understood. The present section discusses the mechanisms required for the calcination to proceed. This includes the chemical kinetics which are required to achieve full calcination, the rate at which the calcination occurs and the effects of carbon dioxide on that rate.

The thermal dissociation (or decomposition) of calcium carbonate ($CaCO_3$, limestone) produces calcium oxide (CaO, quicklime or 'lime') and carbon dioxide (CO_2). On a molar basis, the reversible reaction describing this process has the form:

$$\underset{100g}{CaCO_3} + Heat \Leftrightarrow \underset{56g}{CaO} + \underset{44g}{CO_2} \qquad [2.1]$$

The forward reaction (driving the equation to the product forming side, right) is called calcination, where as the backward reaction is called recarbonation. The temperature required for the calcination to take place is thought by Oates (1998) to be 898°C at one atmosphere pressure of CO_2. However this temperature is not absolute and has been redefined many times, because it depends on the test method used and purity of the limestone under analysis. A figure of 900°C (± 2°C) is generally accepted as a good average value amongst many researchers such as Martin (1932), Schwarzkopf (1974), Boynton (1980), Wingate (1985), Oates (1998), and Mason *et al*. (1999), and therefore 900°C will be used as the theoretical temperature of calcination for the present research. Because the calcination temperature is unique for each limestone deposit, experimentation is used to verify the exact temperature range.

On a mass basis, 1 kg of CaO is produced from 1.786 kg of $CaCO_3$ with 0.786 kg of CO_2 being released.

The two mechanisms that drive the reaction, Equation 2.1, to the right are:

1. energy in the form of heat, and
2. the removal of carbon dioxide from the reaction zone.

The calcination reaction is highly endothermic, with Oates (1998) stating that a theoretical heat of approximately 1686 kJ per kg of $CaCO_3$, at 900°C and 1 atmosphere CO_2 is required. There is significant scatter in the values reported by different researchers for the exact value for the theoretical heat of dissociation. The current range of values are from 2819 kJ to 3054 kJ per kilogram of product (CaO) formed as reported by Martin (1932) and Boynton (1966) respectively. The present study uses one of the more recent investigations, that by Oates, (1998), who cites 3010 kJ per kg of CaO at 900°C. This value has been chosen for several reasons; the first being that it is on the conservative side of the range and therefore any design using this value will provide sufficient heat. The second is that Oates has four decades of experience within the limestone industry, and lastly because the value is one of the most recent.

The total theoretical heat (sensible and chemical) required for calcination at 25°C is 3182 kJ per kg of CaO produced (about 0.883 MWh/tonne). The 172 kJ difference (3182 – 3010 kJ / kg of CaO) in the heat of dissociation between 25°C and 900°C comes from the sensible heat, which is 1801.7 kJ to raise the temperature of 1.786 kg of $CaCO_3$ from 25°C to 900°C. Whereas from the reaction products, 1.000 kg of CaO and 0.786 kg of CO_2 release 863.6 kJ and 765.5 kJ respectively during cooling from 900°C to 25°C. Assuming that all of this energy is recovered, the difference equates to 1801.7 – 1629.1 = 172.6 kJ/kg of CaO.

Figure 2-1 was calculated using Equation [2.2] to verify the theoretical heat required for the calcination reaction.

$$Q = -RT^2 \times \frac{d \log_e P_V}{dT} \qquad [2.2]$$

Source: Martin (1932, pg 8.2)

The resulting values depend on the characteristics of limestone under investigation, with the trend providing a reliable and insightful representation. It can be seen that the theoretical calcination energy reduces as the temperature of the initial $CaCO_3$ (limestone) increases. The energy recovered from cooling the product and CO_2, increases with increasing temperature, so that at 3000K the recovered energy equals the amount required for calcination. Realistically, this temperature could not be obtained without damaging the

quality of the product. These issues are important when preheating the stone and are discussed further in Section 2.3.1.

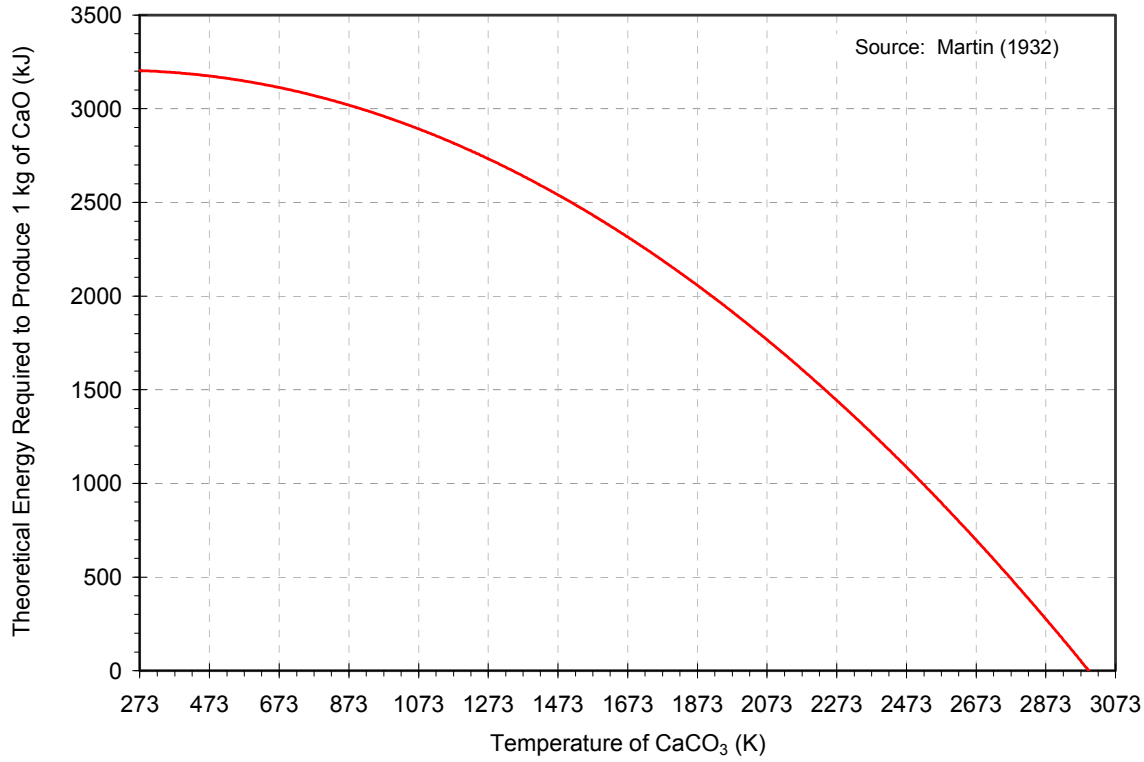

Figure 2-1: Energy required to produce 1 kg of lime as a function of initial temperature based on Equation [2.2].

The second requirement for the calcination reaction to proceed is the removal of carbon dioxide from the reaction zone. The partial pressure of CO_2 must be low enough to allow more CO_2 to be evolved. The relationship between CO_2 partial pressure and temperature is well known, with many researchers developing their own equations for this representation. One such example by Dennis and Hayhurst (1987) is:

$$Log_{10}K_P = \log_{10} P^e_{CO_2} = -\frac{8308}{T} + 7.079 \qquad [2.3]$$

A plot of the dependence of the reaction on the temperature and dissociation pressure as obtained by seven different authors, can be seen in Figure 2-2. There is a range of 50 Kelvin in the predicted values of reaction temperature at 1 atmosphere CO_2 partial pressure. The plot illustrates that for the reaction to proceed at any temperature, the partial pressure within the furnace must be lower than the corresponding partial pressure from the evolving CO_2. For example, using the Criado line (red), at 1140K the partial pressure of CO_2 must be lower than 60 kPa for the calcination reaction to proceed.

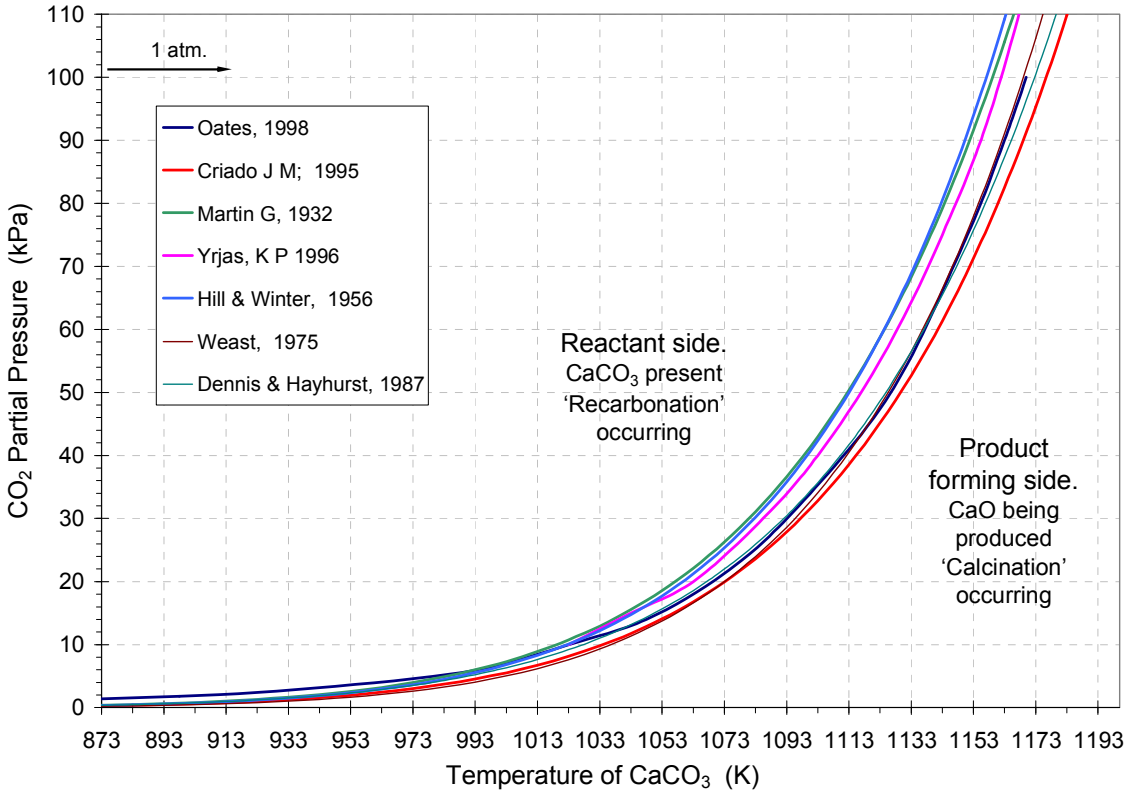

Figure 2-2: The range of dissociation pressure of CO_2 for calcite for different authors.

Due to the exponential form of Figure 2-2 only a small increase in temperature results in a large increase in allowable partial pressure for the reaction to proceed. For example, a 50°C increase from 900°C almost doubles the allowable CO_2 partial pressure from 100 kPa to 195 kPa. For high kiln temperatures, such as in solar furnaces, the partial pressure of CO_2 plays only a minor role in the rate of calcination.

2.3.1 Mechanisms of Calcination

The dissociation of limestone proceeds gradually inward from the outer surface of the stone. After initial surface calcination, the following processes are regarded by Oates (1998), to be the steps taken for the reaction to proceed into the limestone particle.

- Heat is transferred from the furnace environment to the surface of the decomposing particle.
- Heat is then conducted from the surface to the reaction interface, through the newly formed micro-porous layer of lime.
- If the temperature at the reaction interface is high enough, the heat causes the dissociation of $CaCO_3$ into CaO and CO_2.

- The CO_2 produced migrates away from the reaction interface, through the lime layer to the surface of the particle. During its diffusion through the lime layer, the CO_2 is heated to the same temperature as the surface.
- The CO_2 migrates away from the surface into the furnace environment.

The calcination of a sphere of limestone is represented graphically in Figure 2-3. Initial surface calcination can occur at a temperature of around than 873K as shown in Figure 2-2, so long as the partial pressure of carbon dioxide around the stone is virtually zero. This would occur within a kiln if there was free flow of air past the stone which removes the evolving CO_2.

Boynton, (1980) describes that for the reaction to penetrate to the interior of the stone particle, attainment of temperatures considerably higher than the dissociation temperature (1173K) is necessary on the surface of the particle. This is mainly due to the extremely low thermal conductively of lime, and therefore a large temperature potential between the surface and the reaction zone is required to drive the heat through at a reasonable rate. In general, the larger the diameter of the stone particle, the higher is the surface temperature required to calcine its centre.

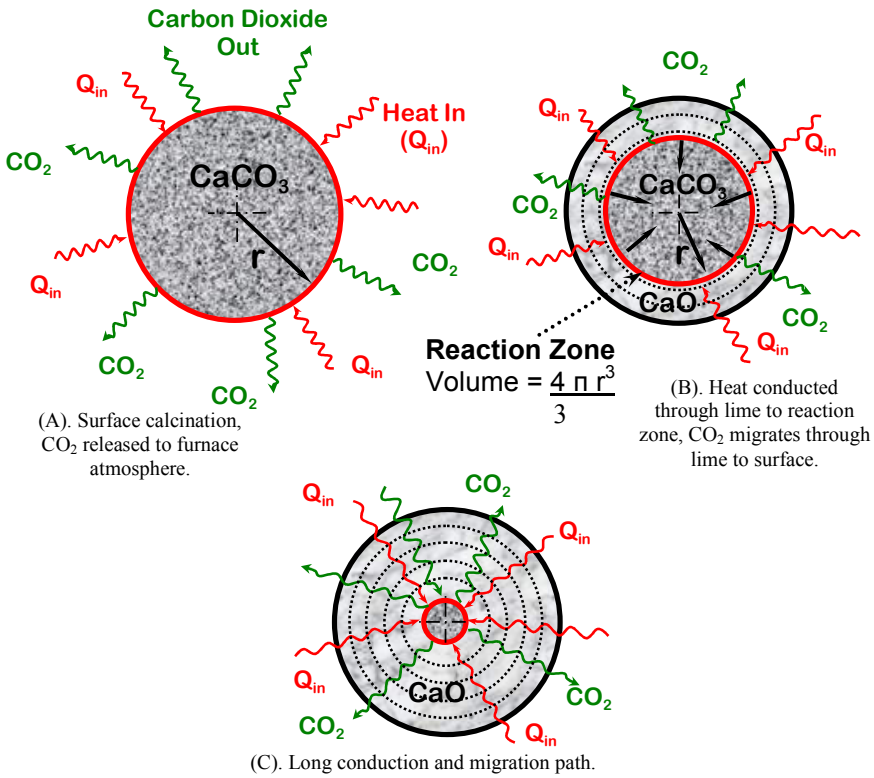

Figure 2-3: Decomposition of a sphere of calcium carbonate (Shell or layer model) under uniform heating.

2.3.2 Kinetics of Calcination

To ensure complete calcination, three essential factors in the kinetics of limestone decomposition are required:

1. The entire stone must be heated to the dissociation temperature of the carbonate.
2. This minimum temperature must be exceeded for the duration of the calcination process.
3. The carbon dioxide gas that is evolved must be removed.

If the temperature of dissociation is not reached throughout the stone then the lime will be under-burnt and limestone, or only partially calcined lime, will remain (called bullheads). Conversely, if the dissociation temperature is significantly exceeded, to temperatures higher than 1200°C, the lime will become over burned (hard burnt). Hard-burnt lime is significantly less reactivity than 'normal' lime thereby rendering it less workable and undesirable for most commercial products. Calcination at very high temperatures also causes significant sintering of the surface layer of the lime. This restricts the release of the evolved carbon dioxide from the centre of the stone and therefore hinders the completion of the calcination process. If sintering occurs to a fully calcined lime lump, it is said to be dead burned and becomes inert (Oates, 1998). The degree of hard burning can be reduced by cooling the quicklime immediately after complete calcination and or by calcining the limestone at a lower temperature, for a longer duration.

The objective of commercial lime manufacture as described by Mason *et al*. (1999) is to produce a completely calcined, soft-burned lime in which no more than 1–2% of the stone has an un-burned core. Such limes are the most porous and chemically reactive.

2.3.3 The Effect of Carbon Dioxide Partial Pressure

As described previously the partial pressure of the carbon dioxide is an important factor in influencing the reversible decomposition reaction of limestone. $CaCO_3$ begins to dissociate at a definite temperature, depending on the pressure of CO_2. If the partial pressure is increased, so too must the temperature be, for the calcination to proceed. If the temperature and pressure are in equilibrium, regardless of their values, dissociation is static (Boynton, 1966).

The dissociation of the limestone proceeds gradually from the outer surface of the stone particle inward. This theory is represented graphically in Figure 2-3. During calcination, the atmosphere immediately below the outer layer of limestone is thought to be 100% CO_2 no matter what the CO_2 percentage in the furnace (Mallen, 1956). It would therefore mean that calcination does not occur below the outer layer until a temperature of at least 900°C has been achieved. Khinast *et al*. (1996), provide a schematic representation of this concept which can be seen in Figure 2-4. It should be noted that the presence of N_2 in this representation indicates that the particle is located in an atmosphere of air or combustion products.

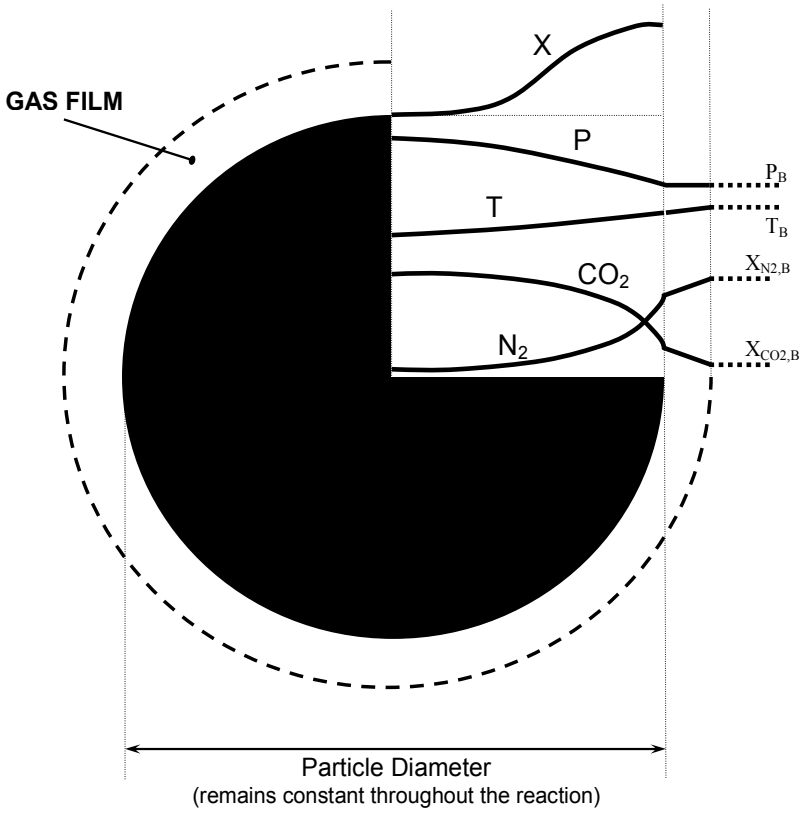

Figure 2-4: Representation of a spherical particle undergoing decomposition, showing pressure, gas density, temperature, molar fractions and conversion gradients.

Source: Khinast *et al*. (1996)

Here: X shows the decomposition gradient of $CaCO_3$ to CaO,

P shows the total resistance pressure,

T shows temperature,

CO_2 shows the carbon dioxide gas density,

N_2 shows the nitrogen gas density,

X_{N2} is the molar fraction of nitrogen,

X_{CO2} is the molar fraction of carbon dioxide,

Subscript B refers to the bulk phase.

The CO_2 formed during calcination has to overcome a certain resistance when diffusing through the quicklime layer. This results in a gradient of CO_2 partial pressure through the stone. The steeper the gradient in CO_2 through the stone the higher is the required temperature at the core for calcination to proceed.

As the reaction face moves inwards, the calcination reaction zone becomes smaller and the quantity of CO_2 being released is reduced. Therefore, the CO_2 pressure within the particle could reduce which results in a reduction in the required dissociation temperature. Mallen (1956) summarised this effect as "at a constant furnace temperature with increasing $CaCO_3$ – CaO interface depth, the dissociation temperatures decreases slightly".

The theory of pressure build up (or lack there of) as the CO_2 migrates, is a contentious issue. Boynton (1980) discusses the issue with larger sized stones by stating that the larger the diameter of the stone, the higher the temperature required for dissociation of the core due to increasing internal pressure as the CO_2 gas forces its escape. The CO_2 expelled has a longer distance to travel and often considerable internal pressure is exerted as the gas forces its escape.

Both theories have merits. Satterfield and Feakes (1959) discuss how the crystalline structure (pore size) of the lime effects the diffusion of CO_2 away from the reaction zone. Lime with small pore structures retard diffusion; where as large pores allow the flow of CO_2. It also depends on the shape of the stone. A spherical 150mm diameter stone size would produce approximately 2.1 kg of CO_2. Fifteen percent (0.3 kg) of the evolved CO_2 would have to diffuse through 37.5 mm or more of lime. An elongated stone with the same mass has less distance between the reaction zone and outer surface could allow the faster expulsion of CO_2. The effect of particle shape is not investigated here due to time constraints. It is recommended that future investigations should be conducted to determine if certain shaped limestone are beneficial to increase reaction rate.

2.3.4 Re-Carbonation

The limestone reaction is reversible, and so re-carbonation of lime readily occurs. Re-carbonation within the furnace most commonly occurs during the heat recovery or cooling stage of the process. It is important therefore, to cool the lime as rapidly as possible in an atmosphere containing as little CO_2 as possible.

Re-carbonation within the furnace is usually caused by sintering of the outer surface, but can also occur if the carbon dioxide partial pressure within the furnace is too high and / or the furnace temperature is too low. Sintering causes the stone to shrink and the lime pores to close, effectively restricting the release of evolved CO_2. Therefore if calcination has not completed and sintering occurs, the evolved CO_2 may become trapped within the particle. Gutschick (1995) discusses how the possibility of re-carbonation underscores the importance of rapid expulsion of the CO_2 gas during calcination.

The percentage of re-carbonation which varies depends upon the size of the particle, with a greater proportion of CO_2 absorption occurring in smaller particles. Boynton (1980) discusses how fine lime dust typically experiences 100% absorption, while 150mm lumps experience a maximum of 25 – 30% absorption. When re-carbonation occurs on the surface of a particle it forms a dense $CaCO_3$ layer effectively halting further CO_2 from entering the particle. Excessive re-carbonation is generally indicated by an abnormally low reactivity. Oates (1998) explains that re-carbonation can seriously diminish the quality and consistency of the lime product.

Re-carbonation over the long term is impossible to halt. The amount of CO_2 liberated during calcination is recaptured by lime plaster and lime mortars to reform limestone if no additives have been added to the mixtures. Therefore, the net environmental impact of CO_2 release into the atmosphere will approach zero over time.

Dobner *et al*. (1977) conducted experiments on the cyclic calcination and re-carbonation of calcined dolomite and found that the addition of steam to the furnace atmosphere resulted in nearly a two order of magnitude increase in the re-carbonation rate. Boynton (1980) and Oates (1998) both discuss how steam and moisture increase re-carbonation by causing surface hydration of the quicklime and then carbonation of some of the calcium hydroxide as it forms calcium carbonate and water, which is then free to hydrate more quicklime. The mechanisms of carbonation abatement using steam are not addressed within the present investigation, but it is noted that further investigation could be conducted within this field.

2.3.5 The Rate of Calcination

The rate of the reaction of limestone is paramount to determining how long the limestone needs to spend in the furnace. The faster the reaction occurs, the faster the manufacturing process can be. The mechanisms controlling the reaction rate are not investigated in this research, so only a brief review is given.

The calcination rate depends on the slowest of the three rate controlling processes:

1. Heat transfer to the stones surface.
2. Mass transfer of CO_2 away from the reaction zone.
3. The rate of the chemical reaction itself.

The rate controlling step has been analysed by many investigators, a small selection being: Satterfield and Feakes (1959), Ingraham and Marier (1963), Searcy and Beruto (1978), Borgwardt (1985), Dennis and Hayhurst (1987), Rao (1989, 1993, 1996), Murthy *et al*. (1994), Criado *et al*. (1995), Wei and Luo (1995), Khinast *et al*. (1996), Brown *et al*. (2000), and Ar and Dogu (2001). There appears to be very little consensus over the rate-controlling step, with the investigators spread fairly evenly over the three rate controlling processes. This suggests that, as deduced by Khinast *et al*. (1996) 'the reported importance of different limiting steps to the overall reaction may be largely due to different experimental conditions, experimental set-up and sample sizes'. Satterfield and Feakes (1959) believe that the rate controlling step is an interrelationship between the three major rate processes.

The relationship between calcination rate and temperature can be expressed using the Arrhenius equation:

$$\frac{dX_{ls}}{dt} = k.\exp\left(\frac{-Ea}{RT}\right) \qquad [2.4]$$

Here:

$\frac{dX_{ls}}{dt}$ is the rate of calcination

k is the Arrhenius rate constant (sec^{-1}) (characteristic of limestone)

E_a is the activation energy of the reaction (180 ± 20 kJ/mol)

R is the Universal Gas Constant = 8.314 J/ K. mol

T is the absolute temperature (K)

The Arrhenius rate constant (k) is found experimentally by plotting the rate of calcination against time. The slope of the plot is the Arrhenius rate constant and the activation energy is the y-axis intercept. Dennis and Hayhurst (1987) suggested that, as the observed rate of the reverse carbonisation reaction is not dependent on temperature, the activation energy for carbonisation must be equal to zero. This argument implies that the activation energy for the forward calcination reaction would be equal to the heat of reaction. This is not strictly correct because recarbonation occurs more readily between 400°C and 600°C as discussed in Boynton (1980). Therefore, there is a small difference between the activation energy and the heat of reaction.

The effect of the carbon dioxide partial pressure on the rate of calcination has been extensively investigated because it is a dominant rate limiting parameter. Early investigations showed that, in a vacuum, the rate of calcination penetration within a limestone particle is proportional to the equilibrium partial pressure of CO_2. Ingraham and Marier (1963) found that the reaction rate decreases with increasing partial pressure of carbon dioxide. This relationship was originally thought to be linear but subsequent investigations by Khinast *et al*. (1996) show that it is exponential. It was proposed that the rate was proportional to the equilibrium partial pressure of CO_2, $P^{e}_{CO_2}$, minus the partial pressure of CO_2 at the interface, $P^{i}_{CO_2}$, i.e.

$$\text{rate} \, \alpha \left(P^{e}_{CO_2} - P^{i}_{CO_2} \right)$$

However, Mallen (1956) found that the above relationship does not hold for the calcination of Penrice marble and Dennis and Hayhurst (1987) found the same for Penrith Limestone. Instead, it was found that the rate is proportional to a modified equilibrium CO_2 partial pressure minus the interface CO_2 partial pressure:

$$\text{rate} \, \alpha \left(P'_{CO_2} - P^{i}_{CO_2} \right)$$

Here: $P'_{CO_2} < P^{e}_{CO_2}$

Adding to this, Telfer *et al*. (2000) proposed that the reaction rate is proportional to the difference in the equilibrium partial pressure of CO_2 and the actual partial pressure of CO_2 at the reaction interface

$$\text{rate} \, \alpha \left(P^{e}_{CO_2} - P^{i}_{CO_2} - Py_1 \right)$$

Here: y_1 is the constant mole fraction of CO_2, which is dependent on the temperature.

Py_1 accounts for the heat and mass transport processes. This determines the three major rate processes as described by Satterfield and Feakes (1959).

Boynton (1966) suggests that there is an optimum calcination temperature and rate of heating for every different limestone that can only be determined by experimentation. Gutschick (1995) asserts that at constant temperature, the rate of calcination varies inversely with the size of the stone, increasing with smaller fractions. He suggests that the size

gradation of limestone is possibly the greatest influence on lime quality. Additionally, Oates (1998) describes how narrow stone gradations (2:1) are more favourable for uniform calcination, where the larger the gradation the greater the tendency for the small particle to become hard burned or the large particle to become under-burnt or a mixture of the two.

An increase in stone temperature by 20°C is reported by Mason *et al*. (1999) to have the same influence on calcination as extending retention time from 2 to 10 hours. Boynton (1966) reports that the rate of heating has the greatest influence on lime quality, the shrinkage, porosity, and reactivity. Although Boynton also advocates that raising the temperature completes calcination more effectively than lengthening its duration.

Mason *et al*. (1999) and Oates (1998) both recommend that from the viewpoint of the lime burner the major variables affecting the rate of dissociation are:

1. The characteristics of the limestone,
2. The particle size distribution,
3. The shape of the particles,
4. The temperature profile in the calcining zone, and
5. The rate of heat exchange between the furnace atmosphere and the limestone.

The difficulty in producing a unified theory of the kinetics of calcination is that it would need to account for all of the above processes, any one of which may become rate determining under particular circumstances.

2.3.6 Effects of Heating Rate

Concentrated solar radiation can potentially achieve heat fluxes of 10,000 kW/m^2 and temperatures of 3600°C as shown in Figure 1-6. The rate at which heat is transferred to the limestone affects the calcination rate and subsequently the reactivity of the quicklime. Telfer (1999) found that a sudden increase in stone temperature can cause the limestone to fracture or explode during the first few minutes which results in various sized limestone which complete calcination at different times. Hard burning of the smaller stone pieces can then occur.

Within a solar furnace the rate of heating will depend on the total heat transfer to the stone. This net energy balance is affected by the absorptivity and emissivity of the limestone. The colour and surface finish of each stone will therefore greatly influence the heating rate processes. Additionally the size, shape and material consistency are issues which need

consideration for process optimisation. A substantial literature review did not identify any publications on the effects of stone surface finish, size or shape on the calcination rate when using solar radiation as the heating source. Although published work does discuss how prolonged exposure to calcination temperatures above 1200°C are a major reason for the production of hard-burnt, low-quality lime (Mallen, 1956; and Moropoulou *et al*., 2001).

Within the proposed solar furnace (presented later in this thesis) the heating rate of the limestone can be controlled through either adjusting the intensity of the solar radiation entering the furnace or adjusting the exposure of the limestone to the radiation. That is, through the control of either the:

1. Total radiation flux being delivered to the furnace.
2. Distribution of the radiant heat flux within the furnace.
3. Quantity, type and size of limestone passing through the furnace.

Quantifying these parameters form the basis of the experimental aspects of this research investigation.

2.3.7 Effects of Limestone Particle Size

The consistency of quicklime product is affected by the variation of stone particle size and shape passing through the furnace. A large variability can lead to a mixture of soft and hard burnt quicklime which cannot be effectively utilised. Both Boynton (1980) and Oates (1998) note that a length to width size ratio of approximately 2 to 1 has been found by experience to achieve a sufficiently uniform calcination time for a high product consistency and quality. Although this is dependent on the manufacturing process being used.

The dissociation of limestone, as discussed in detail in Section 2.3.1, proceeds gradually from the outer surface of the stone inward. Experiments conducted by Mallen (1956) found that the reaction zone gradually moves towards the centre of the stone in a relatively spherical fashion regardless of the original shape of the stone. As the quicklime product layer increasing in thickness, the heat must conduct through an increasing distance. Adding to this, quicklime is inherently thermally insulating making conductive heat transfer relatively difficult. A thickening of the quicklime layer also makes it more difficult for the evolved CO_2 to diffuse through to the surface. An increase in the partial pressure of CO_2 can be experienced and consequently a higher disassociation temperature could therefore be required, as noted by Gallagher and Johnson (1973).

Within a solar furnace, it is desirable to maximise the exposure of the stone to the direct radiation. This means either crushing the rock into smaller particles or rotating the rock so that it has uniform exposure. Caution must be taken with either approach to minimise the unnecessary consumption of electrical energy which could offset the benefits of using solar energy (Nathan, 2002). Additionally, Ar and Dogu (2001) document that heat transfer resistances as well as resistance to the diffusion of evolved CO_2 between closely packed limestone particles has a significant effect on the calcination rate.

An assessment on the optimal bed depth for the limestone within the solar furnace therefore forms part of the research investigation reported in this thesis.

2.4 Modelling the Calcination Reaction

This section reviews the theory required to mathematically model the calcination reaction of limestone particles. It then identifies the type of mathematical model used for this investigation, considering the use of radiation as the sole heating source.

Modelling a gas-solid reaction might seem to be relatively simple, but there are several different possible mechanisms. Considerations for the calcination reaction model must include:

1. The shape of the limestone.
2. The modes of heat transfer to the limestone from the furnace environment.
3. The heat transfer within the limestone.
4. The speed of the reaction, and
5. The composition (physical characteristics, impurities and crystalline structure) of the limestone.

These considerations and approaches are similar to those used when modelling the heterogeneous gas-solid reactions associated with the devolatilization of single coal (char) particles, which according to Laurendeau (1978) are governed by an intricate coupling of transport phenomena and chemical kinetics.

2.4.1 Models Used For Non-Catalytic Gas-Solid Reactions

There are several different modelling possibilities for representing gas-solid reactions, depending on the initial surface area of the solid reactant and how the surface area changes with time. A representation of a standard gas-solid reaction can be shown as:

$$A_{(g)} + B_{(s)} \rightarrow E_{(g)} + F_{(s)}$$

The three most commonly used mathematical models for limestone calcination, as given by Smith (1981), are:

- the Shrinking Core reaction Model,
- the Uniform Conversion Model (Homogeneous Model), and
- the Grain Model.

Investigators such as Ingraham and Marier (1963), Hills (1968), Dennis and Hayhurst (1987), Khraisha and Dugwell (1989), Milne *et al*. (1990), Telfer (1999) and Ar and Dogu (2001) have mathematically described the calcination of limestone using the Shrinking Core Model (SCM), or a modified version of it. Satterfield and Feakes (1959) showed that there is no defined reaction front as is assumed within the shrinking core model, so Rao *et al*. (1989) and Murthy *et al*. (1994) developed a Grain Model (GM) to describe the decomposition reaction. The two models (SCM and GM) fit their own experimental data adequately, but performed more poorly when applied to other investigator's results. Khinast *et al*. (1996) developed a modified random pore model which represents his TGA experiments, where the reaction rate decreased exponentially with increasing CO_2 partial pressure. It was concluded that both chemical kinetics and mass transport in the particle were the reaction limiting factors. Borgwardt (1985) applied a kinetic model based on the measurement of the surface area of $CaCO_3$ using the Brunauer-Emmett-Teller method (B.E.T.). The model satisfactorily predicts the rate of calcination in a dispersed particle system of 1 to 90 μm limestone at temperatures 516°C to 1000°C and 80% conversion. This model unfortunately failed to provide an accurate representation for data collected by other investigators. Khinast *et al*. (1996) used a modified random pore model which assumes that the reaction limiting factors are chemical kinetics and mass transport through the particle. Silcox *et al*. (1989) produced a simplified SCM model that describes the decomposition of the parent material at the reactant product interface, the diffusion of CO_2 or H_2O through the growing CaO layer, and the sintering of the CaO layer. The model is qualitative, but it provides useful estimates of peak CO_2 pressures in the CaO layer, relative rates of surface area development and loss for $Ca(OH)_2$ and $CaCO_3$, the effect of particle size, and the effects of time and temperature.

The three different models will now be discussed in more detail.

2.4.2 The Shrinking Core Model

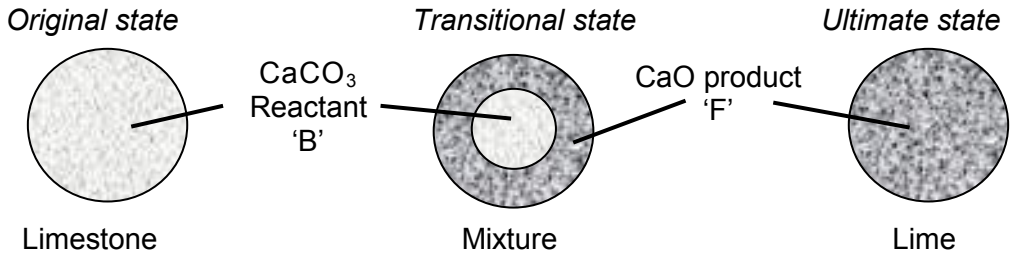

The Shrinking Core Model was developed for solids that are non-porous, although the model can be used where the rate of the chemical reaction is much slower than the diffusion of the gas through the newly formed product (Smith, 1981). The main feature is that the reaction occurs at an interface between a spherical un-reacted core ($CaCO_3$) and a surrounding solid product (CaO). As the reaction progresses and the un-reacted core shrinks, the zone of reaction moves towards the centre of the solid. Telfer (1999) presents equation [2.5] which relates the calcination of a spherical solid to the radius of the un-reacted core. It should be noted that the bulk density is used in equation [2.5] which does not account for density differences between the $CaCO_3$ and CaO.

$$X = \frac{m_o - m_t}{m_o} = \frac{\frac{4}{3}\pi\rho_m r_o^3 - \frac{4}{3}\pi\rho_m r_c^3}{\frac{4}{3}\pi\rho_m r_o^3} \qquad [2.5]$$

Here:

X is the fractional calcination of limestone,

m_o is the initial mass of limestone,

m_t is the mass of calcining limestone at any time(t),

r_o is the initial radius of the solid limestone,

r_c is the radius of the un-reacted limestone core at any time, and

ρ_m denotes the bulk density of the reacting particle.

Cancelling similar values gives:

$$X = 1 - \left(\frac{r_c}{r_o}\right)^3$$

There is three rate-limiting processes for this model :

- External gas diffusion,
- Chemical reaction, and
- Product layer diffusion that can occur in any gas-solid reaction.

This model does not account for heat transfer to the particle which is a significant rate controlling steps. Although the rate controlling steps do depend on the type of experimental equipment used.

The calcination reaction is a first order chemical reaction; therefore, the time required for calcination for a chemical reaction controlled region can be described by:

$$t = \frac{\rho_B r_o}{M_B b k_s (C_A)_b}\left[1-(1-X)^{1/3}\right] = \tau\, f_c(X) \qquad [2.6]$$

Here:

$$\tau = \frac{\rho_B r_o}{M_B b k_s (C_A)_b}$$

And $$f_c(X) = \left[1-(1-X)^{1/3}\right]$$

b is a stoichiometric coefficient,

M_B is the molecular weight of the solid reactant,

$(C_A)_b$ is reactant gas concentration, and

k_s is the reaction rate constant.

The time required for calcination for the product layer diffusion controlled region is:

$$t = \frac{\rho_B r_o^2}{6 M_B b D_e (C_A)_b}\left[1-3(1-X)^{2/3}+2(1-X)\right] = \tau\, f_d(X) \qquad [2.7]$$

Here:

$$\tau = \frac{\rho_B r_o^2}{6 M_B b D_e (C_A)_b}$$

$$f_d(X) = \left[1-3(1-X)^{2/3}+2(1-X)\right]$$

where D_e is the effective diffusivity through the product layer.

It should be noted that the above equations represent the shrinking core model applied for extreme rate controlling situations. Other assumptions used to develop the simple mathematical expression for the various controlling stages of the shrinking core model include:

- The reactant solid is spherical and the spherical shape is maintained throughout the course of the reaction.
- No other physical or chemical changes take place during the calcination reaction.

- There is negligible gaseous build up between the unreacted core and product layer.
- The porosity of the reactant ($CaCO_3$) and product (CaO) are considered equal.

However as reported by Oates (1998), the apparent density varies from 2.7 g cm^{-3} for high calcium limestone to below 1.4 g cm^{-3} for the resultant CaO. This gives rise to approximately 55% porosity in the CaO product for a constant volume. The equal porosity assumption does not therefore take into account the structural changes which occur within the calcining particle.

A pseudo-steady state approximation has been developed by Smith (1981) which assumes that that the density of the gas in the pores of the solid is much lower than that of the solid reactant. From this it can be deduced that the rate of movement of the reaction interface, $\frac{dr_c}{dt}$, is small compared with the velocity of the diffusion of gas through the product layer.

Telfer (1999) suggests that the SCM model gives a good representation of the calcination trend, but could not provide a statistically sound fit. It was suggested that the calcination process is too complex to be summarised by SCM applied to the grain level of the $CaCO_3$ particle. Despite these limitations, the shrinking core model forms the basis for mathematically modelling the calcination of Penrice marble within this thesis.

2.4.3 The Uniform Conversion Model (Homogeneous Model)

The uniform conversion model can be employed to model highly porous particles that contain enough voidage for the gaseous reactant to enter and reach all areas of the solid with negligible diffusion resistances. The rate of reaction changes as the product layer accumulates and varies the surface area of solid reactant. It is assumed that during the reaction, the density of the particle decreases while the particle size remains constant.

The conversion of solid product over time is a function of the first order rate constant, and is given by the following:

$$\frac{dX}{dt} = k.(1 - X) \qquad [2.8]$$

Which can be rewritten as:

$$-\ln(1 - X) = k.t \qquad [2.9]$$

Here X_l is the fraction calcination of the limestone
k is the first order rate constant.
t is time.

At different locations in the solid, different rates of reaction will arise. However, the reaction process is considered homogenous because at all areas, the solid is reacting continuously and progressively throughout the particle.

This model has limited use in the calcination of limestone due to the assumption that the gas can diffuse through the particle unabated. Most investigators report a significant influence of CO_2 partial pressure on the reaction rate Khinast *et al*. (1996). This model also does not consider the possibility of under-burning (bullheads) or hard-burning on the surface.

2.4.4 The Grain Pellet Model

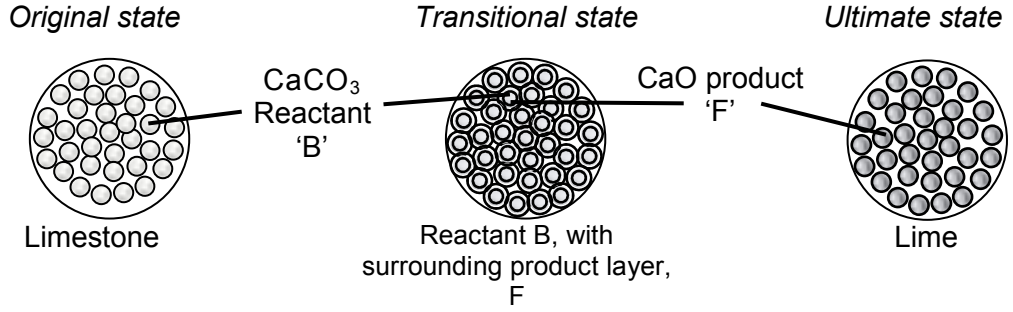

The grain theory depicts the solid reactant particle as a porous pellet comprising of numerous non-porous reactant grains. Each non-porous grain reacts according to the shrinking core model as described above. It is assumed that the $CaCO_3$ un-reacted core within each grain is chemically and physically static. Furthermore, the resistance to the intergrain gas diffusion between the pores is considered insignificant. Thus, for the chemical reaction and product layer diffusion-controlling region, the calcination time can be given by Equation [2.10] and Equation [2.11], which are similar to that for the SCM:

$$t = \frac{\rho_B r_g}{M_B b k_s (C_A)_b}\left[1-(1-X)^{1/3}\right] = \tau\, f_c(X) \qquad [2.10]$$

$$t = \frac{\rho_B\, r_g^2}{6 M_B b D_e (C_A)_b}\left[1-3(1-X)^{2/3}+2(1-X)\right] = \tau\, f_d(X) \qquad [2.11]$$

Here:

r_g is the radius of particle grains $= \dfrac{3}{S_g\, \rho_B}$

S_g is the initial surface area, and

ρ_B is the density of the spherical grain.

The grain pellet model is based on the shrinking core model. It has yet to find extensive usage due to the complexity of representing a larger particle from a collection of pellet calculations. Rao *et al*. (1989) and Murthy *et al*. (1994) have done so, and have achieved results that represent their experimental data satisfactorily. To date no other applications or comparisons with experimental data were found.

2.4.5 Calcination Modelling of Non Uniformly Heated Limestone

There has been limited investigation on mathematically modelling the calcination of limestone when exposed to a non uniform heating source. One published article was found, Lipinski and Steinfeld (2004) that uses a discretised domain to calculate the heat fluxes through each modelling cell to provide a time dependent three dimensional energy transfer model. The model calculates the conduction, convection and radiation transfers between an Argon arc solar simulator and a prism-mound of $CaCO_3$ particles placed on a silicon carbide refractory plate. A time dependent energy balance around the experimental set-up is evaluated. The $CaCO_3$ prism-mound is considered to be a homogenous porous solid and thus it can be deduced that the uniform conversion model is used. Calcination is considered complete after 270 kJ/mol is transferred to the 1200 K carbonate prism. The model does not consider intra particle heat or mass transfer within the sample. Calibration was achieved using experiments, where the mass loss of the limestone was measured at controlled intervals.

Unpublished work by Hancock (2002) used the shrinking core model equation developed by Hills (1968) for modelling the calcination of limestone under one dimensional heating by solar

radiation. A time dependent heat transfer approach is used, with the rate controlling step being conductivity to the reaction zone. End effects of the rectangular shaped particle, and mass transfer are neglected. The particle is divided into 2mm layers, which are assumed to be either 0% or 100% calcined.

The mathematical calcination model developed within the present research (and presented in Chapter 10) uses an energy balance approach, similar to the above examples, to calculate the heat absorbed by the marble sample from the radiation source. The energy balance model then calculates the heat transferred between the participating mediums surrounding the marble sample to obtain the resultant energy available to heat and then calcine the sample. The model then differs from the two examples above because they do not represent the environment where a single round stone is non-uniformly heated by solar radiation. Having non uniform heating over the surface of the stone will affect the transfer of heat to the reaction zone. Therefore, two calcination models are presented; the standard shrinking core model using a concentric core and a shrinking core model where the core is offset to the lower side of the sample. A representation of the two models is shown graphically in Figure 2-5.

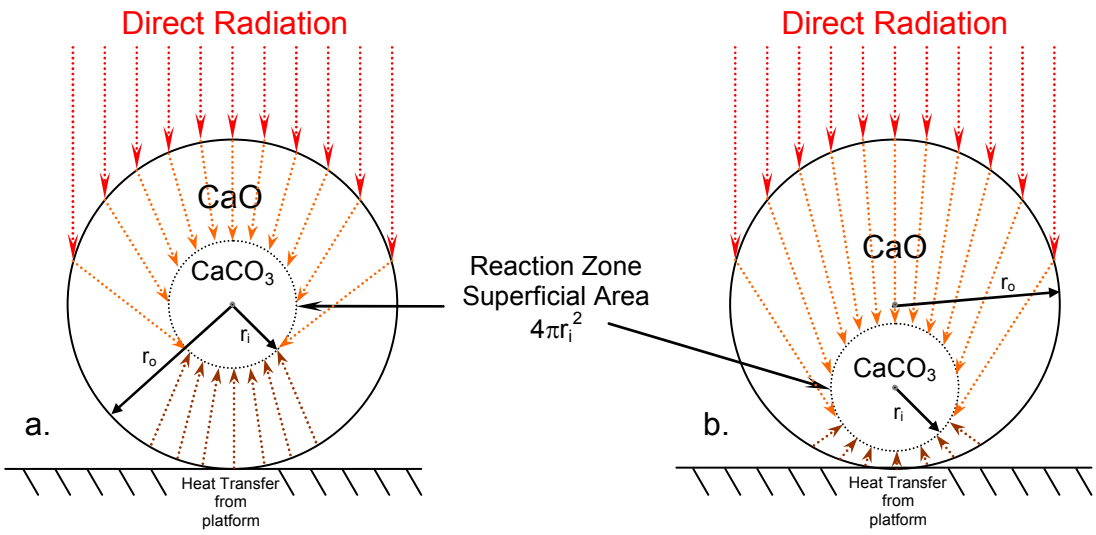

Figure 2-5: Representation of the (a.) standard concentric shrinking core model and (b.) eccentric shrinking core model for a limestone sample irradiated from one side.

2.5 Controlling Parameters for Lime Kiln Design

The selection of a lime kiln for a particular installation is a relatively complex process. The kiln must be suitable for burning a variety of feedstone and produce the required quality of quicklime at a competitive price. Its capacity must also be appropriate for the market requirements. Oates (1998) provides an initial check list for determining which kiln type might best suit the particular application. The considerations include:

- The characteristics of the limestone (particle size, purity and strength).
- Quality of quicklime required (CaO %, sulphur content and reactivity).
- Availability and cost of fuel(s).
- Any physical location constraints (available land and geographical location).
- Capital and operational costs.
- Current and forecasted market demand.

It is desirable to design a single kiln that can process almost all sizes and types of limestone, but many lime producers utilise more than one kiln for processing the larger and smaller limestone grades.

In the United States almost 90% of the lime producers use rotary kilns, while in Europe shaft kilns predominate. According to Schwarzkopf (1974) both kiln types have high production rates, are equal in product quality, and can process various sized limestone with good thermal efficiency. In addition, advanced energy recovery and preheating systems are making significant energy savings and are further reducing fuel costs for both systems.

Rotary kilns have higher energy consumption per mass of product than shaft kilns because of the greater heat losses from the larger external surface area of the rotary kiln and their thinner refractory linings due to rotational mass considerations. Mullinger (2007) discussed that high efficiency, modern rotary kilns consume around 1195 kcal per kg of product produced where as shaft kilns can quite easily be less than 850 kcal per kg. However a consistent stone size ratio is required to maintain good bed porosity within shaft kilns to allow uniform heat dispersion, as was discussed in Section 2.3.7.

For greater control over the burning process and subsequent higher purity and a more reactive quicklime product, a fluidised bed calciner or a rotary hearth system (Calcimatic) could be utilised. Fluidised bed systems require highly crushed fine limestone feed and have high capital costs as documented by Wingate (1985). Calcimatic kilns were a Canadian designed flat bed furnace which was over-fired using fuel oil or natural gas. These systems typically used pebble sized limestone but could utilise virtually any sized limestone as long as

a good size ratio (up to 1:3) is maintained. According to Oates (2001), unfortunately high capital and maintenance costs have seen all of the Calcimatic kiln phased out by the end of the 1980s.

2.5.1 Kiln Size and Production Rate

The size of a particular kiln is usually based on the required production rate. It would seem intuitive that a high production rate would require a single large kiln, but this is not always the case. Two smaller kilns that run in parallel can sometimes be utilised more effectively than a single large one. Utilising two different kilns can provide processing of two different sized stone at the same time Oates (1998). Another advantage is that one kiln can be temporarily shut down of maintenance (or if production is seasonal) without shutting down the entire plant. Although it is considered by Boynton (1966) that construction and maintenance costs are higher if two different types of kilns are used as opposed to using two of the same type of kiln.

The practical operating ranges and typical limestone sizes are given in Table 2-1. The variation in production output depends on the size of the kiln. Larger kilns typically have higher outputs because they can expose more of the limestone feed to the heat. The dominant modes of heat transfer are radiant and convective, which increases the rate of calcination, as discussed in Section 2.3.6.

Table 2-1: Operating output and range of stone sizes for various commercial lime kilns.

Kiln Type	**Output; Tonnes per Day**	**Range of Stone Size mm**
Long Rotary	100 – 1,500	0 - 60
Preheating, Short Rotary	100 – 1,500	0 - 60
Vertical Shaft	50 – 600	20 - 200
Flash Calciner	500 – 3,000	< 1
Fluidised Bed	30 - 150	< 2
Rotary Hearth	80 – 300	15 - 45

Sources: Oates (1998) table 16.1 and Sauers *et al*. (1993) table 2

There is no intuitive relationship between plant output rate and the limestone size. The difference in the range of stone size for each kiln type is influenced by the physical processes in the kiln. The method of heat transfer and transport / movement of the stone

through the kiln will dictate the maximum and minimum stone size. For example a flash calciner maintains the limestone particles in suspension using an air stream. Particles too large to be entrained within the air stream cannot be processed.

Other factors that affect the stone size range and therefore type of kiln include the characteristics of the local limestone, the pre-processing costs of crushing and screening the stone, the desired production rate, the quality of the quicklime and its final application.

2.5.2 Stone Size Reduction

Quarrying of raw materials consists of drilling, blasting, loading, overburden removal and hauling. The hauled material is commonly processed within a short distance of the quarry to minimise haulage costs and unnecessary transport of reject or overburden material. The processing of limestone involves crushing / grinding, sizing, beneficiation (reduction of impurities), storage / load-out and transportation. After transportation costs, Oates (1998) notes that crushing is one of the more energy-intensive limestone processing operations.

After blasting, Boynton (1980) reports that primary crushing is the most effective method of stone size reduction. Stone is generally crushed in two ways: by impact or compression. Compression crusher types include the jaw crusher, gyratory crusher, and roll crushers, which all apply a slow load (or pressure) onto the rock until it breaks apart. Impact crusher types include the aptly named impact crusher and also the hammermill. These crushers apply a sudden impulsive force which smashes the rock apart. According to Oates (1998) impact crushers are generally lower in capital cost, but require relatively more electrical energy for the same size reduction and also produce more fines (small particles).

Oates (1998) reports the hardness of limestone ($CaCO_3$) to be in the range of 2 to 4 on the Mohs scale and the compressive strength of limestone to vary between 10MN/m^2 for chalks, to 200MN/m^2 for marbles. Because the strength of a material is a function of the cross sectional area of the particle, it can therefore be expected that smaller particles require less force per stone to break apart than larger particles. This does not necessarily translate to a reduction in energy consumption, which is associated with crushing rate and the loading of the crusher.

The parameter of great interest in crushing is the grindability of a material, which is defined as the amount of product produced per unit of expended energy. The power to size reduction ratio is a difficult parameter to quote because it is dependent on the material being processed.

Table 2-2 shows selected data from Sillem (1977, Table 1) which reports the reduction ratio of Japanese limestone using four different crushers and the power consumption per tonne. Table 2-2 illustrates that the hammer mill has a 30 – 100% higher average specific power consumption than the other crushers, but has the highest reduction ratio and could therefore reduce rocks 1.5m in the feed size to 25mm in a single pass. Energy consumption per unit reduction has been calculated and added to the data from Sillem's table to illustrate that the hammermill and the gyratory crusher are approximately equivalent in energy usage for each reduction in stone size.

Table 2-2: Characteristic data of four types of limestone crusher.

NOTE:
This table is included on page 46 of the print copy of the thesis held in the University of Adelaide Library.

Source: Sillem (1977), Table 1

The present investigation assesses Penrice marble so that a brief examination of the power used to reduce the size of this stone is conducted. Special thanks go to the mine manager, Andrew Graetz for provided the power and flow rate data.

The Penrice crushing and processing plant currently uses two serial crushers for stone size reduction; an *Allis Chambers* (54" x 74") gyratory primary crusher and a *Terax Jaques* (4') secondary gyratory crusher.

The *Allis Chambers* primary crusher receives an average of 600 tonnes/hr of marble, which can be up to 1.8m in size. The crushing gap is set to 450mm which provides a 4:1 stone size reduction ratio. During the crushing process, the *Allis Chambers* gyratory crusher draws approximately 50 amps at 4 kiloVolts and thus the 350kW drive consumes approximately 275kW of power. The power consumption for the *Allis Chambers* primary crusher is therefore 0.115 kWh / tonne of unit size reduction. The *Terax Jaques* secondary crusher receives an average of 350 tonnes/hr of up to 450mm marble and its setting is 150mm which provides a 3:1 size reduction ratio. The *Terax Jaques* draws approximately 65 Amps (±5A)

at 1000 Volts and thus the 112kW drive consumes approximately 90kW of power. The power consumption is therefore 0.086 kWh / tonne for each unit size reduction.

This data indicates that the largest power consumption per tonne is when breaking the larger stone sizes in the primary crushing process, with a reduction in power consumption as the stone size reduces.

The crushed limestone is sorted into the various size ranges displayed in Table 4.3 using vibratory screens. It should also be noted that each crusher produces approximately 25% scalps or fines (sub 25mm marble particles) each. The scalps contain approximately 25% of stone between 25mm and 10mm, 38% between 10mm and 1mm, and 37% between 1mm and 75μm. These sized stones are currently used by local industry for glass and steel manufacture, road base, and in agricultural applications. Graetz (2000) explained that the scalps were currently screened into more distinctive size ranges before supply to the general market. Screening and sorting is a value adding process to a currently unusable mixture of product. An industry which can utilise the scalps before sorting can make a substantial reduction in processing cost and also a reduction in the wholesale costs of the marble.

One of the design targets for the proposed solar lime furnace is to reduce the total environmental footprint by reducing the electrical power consumption at the conceptual design process stage. By processing the material on a bed the crushing requirement and hence associated energy consumption is minimised. It is recommended that the designers evaluate the correlation between the electrical energy used for crushing the stone and the solar energy required to heat and calcine that sized stone. This evaluation can then be used for optimising the process residence time considering the available solar radiant energy, while reducing electrical power consumption by minimising the required crushing.

2.5.3 Optimising Furnace Shape for Radiant Heat Transfer

The energy efficiency of kiln operation is determined by the consumption of energy by the process, as presented by Jenkins (1990). It is desirable therefore to optimise a particular furnace design for the direct usage of the primary energy, by investigating effects of changing kiln structural dimensions and shapes. Meier and Cella (2004) note that the solar furnace should be designed so that a majority of the solar flux entering the aperture is used for the calcination process.

Within any solar furnace design process, consideration needs to be given to maintaining optical access into the furnace and then controlling and maximising the energy flow to the reactant(s). The design of the aperture should minimise the amount of energy being lost from the furnace. According to Steinfeld and Schubnell (1993), the furnace design must provide a good match of the solar flux density in the aperture to the rate of the calcination reaction and the feed rate of the limestone, so that the reactants reach a desired temperature over a given period of time. In addition, the design of the solar concentrating system should minimise the number of reflective surfaces to maximise optical efficiency. The use of an elevated furnace to collect radiation a heliostat field would allow only a single reflector but would also require the stone to be elevated for processing, which requires work. An assessment of the optimal configuration is site specific and would also be a critical part of the design process. Meeting these design requirements enables the lime producer to produce a desirable product as efficiently as possible. It is also intuitive that the more efficient the reactor performance, the smaller the required heliostat field for a given production rate and possibly the lower the capital cost of the lime manufacturing plant.

The shapes of solar furnaces vary between different applications. Villermaux (1979) reviewed numerous solar chemical reactors, giving the advantages and disadvantages of the different designs. Due to heat losses from the solar opening (and other areas of the reactor) Villermaux recommends that the solar reactor be as small as practical. For industrial scale solar lime production, large production rates are required, making small reactors impractical. Larger styles of solar furnaces are therefore required for lime calcination. Different styles are proposed and discussed in detail in the following section, with advantages and disadvantages being used to identify a viable options.

2.5.4 Basic Process Considerations

There are physical limitations to making lime kilns with different cross sectional shapes. The rotation of kilns that are not round in cross section is difficult to achieve. There are substantial structural issues due to the inconsistent movement of the process material, as well as unpredictable bed mixing and material flow problems. An alternative bed mixing method for non-round kilns is therefore required. Mixing ensures uniform heat distribution throughout the bed and also maintains stone rotation, avoiding hard burning of the stone on one side.

Non round kilns generally do not rotate. Rather, the limestone travels through the kiln on a flat grate which moves longitudinally through the furnace. Grate systems have been developed which offer considerable control over the movement of the feed stone through the

furnace. The exact type of grate system and or mixing method that could be used for solar thermal lime manufacturing is beyond the scope of this thesis. Additionally, issues that require further consideration include: duration of mixing, uniformity of mixing, and timing of the mixing. It is also recommended that a relatively dust free atmosphere be maintained to ensure a transparent furnace atmosphere.

2.6 Solar Thermal Lime Manufacture

The use of solar thermal radiant energy within kilns is not a new idea. Johann Friedrich Böttger, 1682-1719, German chemist and originator of Dresden china used a lens to concentrate solar radiation into his furnace for the thermal firing of porcelain statues and wares. However solar thermal concentrating systems have only been used infrequently to burn glass and other stoneware due to the long times required for successful firing and the temporal interruptions of the solar input by clouds or nightfall. It wasn't until the 1970's when large tracking heliostat fields became technically feasible that high temperature solar thermal applications were more fully investigated.

The thermo-chemical storage of solar energy and then its release at times of low solar radiation (night time and cloudy periods) has been investigated by numerous researchers such as Wentworth and Chen (1976), Villermaux (1979), Flamant *et al*. (1979), Diver (1987) and Imhof (1991) to name a few. The investigations identified numerous thermo-chemical processes, with limestone (specifically $CaCO_3$) being one of the numerous minerals being selected for more detailed consideration. They proposed thermo-chemical storage concepts to calcine limestone during the day and then hydrate it at night, and recover the energy released as a thermal power source. It is reported that this process could be suitable for long term energy storage and transportation of solar energy, e.g. to a location which has low solar insolation. It is my view that this method of solar energy storage and transport is not plausible due to the conversion efficiency losses and the undesirable production of CO_2. For an ideal conversion, calcining limestone consumes 3180 kJ/kg CaO of heat energy, and the heat energy released during Hydration (slaking) is 1156 kJ/kg CaO, a 36% loss of energy (Oates, 1998). Taking into consideration the efficiency of a solar lime manufacture process, which to date is reported by Flamant *et al*. (1979) to be up to 40% and a slaking heat collection efficiency between 50% - 75% (Boynton, 1980) the efficiency from solar to heat energy would be less than 11%. There is then the efficiency losses associated with using the heat produced by slaking to generate other useable energy forms, such as electricity. Hence such proposals are unlikely to be viable.

Flamant *et al*. (1979) proves that solar energy could be used to calcine limestone and therefore provide thermo-chemical energy storage. Thus, it is technically feasible and a viable proposition to calcine limestone using solar energy.

2.6.1 Solar Chemical Reactors Used For Lime Manufacture

A comprehensive review of solar chemical reactors was conducted by Villermaux (1979), Flamant *et al*. (1979) and Diver (1987) who identify advantages, disadvantages, limitations, and risks associated with solar chemical reactor designs. To date, only experimental laboratory sized solar furnaces / reactors have been built for the thermochemical decomposition of limestone.

Solar chemical reactors can be characterised into two basic types:

1. **Indirect receiver/reactors:** they use an intermediate heat transfer fluid, such as molten salts, or solid separator wall between the receiver and the reactor. The fluid or wall is directly heated by solar energy and then transfers the energy into the receiver.
2. **Direct absorption receiver/reactors:** they absorb sunlight directly on the reactor feed.

Current solar lime manufacturing reactors / furnaces generally use direct absorption methods. Two such solar furnaces are shown in Figures 2-6 and 2-7.

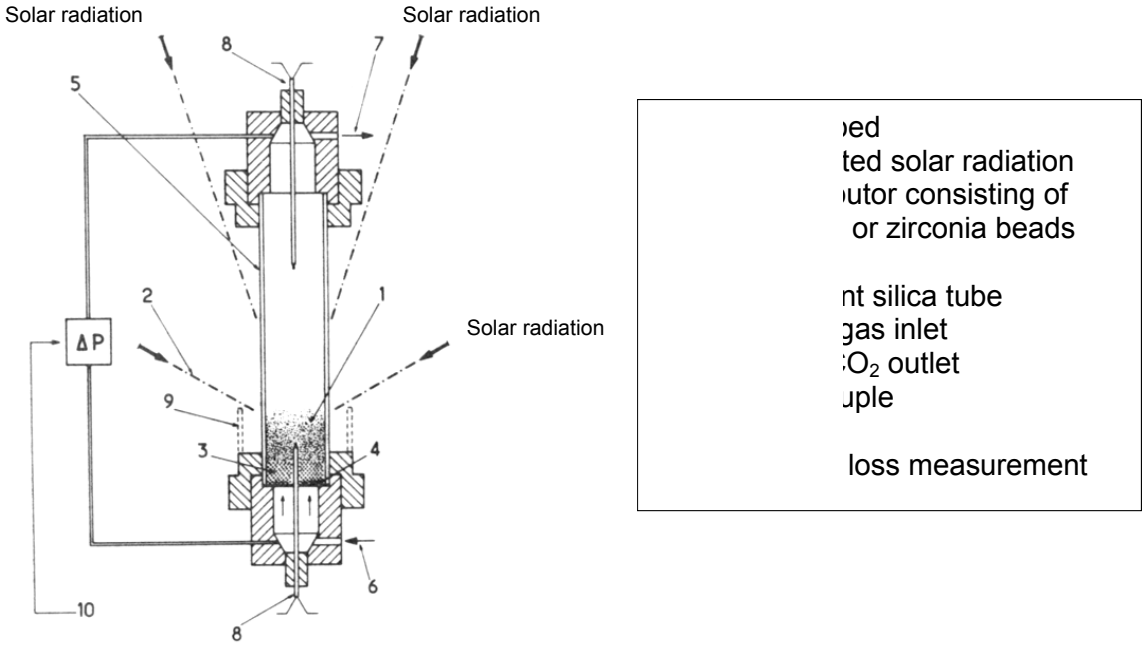

Figure 2-6: Schematic diagram of a solar fluidised bed reactor.

Source: Flamant *et al*. (1979)

1 – Refractory tube
2 – Limestone inlet
3 – Lime product outlet
4 – Insulator
5 – Axis of the tube (tilted)
6 – Concentrated solar rays
7 – Water cooled metallic shell

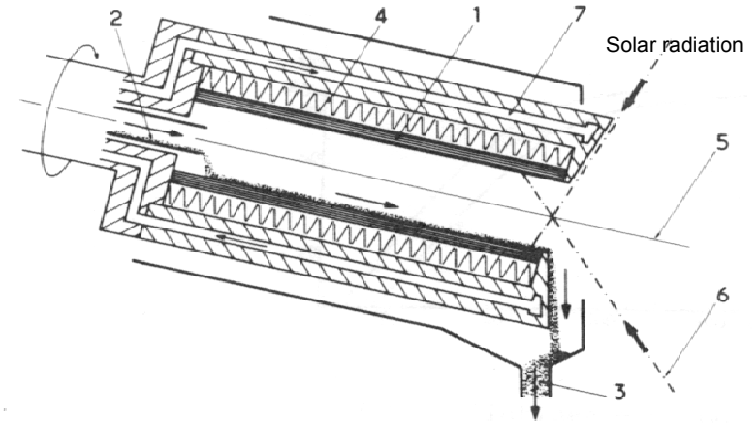

Figure 2-7: Schematic diagram of an open ended inclined solar rotary furnace.

Source: Flamant *et al*. (1979)

The fluidised bed reactor proposed by Flamant *et al*. (1979) is reported to provide a uniform temperature distribution throughout the bed of 0.6mm to 2.0mm diameter limestone, and a thermal conversion efficiency of up to 40%. The energy consumption is reported to be 32,400kJ/kg of CaO produced at an average 1.4 ± 0.1 kW of supplied radiant power. The radiant heat flux value was not provided. Measured data from the fluidised bed showed that a uniform temperature distribution is achieved within the bed and that good energy absorption qualities were obtained. The authors identified that the fluidised bed system consumes electrical energy to drive the fans producing the high velocity fluidising air for the bed, although no specific energy consumption rate was provided. Additionally, the fluidising air consumes a small proportion of the supplied solar energy thus reducing system efficiency (available solar to chemical conversion). It was estimated that 14.3% of the solar energy was lost through convective and conductive heat losses. The radiative losses through the transparent silica windows were approximately 32% and are described as “major” with recommendations being made to increase the absorptivity of the process material. Abrasion of the windows and walls by the limestone is not discussed. A reduction in the transparency of the silica windows (or any window) due to abrasion or dust increases its reflectivity and therefore reduces the energy absorption.

The rotary kilns proposed by Flamant *et al*. (1979) and further optimisation by Badie *et al*. (1980) is reported to have a significant thermal gradient (10,000°C.m^{-1}) axially along the length of the furnace. This is because, unlike a flame, where the heat is released along most of the length of the kiln, for this solar furnace, it is all introduced at one end. The energy consumption is reported to be 63 kW.h.kg^{-1} (226.8 MJ/kg) of CaO produced at an average 1.5 kW of supplied radiant power. The limestone particle size ranged between 0.2 to 0.315mm. The radiant heat flux was not provided. A completed calcination reaction conversion of only 30% was obtained, at a thermal efficiency of 7%, with a filling fraction of

0.15 and rotation speed of 8 rpm. These values indicate that it is unlikely that the solar decomposition of limestone using this rotary furnace process will be commercially viable.

Flamant *et al*. (1979) reported a need for better thermal insulation around the walls to reduce heat loss from the furnace, which varied between 70% and 95%. These conduction losses decrease as the loading increases. Heat loss from the opening through which the radiant energy inlet is directed was also not reported. Additionally the authors did not comment whether dust formation produced by the feed material movement through the furnace caused any adverse effects. Meier *et al*. (2002) observed significant heat and mass loss through the opening of their rotary kiln, which can be calculated to be approximately 56%.

Optimisation of the two solar furnaces was conducted by Badie *et al*. (1980) with the objective of developing a method to distribute heat inside the rotary furnace more evenly. One idea was to add graphite to the feed mixture. It is reported that this concept achieved a 36% increase (from 11% to 15%) in overall efficiency, which was calculated by comparing calcination time, the incident energy received, and the conversion rate. However carbon is considered an undesirable contaminant within quicklime, especially if slaking. No method to separate the graphite from the quicklime was proposed.

Another potential kiln enhancement was to position a stainless steel tube axially along the centre line of the furnace. The solar radiation was directed down into the tube, and thus the hot tube provides an indirect heating source. Tubes of various diameters (5.25mm - 36mm) and lengths (60mm – 120mm) were placed in the focal plain of a horizontal axis solar furnace. The tubes were closed at the far end to prevent leakage of direct solar radiation into the furnace. The conclusion was that “the addition of a metallic transfer wall seemed to improve the overall process efficiency” but no numbers were provided. Work-in-progress by Badie *et al*. (1980) included the construction of a continuous operation rotary kiln with a metallic transfer wall, and the development of an annular cylindrical fluidised bed which is shown in Figure 2-8.

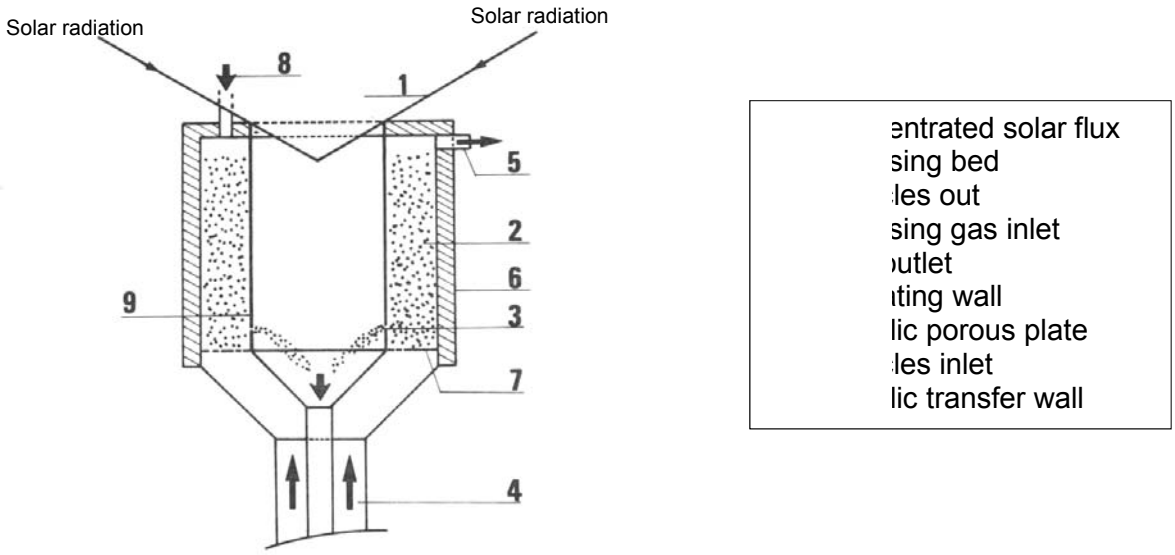

Figure 2-8: Diagram of the revised solar fluidised bed reactor, showing the heat transfer wall.

Source: Badie *et al*. (1980)

The experimental apparatus used for limestone calcination experiments used by Salman and Khraishi, (1988), which can be seen in Figure 2-9, consisted of a stainless steel box into which the solar radiation was directed. A quartz window located on the side of the box facing the solar concentrator allowed the radiation to be transmitted into the box's interior, onto the process material. A graphite tube positioned in the centre of the reactor is used for the introduction of the calcium carbonate or gypsum pellets (0.8g, 13mm diameter and 2-3mm long). The effect of time and temperature on the decarbonation rate of $CaCO_3$ and $CaSO_4.2H_2O$ was the primary purpose for this investigation. The limestone pellet was only illuminated from one side causing the calcination rate (heat transfer rate and CO_2 diffusion) to decrease as the reaction zone moved away from the illuminated side of the pellet. It was shown that for a temperature increase from 1165°C to 1446°C, the calcination rate increased from 17% to 65% respectively.

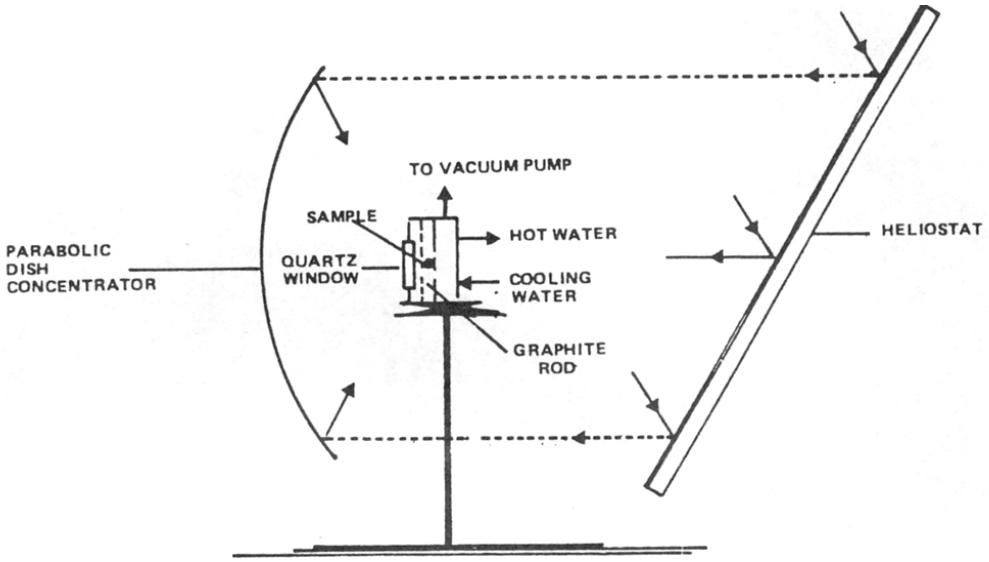

Figure 2-9: Experimental apparatus for solar energy reactions.

Source: Salman and Khraishi (1988)

Imhof (1991) selected the thermal decomposition of calcite as a representative model reaction for the long-term storage of solar energy. A different style of reactor was developed due to the technical difficulties associated with quartz or silica windows, which are expensive, brittle, require careful mounting, often fail to withstand high solar fluxes / high temperatures, and reduce the solar energy efficiency. An atmospherically open cyclone reactor, shown in Figure 2-10, was therefore suggested. This reactor would operate like a “normal” cyclone, but incorporated a different annular outlet duct, which they called a suction ring. The inner section of the suction ring allows the solar radiation to enter the cyclone, while the outer section is used to collect the evolved CO_2, the transportation air and any dust that is inevitably produced. The reactor could be rotated and positioned at any orientation, and scaled to suit the size of the heliostat reflection and concentration field as shown in Figure 2-12. Imhof concludes that, “since the optical properties of calcite are rather poor for the absorption of concentrated solar light, a combination of the suggested solar cyclone reactor with a fluidised bed (Figure 2-11) is a further development”. The objective of the modification was to enhance particle residence times and allow for longer reaction times. These three solar reactor designs are not reported to have been manufactured or tested.

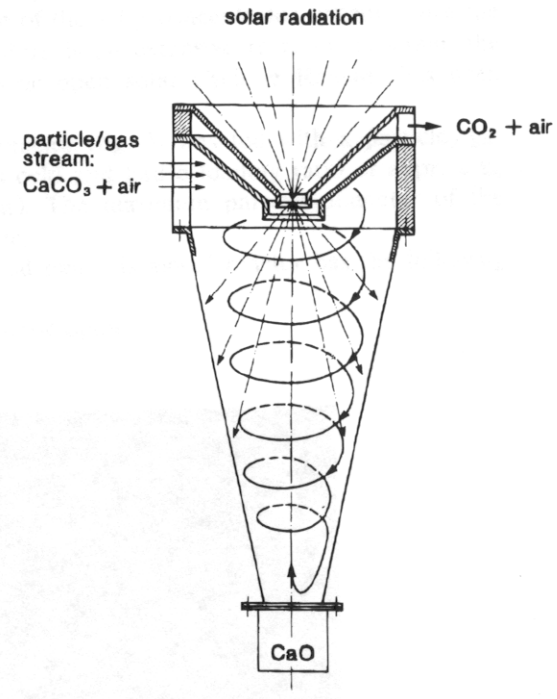

Figure 2-10: Schematic diagram of the solar cyclone reactor.

Source: Imhof (1991)

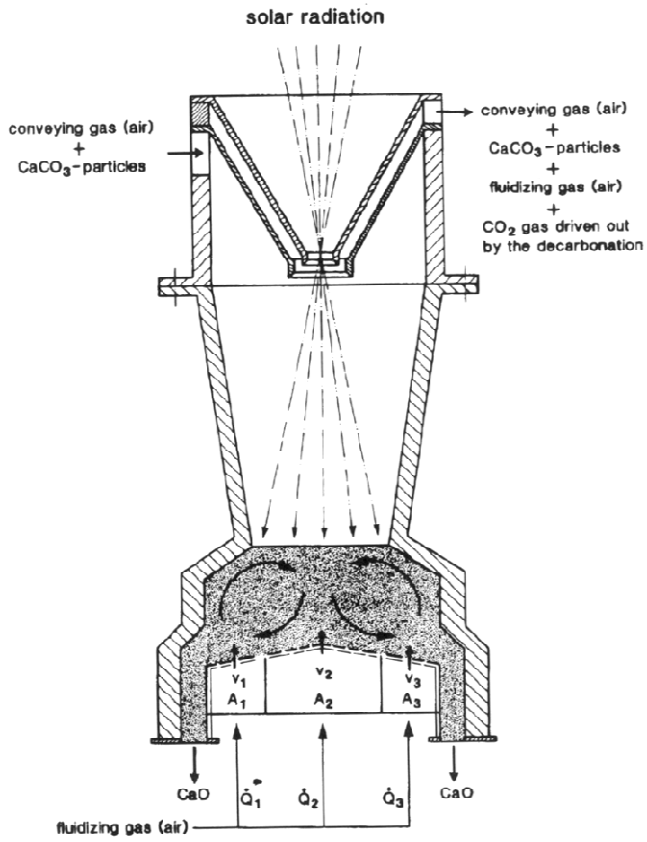

Figure 2-11: The atmospheric open solar cyclone reactor combined with a fluidised bed.

Source: Imhof (1991)

NOTE:
This figure is included on page 55 of the print copy of the thesis held in the University of Adelaide Library.

Figure 2-12: Schematic diagram of a proposed solar cement plant ~ Insert shows details of the vertical cyclonic reactor.

Source: Imhof (1991)

The High Temperature Solar Technology Laboratory (HTL) of the Paul Scherrer Institute (PSI) conducted an internal investigation of potential thermochemical reactor configurations and selected a falling particle receiver/reactor, which is described by Meier (1999). It was identified that the intrinsic drawback of the particle cloud reactors, developed previously at P.S.I., was the significant amount of additional air needed to convey the micro sized particles through the reaction zone. Heating of the inert transport air required additional energy, thus significantly lowering the efficiency of the reactor. A falling particle receiver/reactor was therefore selected from other potential configurations. The falling particle reactor concept includes a field of tracking mirrors (heliostats) used to focus the incident solar energy onto the aperture of the receiver/reactor mounted at the top of a tower, as shown in Figure 2-13. The proposed 1.5 MW furnace uses a 5 m high by 0.36 m wide curtain of free-falling solid particles (0.6 kg/s) to absorb concentrated solar radiant flux of less than 1 MW/m^2.

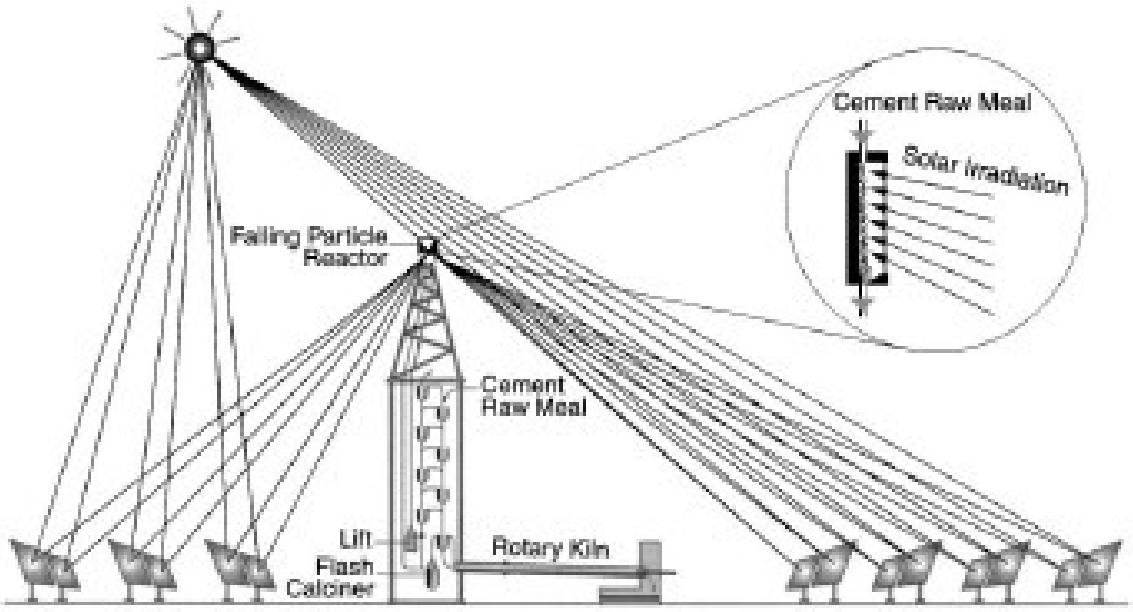

Figure 2-13: Industrial solar reactor design. Insert shows simplified schematic of the falling particle reactor for a proposed 1.5MW pilot plant.

Source: Meier (1999)

Imhof (2000) identified that the single sided falling particle receiver was not viable due to the heat losses through solar inlet opening which would significantly decrease the efficiency of the system. A revised downward facing falling particle solar reactor concept was conceived (Figure 2-14) making it possible to install a vertical transparent or opaque window, which is reported to reduce the high thermal mechanical stresses experienced with the horizontal mounting of quarts windows.

NOTE:
This figure is included on page 57 of the print copy of the thesis held in the University of Adelaide Library.

Figure 2-14: Schematic diagram of the downward facing falling particle solar reactor.

Source: Imhof (2000)

The focus of the Paul Scherrer Institute then shifted towards designing and building a 10kW solar lime rotary kiln reactor which can be seen in Figure 2-15. The reactor is 600 mm in length and 350 mm in diameter and is operated in a horizontal position. The 8cm aperture, which is shown in Figure 2-16, allows concentrated sunlight to radiate into the cavity reactor directly onto the process material. In contrast to the conventional tilted cylindrical kiln, this symmetrical horizontal reactor has a conical reaction chamber with a fixed cone angle of 5 degrees. A small silo (hopper) is placed on top of the reactor's aluminium structure and allows for storage of up to 20 kg of powdered limestone which is enough for 10 hours of continual use. A simple dozing system is integrated in the hopper structure to control the feeding rate of the raw material. The raw material is introduced from the rear of the drum reactor through a small feed pipe located directly beneath the dosing system. The mass flow rates of the dosing system range between 25 and 500 g/min. A rudimentary discharging system collects the end-product in bins open to the atmosphere.

NOTE:
These figures are included on page 58 of the print copy of the thesis held in the University of Adelaide Library.

Figure 2-16: View of the solar reactor aperture.
Source: Bonaldi *et al*. (2002)

Figure 2-15: Photo of the pilot scale solar rotary reactor system.
Source: Meier *et al*. (2002)

2.6.2 Evaluation of Existing Reactor Designs

Despite the progress, there are significant inherent issues with existing solar furnace designs used for the thermochemical decomposition of limestone. Many of these issues are outlined in Section 2.6.1 above, but are revisited in a concise format in Tables 2-3 and 2-4. The advantages and disadvantages prefixed with ⊙ are identified by the researchers within their papers, where as items prefixed with ⊕ are not identified, but are considered to be genuine considerations.

Table 2-3: Advantages and disadvantages of the fluidise bed and cyclone solar furnaces.

Type of Solar Furnace: **Fluidised Bed**	Researchers: Flamant *et al*. (1979); Imhof (1991).
Advantages: ⊙ Uniform stone heating.	
Disadvantages: ⊙ Energy consumed to fluidise the bed. ⊙ Limited penetration of solar radiation into bed. ⊙ Energy loss through windows. ⊙ Windows are brittle and require careful mounting. ⊙ Windows often fail to withstand fluctuations in high solar fluxes or high temperatures. ⊙ Windows reduce the available solar energy by reflecting certain bands of the solar spectrum. ⊙ Small limestone particles (<2mm). ⊕ Absorption of radiant energy by transport air. ⊕ Pitting and degradation of windows and subsequent reflection of solar radiation. ⊕ Cleaning and maintenance of windows. ⊕ Particle abrasion against walls, windows and other particles.	
Type of Solar Furnace: **Cyclone or Fall Particle (Flash Calciner)**	Researchers: Imhof (1991), (1997), (2000); Meier (1999).
Advantages: ⊙ Very short residence times. ⊙ Uniform radiation coverage over limestone particle surface. ⊙ Automatic product separation from carrier gas and CO_2.	
Disadvantages: ⊙ Energy consumed by transport of air. ⊙ Heat and mass loss through openings. ⊙ Small limestone particles (<2mm). ⊕ Dust formation due to particle movement. ⊕ Maintenance of receiver located on top of tower.	

Table 2-4: Advantages and disadvantages of the rotary kiln and flat bed solar furnaces.

Type of Solar Furnace: **Rotary Kiln**	Researchers: Flamant *et al*. (1979); Meier *et al*. (2002); Bonaldi *et al*. (2002).
Advantages: ⊕ Uniform radiation coverage over limestone particle surface. ⊕ Limestone particles up to 10mm.	
Disadvantages: ⊙ Heat and mass loss through opening. ⊙ High thermal gradient along kiln. ⊙ Low maximum fill ratio of limestone inside kiln. ⊕ Electrical energy consumed to rotate the kiln (although small compared to the calcination energy). ⊕ Low exposure of limestone to direct radiation. ⊕ Dust formation due to particle movement.	
Type of Solar Furnace: **Flat Bed (without particle movement)**	Researchers: Salman and Khraishi (1988).
Advantages: ⊕ No dust formation. ⊕ Unlimited limestone particle size.	
Disadvantages: ⊙ Non-Uniform stone heating.	

According to Meier *et al*. (2002) the efficiency of most solar reactors could be improved by incorporating several design changes that enable thermal energy recovery from the products. They suggest capturing the gaseous products (mainly CO_2) and using it to pre-heat the incoming furnace feed material. This is one approach to minimising parasitic losses from proposed solar furnaces. Adding to this Diver (1987) advocates making solar furnaces (reactors) relatively small and compact. He suggests that conduction and convection loss from open (no window) receivers is proportional to the internal area of the cavity, and that the magnitude of the convective loss component is comparable to the radiant loss. He also admits that making a solar furnace too small could reduce the effectiveness of the radiation

absorptance which can result in large temperature gradients which could result in structural failure. It is proposed therefore that the furnace size be determined by the heat transfer characteristics of the working fluid (limestone feed) which is normally obtained experimentally. Steinfeld and Schubnell (1993) describe a mathematical modelling method used to determine the optimum aperture size and operation temperature for a solar cavity-receiver. The desire is to improve the efficiency of energy conversion from solar radiation to the thermochemical process. The optimum aperture size is believed to result from a compromise between maximising the capture of radiation and minimising the heat losses. Although the paper does not consider that the amount of heat flux that the process feed can absorb increases with the heat transfer coefficient of the substance and decreases with increasing operating temperature.

Heat loss from a furnace system is the concern of every furnace designer. To reduce heat loss from a solar furnace, each heat mode (radiation, convection and conduction) should be retained within the furnace. The use of quartz or silica windows which allow solar radiation transmission but retain the furnace atmosphere was investigated by Salman and Khraishi (1988) and Imhof (1991). The many technical difficulties (disadvantages) associated with windows are presented above. An alternative method of solar opening heat retention therefore needs further investigation. Due to time constraints, this engineering problem will be addressed in a future detailed design of the proposed solar furnace.

Villermaux (1979) identified that the selection of solar reactor construction material is paramount to the life and effectiveness of the system. He also discusses how improvements in construction materials are required so that higher intensity heat flux can be used, and also address structural problems associated with cyclical thermal loading. The Paul Scherrer Institute and QualiCal (2000-2003) found that furnace lining construction materials were very difficult to utilise and maintain due to the high heat flux levels being used. Cracking of the refractory lining occurred at temperatures above 1250°C due to the casting of the refractory lining being too thin. The refractory lining they used has two layers of different materials; a very low density (200 kg/m^3) porous ceramic fibre insulating external lining (Refratherm 116P), and the conical shape inner surface formed by casting a very high-density (2550 kg/m^3) refractory concrete (Reframullite 70). These materials are considered by many to be extremely versatile and robust. It is therefore obvious that the design did not account for the non reversible thermal expansion on first heating and so was incorrectly installed.

Quicklime is inherently sensitive to abrasion and impacts which typically produce particles less than 75μm and can form up to 5% - 10% of the product stream Oates (1998). Airborne dust makes the furnace atmosphere optically thick which reduces the radiation path length

and therefore the available radiation for the process stream. A total reduction in the movement (rotating, turning or tumbling) of the limestone and product quicklime is desirable to avoid the formation of dust.

Significant inherent issues have been identified within existing experimental solar furnaces. To date, no commercially acceptable, industrial sized solar lime furnace has been facilitated. The fluidised bed, rotary kiln and flash calciners have received significant attention from proposed solar kiln proponents because they are extensively used for combustion driven lime manufacture. Combustion driven systems deliver energy to the process material using all forms of heat transfer dispersed over a relatively large area; where as a solar radiant system typically uses high intensity radiation over a small area. Using conventional combustion kiln configurations for solar applications does not account for the differences between the heat delivery methods. It is therefore a desirable requirement to use a furnace which is optimised for solar radiation heat transfer rather than a combustion system. Alternatively use solar energy as a significant supplement to a combustion lime kiln.

The use of solar energy to supplement a combustion driven system or as an auxiliary system has considerable merit due to the intermittent nature of solar energy. Methods to combine solar and combustion systems have been proposed for power generation systems for many years with the benefit being the cost reduction when the solar energy is introduced into a gas turbine system. These same energy cost benefits could be evident for a solar calcination furnace system.

A solar furnace which has the least identified disadvantages in Tables 2-3 and 2-4 is the flat bed solar furnace used by Salman and Khraishi (1988). The advantages of being able to process any particular sized limestone, reduces the amount of electrical energy used to crush the stone. Additionally, dust formation is minimised because the furnace does not inherently move or rotate the stone. The flat bed furnace design, such as the Calcimatic kiln, forms the basis for the proposed solar furnace presented in Chapter 3.

The effect of using a non-uniform heating source is unknown and unreported. Without periodically turning the stone, the stone on the flat bed is illuminated by radiation from only one side. Questions regarding the additional calcination time required to achieve uniform calcination and the relationships between calcination time, limestone particle diameter and the heat flux intensity arise.

2.7 Economics of Commercial Scale Solar Lime Manufacture

The economic viability of commercial lime manufacture using solar radiation has been evaluated by Imhof (1997), Imhof (2000), Riedl (2003), Meier and Cella (2004) and Stanmore and Gilot (2005). The evaluations take into consideration the costs of construction, for both the solar processing plant and the heliostat field, and the ongoing costs of production and maintenance for the expected useful life of the plant. The payback period is then calculated and an economic viability considered relative to a current equivalent conventional lime manufacturing system.

Riedl (2003) notes that full life cycle evaluations are rarely conducted, with the costs associated with decommissioning, deconstructing and disposal of the components often being neglected. She suggests that these after-production costs do not affect proposed production rates and are therefore less significant to prospective investors.

The economic evaluation of the cyclone reactor envisaged by Imhof (1997) concluded that, at that time, it was not economically viable for an industrial sized solar lime/cement processing plant to compete with conventional thermal processing methods. It was conceded that the savings in fuel consumption and the cost of removal and disposal of harmful pollutants might compensate the additional capital investment required for utilising solar energy. Imhof (2000) also suggests that increased fuel prices and a carbon tax of over 50 US$/tonne CO_2 would be required to attain no increase in product cost from the current conventional fossil fuel burning systems.

An economic assessment of the proposed solar furnace design presented in Chapter 3 will be conducted at the beginning of the detailed design stage in the future, and as such is not reported here.

2.8 Approaches to Modelling a Lime Kiln

Techniques to model and design furnaces are varied in their complexity and flexibility. According to Spalding (1963), the accuracy of any modelling technique depends on the number and boldness of the assumptions. In practice Singhal (1999) found that a compromise must be made between modelling reliability, robustness, maintainability, flexibility, cost, precision, and computational time.

Mathematical modelling plays a vital role in providing an effective means to investigate the performance of equipment as well as determine the consequences of any changes in the design, operation or control of proposed plant. A variety of mathematical modelling techniques are used commercially, ranging from computational fluid dynamics (CFD) software packages to straightforward heat and mass transfer hand calculations. According to Selcuk *et al*. (1975) the selection of a suitable modelling technique involves the consideration of the dominant modes of heat transfer within the furnace under investigation. For a solar furnace, radiation is the dominant mode of heat transfer. The thermal performance of a solar furnace therefore requires accurate prediction of both direct and indirect radiant heat transfer. The modelling techniques used most commonly include computational fluid dynamics, flux modelling and zone modelling. A brief overview of each modelling type is given in the next three sections.

2.8.1 Computational Fluid Dynamics

Most commercially available Computational Fluid Dynamic (CFD) packages have radiation analysis solution methods available. However CFD modelling, as the name implies, refers to the behaviour of fluid flow, be it a liquid or gas. The prediction of fluid flow involves the simultaneous solution of the Navier-Sokes equations for momentum conservation together with the equations for mass conservation (continuity) in the relevant coordinate directions (Viskanta and Menguc, 1987). The present project aim to reduce the amount of movement of the limestone within the furnace and avoid the formation of dust, so that the only flow of significance is derived from the evolving CO_2 from the calcination reaction. The flow of carbon dioxide driven by mild buoyancy effects and pressure gradient fluctuations within the furnace atmosphere. These movements will be slow and because the CO_2 will be approximately the same temperature as the stone may not provide significant energy transfer. The use of a coarse CFD grid would therefore suffice in this situation. The problem associated with using a coarse grid within many CFD radiation models, is that the radiation transfer is not correctly represented within the furnace especially if the atmosphere is not transparent to the entire electromagnetic spectrum i.e. CO_2 absorption of certain frequencies. To account for energy absorption by furnace atmospheric gases CFD modelling packages use a weighted-sum-of-grey-gases method for radiation exchange. The weighted-sum-of-grey-gases method approximates the total radiation emitting through the furnace atmosphere, but does not distinguish between direct and indirect radiation exchange or consider its overall directionality. For a solar furnace the direct radiation is likely to dominate

thus making the direction and magnitude of the direct radiation important to the modelling approximation.

Radiative heat transfer through media of high transparency depends on the exchange areas (or view factors) between each of the surfaces within the furnace. The internal furnace shape therefore needs to be correctly represented within the modelling package.

Another inherent limitation of CFD is that the energy balance across the entire system often does not balance well. This is because the energy balance is performed approximately across each of the very large number of computational cells. For these reasons CFD is not a tool of choice in the present research project.

2.8.2 Flux Modelling

Flux models have been one of the most widely used methods for radiative heat transfer calculations since the publication of a two-flux model by Professor Schuster in 1905 (Viskanta and Menguc, 1987). The radiation intensity is mathematically described as a function of the location, the direction of propagation and strength of electromagnetic wavelength. The need to account for the direction of radiation propagation results in large calculations because all directions must be taken into account. It is therefore beneficial to reduce the spatial directions of the radiation into separate known directions. The radiation is assumed to be uniform for all given segments within the known directions. The radiation heat transfer equation is then calculated using a series of coupled ordinary (linear) differential equations in terms of average radiation intensities or fluxes. This is known as the flux method for radiation heat transfer.

Flux calculation methods are well suited for calculating problems involving significant flow, but where radiation heat transfer is dominant. Correia (2001) notes that this is because the radiation analysis involves partial differential equations that can be conveniently solved simultaneously with equations describing the flow field. In general the accuracy of the flux approximation depends on the choice of solid-angle subdivision. Siddall (1972) explains that increasing the number of direction segments improves the accuracy of the solution but also increases the computational effort.

Three problems were identified by Viskanta and Menguc (1987), which are worth mentioning:

1). There may be no coupling between the axial and radial fluxes, which can make the governing equations unrealistic.

2). The approximations of the intensity distribution, from which the flux equations are obtained, are arbitrary.

3). The modelling equations cannot approximate highly anisotropic scattering correctly, (although it is theoretically possible).

The main flow within the proposed solar lime furnace will be the limestone feed through the system. Convectional flow of the CO_2 will be minimised to help reduce one of the main heat losses, as identified earlier in this Chapter. Modelling using a flux modelling method would therefore be a computationally tedious method for modelling this particular solar furnace design.

2.8.3 Zonal Modelling

The zone method is a relatively simple modelling technique used for radiation analysis. It has been used by Vercammen and Froment (1980), Ward *et al*. (1999), and Correia (2001) in mathematical models, which describe a range of industrial heating processes where thermal radiation dominates. It is recognised by many kiln and furnace designers such as Selcuk *et al*. (1975), Viskanta and Menguc (1987) and Jenkins (2002) as a rigorous, reliable, tried and tested numerical method for the calculation of thermal radiation heat transfer in practical systems.

Originally developed by Hottel and Cohen (1957) and then revised further into the modern mathematical technique by Hottel and Sarofim (1967), the zone method calculates energy transfer within a non-isothermal furnace by dividing it into a series of discrete isothermal zones bounded by surfaces, each with a constant, but separately defined, temperature and radiative properties. The energy balances in the zone method yield a set of non-linear equations that can be solved simultaneously to provide the temperatures and/or heat fluxes between the surfaces. These can then be used to calculate the thermal performance of the furnace. Viskanta and Menguc (1987) describe how the zonal modelling technique can account for the absorption of certain frequencies of the electromagnetic spectrum by certain grey gases (CO_2, H_2O etc), as well as the absorption and partial reflection of the refractory surfaces and any process material within the furnace. The integral approach adopted in this method treats radiation in the enclosure in a global manner so that reliable estimates of radiative heat transfer can be obtained (Tucker, 1990).

The zone method used by Rhine and Tucker (1991) does not provide a total system description of the thermo-physical process involved. The model input for the overall energy

balance must include any addition or loss through chemical reactions, any inconsistent concentrations of furnace atmosphere and of course the mass flows in, and across, each zone to account for enthalpy exchange. Correia *et al*. (2000a) explain that it is therefore necessary to link the conservation of momentum, mass and energy to the zone model to achieve a balanced model.

An advantage of this method over CFD and flux techniques as described by Correia *et al*. (2000b) is that due to its low computational demand it can be readily adapted to simulate the non-steady state behaviour of intermittently operated systems. This is achieved by sequentially applying the zone model at discrete time intervals throughout the period of operation. Non steady state prediction is particularly important with a solar furnace design, due to the varying nature of solar energy. In these circumstances, the zone method of radiation analysis is likely to be the most appropriate modelling technique for many solar furnaces.

The quality of the output data from zone modelling depends on the number and placement of the zones within the model. Correia (2001) describes how the number of zones significantly affects the predicted thermal performance of both continuous and transiently operated furnaces. The problem arises when increasing the number of zones, which increases the number of exchange areas and therefore the mathematical complexity of the model. There are therefore three main types of zone modelling techniques recognized, the single gas zone, the long furnace zone and the Multi-Dimensional Zone.

The single gas zone model, also commonly referred to as a well stirred furnace model or zero-dimension Hottel model, is the analysis of the entire furnace enclosure as a complete zone. That is, the walls, roof and floor of the furnace are the surface zones (or boundary) of the model, and the modelling body is the gas volume within the furnace.

The long furnace modelling technique is a more complex version of the single gas well-stirred zone model. The model can be described as a linear connection of single gas zone models. There is a stepwise variation of gas and surface temperatures in the longitudinal, or x direction. It is therefore referred to by Rhine and Tucker (1991), and Correia (2001) as a one-dimensional model. Hottel and Sarofim (1967) note that there is a strong correlation between the long furnace model and a plug flow model. It is to be used where there is a continuous change of temperature in the longitudinal direction.

The multi-dimensional zone model is a further development of the long furnace model. The spatial variation of temperature and heat flux in both the longitudinally and cross-section (or radial) direction is conducted. For an axi-symmetrical geometry furnace, the multi-

dimensional zone model is a two-dimensional (2D) representation. A three-dimensional (3D) analysis would include heat flux variations in the cross sectional plane, i.e. heat flux differences in the horizontal and vertical directions.

2.8.4 Summary of Modelling Approaches

The advantages and disadvantages of using various mathematical modelling techniques were contemplated before selection of a suitable 'package'. These are shown in Table 2-5.

Each approach has its merits depending upon the design requirements, the practical experience of the designer, the mathematical and computational ability of the designer and, of course, on the economic situation. According to Rhine and Tucker (1991) the simplest techniques, like the single gas zone model, have only limited accuracy and detail, but provide quick solutions and a basis for the more complex approaches. However the multi-dimensional zone method is best suited to modelling of solar furnaces because it can be used to represent relatively complex furnace shapes without excessive computational effort or time. It also produces a realistic representation of both the direct and indirect radiation transfer within the furnace enclosure.

Table 2-5: Comparison of the advantages and disadvantages of thermal radiation modelling techniques for solar furnaces.

Model Type	Advantages	Disadvantages
Computational Fluid Dynamic (CFD)	• Only requires Initial and Boundary conditions • Adaptable to numerous configurations • Well established as a commercially available tool	• Initially difficult to learn • Large amount of output data • Very high computational power required to model an industrial process. • Potentially long computational time • Does not close the enthalpy balance of the furnace • Not suitable where there the dominant heat transfer is independent of flow.
Single-Gas-Zone	• Simple to use • Flexible • Run time small • Hand calculation possible	• Spatial heat flux variation ignored • Limited accuracy
Long Furnace Zone	Same as Single Gas Zone plus: • Adaptable to many geometries • Transient and steady state	• Inter-zonal radiation ignored (Type 1) • Large number of exchange areas to calculate • Requires consistent 1-D furnace shape
Multi-Dimensional Zone	Same as Single Gas and Long Furnace Zone plus: • Realistic representation of radiation	• Large amount of data • Not easily adaptable • Moderate computational power (but much lower than CFD)

2.9 Conclusions from the Literature Review

This chapter presented an overview of the issues and mechanisms that have been identified as technical and design constraints to a successful, commercial solar lime manufacturing system. It has been established that significant new knowledge is required before the solar

thermal possessing of limestone can become commercially viable. In particular it was identified that any proposed solar furnace should maximise the direct exposure of the limestone to the solar radiation, while carefully controlling the heating rate and minimising the build up of CO_2 within the furnace.

To achieve large production rates the small thermochemical solar reactors identified by Villermaux (1979) can not be used. A critical analysis of industrial scale solar lime furnaces is presented in Tables 2-3 and 2-4. It identified many advantages and disadvantages of several designs, such as rotary kilns and fluidised bed reactors that have been used on a laboratory scale for continual feed experiments. The rotary kiln allows the escape of radiation and convective flows through the ends of the cylinder as well as having a high thermal gradient along its length. Meier *et al*. (2002) and Bonaldi *et al*. (2002) also identified significant mass loss through the solar opening of the rotary kiln. The fluidised bed consumes considerable energy maintaining stone movement as well as allows radiant heat loss through windows. This heat loss was identified by Flamant *et al*. (1979), Salman and Khraishi (1988) and Imhof (1991) as being one of the major heat losses from the system. The use of windows also inhibits solar radiation transmission due to dust formation and abrasion of the surface which naturally occurs over time.

A solar furnace which minimises stone movement, dust formation, and can accept varying limestone sizes is desirable for optimising radiant exchange and minimising electrical energy use. One such conventional kiln system, which has not previously been evaluated for solar energy is the Calcimatic kiln. This kiln uses a flat bed travelling grate which can accept various sized limestone and provide precise control over the feed flow.

Section 2.3 of the literature review identified that the calcination of limestone using conventional fuel based furnaces is effected by the furnace temperature, the heating rate, the size of the limestone particle and the partial pressure of CO_2 within and surrounding the calcining stone. The calcination of limestone using solar radiation requires similar considerations with the addition of allowance for radiation intensity, uniformity of the radiant heat flux and uniformity of heating over the stones surface. It is evident that no systematic evaluation has been performed on the independent influence of radiation intensity, stone size and exposure time on the calcination rate of small to medium sized marble / limestone.

A heat transfer based mathematical model was used by Lipinski and Steinfeld (2004) to evaluate the calcination of limestone being heated by solar radiation. The model was based on the homogeneous uniform conversion model which does not consider a calcination front or intra-particle effects within the sample. An alternative approach by Hancock (2002) used

the SCM equation developed by Hills (1968) in their one dimensional solar calcination model. This model evaluated a rectangular particle but neglected mass transfer and ends effects. A standard SCM assumes uniform heating over the stones surface which does not represent solar heating. It is therefore proposed to use a modified version of a heat transfer based SCM for the present solar calcination modelling.

The review of the controlling parameters used for lime furnace design identified that the furnace size and shape have a significant effect on the production rate and energy consumption. It is desirable to optimise a particular furnace design for the direct usage of the primary energy, by investigating the effects of changing kiln structural dimensions and shapes. Several separate investigations are reported which focus mainly on specialised solar thermal reactors. Apart from the solar rotary kiln (Figures 2-6 and 2-15) the remaining solar furnaces were specifically designed as solar chemical reactors. Mathematically modelling the heat transfer within various furnace shapes can be used to determine which shape(s) optimise the transfer of heat to the process material. Various modelling packages are available and can be used for kiln and solar furnace analysis. The Hottel zonal model offers a relatively simple modelling technique for radiation analysis.

This literature review has identified several key gaps in the knowledge base which are now used to form the aims and objectives of the present research.

2.10 Aims and Objectives of the Current Research

This research is being conducted to answer fundamental questions about minerals processing using solar energy as well as address some of the issues regarding the effectiveness of using concentrated solar energy for the primary heating source for the thermal calcination the limestone. The aims of the proposed PhD research are:

- To develop a mathematical model for the analysis of process efficiency to directly compare combustion driven lime manufacture with solar lime manufacture.
- To use a zero-dimensional thermal radiation Hottel model to evaluate the effects of changing the solar furnace length, cross sectional shape, limestone bed coverage on the heat transfer to the limestone feed. Also quantify the heat losses through openings in the furnace walls (or roof) which allow feed-stock flow and the inlet of solar radiation.

- To determine a method for measuring the radiant heat flux being supplied to the experimental solar furnace during the experimental aspects of this research.

- To experimentally quantify baseline calcination rates for small to medium sized Penrice marble for furnace temperatures between 900°C and 1000°C. Also evaluate the effects of limestone bed depth on the bulk rate of calcination for the same furnace temperatures.

- To experimentally investigate the effects of local radiation intensity on the calcination kinetics as a function of stone size.

- To experimentally quantify the benefits to calcination rate in using an enclosed solar furnace.

- To develop a multi-zone two-dimensional thermal radiation zonal model to simulate the radiation source and resulting heat flux on the limestone within the open system and enclosed solar furnace experimental apparatus.

- To develop and validate a mathematical calcination model which represents the non uniform (single sided) heating which occurs due to the radiation source heating.

The major research objectives of the project are therefore to develop and validate a useful mathematical description of a solar furnace for the calcination of limestone. The knowledge gained from this investigation can be used to conduct a conceptual design of an industrial scale solar lime facility.

Chapter 3

Zero Dimensional Studies of a Solar Lime Furnace

3.1 Introduction

The design of a new solar furnace should incorporate the best of existing lime burning facilities where appropriate and include newly developed solar technology and techniques. The development of a theoretical model to analyse alternative solar furnace designs is therefore advantageous. This chapter presents a process efficiency analysis and a zero dimensional modelling technique to analyse various solar furnace designs.

This chapter begins with a comprehensive theoretical analysis of the energy requirements within various 'chambers' of a generic lime kiln, as seen in Figure 3-1. The process efficiency analysis is used to calculate and compare the energy consumption and available heat recovery within furnaces which use either conventional fossil fuels or solar energy as the heating source.

Zero dimensional zone models are then used to calculate the variations in energy efficiency for different shaped solar lime furnaces. The energy efficiency analysis is used to compare furnace shapes which have various cross sectional dimension and also the affects of altering the aspect ratio (length to width ratio) on this efficiency. These analyses include the radiation heat losses from the furnace through the inlet and outlet openings and the convective heat losses from the furnace structure.

The zone method is a relatively simple modelling technique used for radiation analysis. The single gas zone model, also commonly referred to as a well stirred furnace model, or zero-dimension Hottel model, is the analysis of the entire furnace enclosure as a single zone with uniform properties. That is, the walls, roof and floor of the furnace are the surface zones and the furnace volume being the gas zone. This simple modelling technique is useful for broad assessments and can predict trends as furnace parameters are altered. From these analyses, furnace configurations which show beneficial characteristics are selected for more detailed analysis.

The chapter concludes with a discussion and summary of the results.

3.2 Theoretical Energy Requirements for Quicklime Production

3.2.1 System Requirements for Conventional Energy

A mathematical model was developed to simulate the flow of heat and mass through a typical lime manufacturing process. The heat and mass balance analysis compares the energy efficiency of using a range of different energy sources including general-purpose coal, coke, heavy fuel oil, and methane. This analysis is conducted on a generic kiln, which consisted of three zones, a preheating zone, a calcining zone, and a cooling zone as represented in Figure 3-1. This kiln representation is applicable to any lime making technology, e.g. rotary kiln, shaft kiln, tunnel kiln or Calcimatic kiln. The mathematical procedures presented here are similar to those of Dorman (1979).

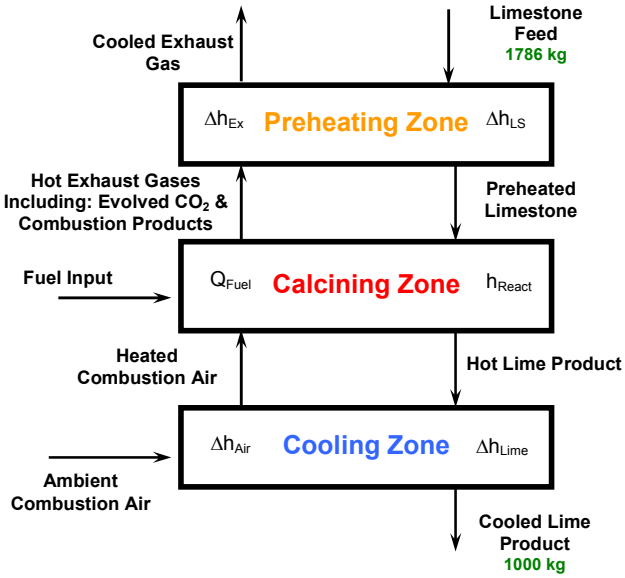

Figure 3-1: Energy and mass flow diagram for a typical fossil fuel burning lime-producing system.

The heat and mass flow process through the kiln is as follows: The limestone feed enters the preheating zone where it is preheated by the kiln's exhaust gases. If this preheating process were to be 100% effective, the limestone could theoretically reach the 900°C calcination temperature before entering the calcining zone. After being used to preheat the stone, the cooled exhaust gases are then expelled. The pre-heated limestone moves into the calcination zone where the stone is exposed to high heat fluxes from the combustion of a fuel (or from solar radiation). The thermal decomposition reaction of the limestone occurs within the calcination zone where quicklime product (CaO) and carbon dioxide (CO_2) are produced. The quicklime product moves in to the cooling zone, where the combustion air is preheated by the hot lime. If the recovery process within the cooling zone were 100%

effective, all of the heat from the hot lime product could be recovered and used to preheat the combustion air. Having been preheated, the combustion air is transported to the calcination zone, where it can be fed into the burner and used as a primary and or secondary air supply. The combustion air mixes with a fuel which is subsequently combusted and supplies the heat flux required for the thermochemical decomposition of the limestone. The combustion process produces combustion gases which mix with the evolved CO_2 from the calcination reaction and form the exhaust gases. This exhaust gas mixture is then used to preheat the incoming limestone feed.

3.2.2 Assumptions Used in the Energy Balance

Several assumptions are made in this analysis, which represents a conservative idealistic scenario. The main assumptions used in this mathematical analysis include:

1. All gases and process materials are homogeneous and at equilibrium.
2. Kinetic and potential energy effects neglected.
3. The exhaust gas temperature out of the calcination zone is 900°C.
4. The adiabatic flame temperature is neglected.
5. The quicklime temperature out of the calcination zone is 900°C.
6. All heat transferred from the fuel is independent of the transfer mechanism. Therefore all the heat contained within the fuel is available for the process.
7. Effectiveness of heat transferred between hot and cold bodies is ideal, i.e. all energy that is available for heat transfer is transferred.
8. No heat losses from the furnace structure.
9. Stoichiometric air for combustion and complete combustion occurring.
10. No water present within the limestone.
11. No heat transfer from the H_2O within the combustion exhaust gases.

Two different heat transfer effectiveness scenarios were conducted. The assumption for the first scenario is that ideal heat transfer occurs at all stages during calcination, and also in the preheating and cooling zones of the kiln. That is, the effectiveness of the heat exchanges is 100%. The second scenario assumes that the effectiveness of the heat exchanges within all the pre-mentioned zones is only 80%. The 80% figure has been chosen as being typical of that found in many industrial kilns. This scenario therefore provides a more realistic

representation of the energy requirements, which can then be used as a starting point for the basic zone model.

3.2.3 Heat and Mass Balance for Conventional Lime Kilns

Theoretically, to produce one tonne of calcium oxide, CaO (quicklime), 1786 kg of calcium carbonate, $CaCO_3$ (limestone) is required, with 786 kg of CO_2 being released during the decomposition. The complete decomposition of $CaCO_3$ requires approximately 3027 kJ/kg CaO of heat at a temperature of around 900°C (1173K) as provided by Oates, (1998). Using the average value for specific heat for limestone, the total heat required to preheat the $CaCO_3$ is 1.114 kJ/kg.K × (1173 – 295) = 1,747,135 kJ/tonne CaO. The total heat required for heating and calcining is therefore 3,027,056 + 1,747,135 = 5,967,740 kJ/tonne CaO which rounds to 5,968 MJ/tonne CaO. The remaining calculations will display numbers rounded to 4 significant figures.

The heat contained within the hot quicklime and carbon dioxide products can potentially be recovered and utilised to preheat the combustion air and the feed stone respectively. A counter current 100% effective heat transfer system would recover 1000 kg × 0.972 kJ/kg K × (1173 – 295) = 853.4 MJ/tonne CaO from the CaO, and 786 kg × 1.058 kJ/kg K × (1173 – 295) = 729.9 MJ/tonne CaO from the evolved CO_2 giving the theoretical limit of total recoverable energy as 1,583 MJ/tonne CaO.

The combustion properties of four fuels, general purpose coal (902), coke, heavy fuel oil, and methane that are chosen for this analysis can be seen in Appendix A. As an example though, the stoichiometric combustion of 1 kg of methane (natural gas) requires 17.2 kg of air and theoretically produces 55.5 MJ of energy and 18.2 kg of combustion products. The minimum total methane consumption is therefore 60 kg fuel/tonne CaO × 55.5 MJ/kg methane = 3337 MJ/tonne CaO. For an 80% effective process, the minimum total methane consumption is 4761 MJ/tonne CaO (or 86 kg per tonne of CaO produced).

The high temperature combustion exhaust gases and the evolved CO_2 from the calcination reaction are used to preheat the incoming limestone. The energy content of these vented gases combined is 1922 MJ/tonne CaO (or 2556 MJ/tonne CaO for 80% effectiveness). This exceeds the energy required to preheat the incoming limestone, so the vent gases leave the furnace at a temperature of approximately 102°C.

Heat and mass balances were conducted around each chamber of the kiln for each fuel type. Table 3-1 provides a comparison of some of the more important results found from the heat

and mass balance calculations for the fossil fuel-fired kilns. These calculations have been sorted in descending order of mass of fuel consumption. Full details of the parameters used to produce this table are shown in Appendix A.

Table 3-1: Calculated results from energy balances using various fossil fuels as the heating source for lime furnaces.

80% Effective heat transfer ~ in **Bold** Ideal situation ~ in brackets	**General-purpose coal** (22,600 kJ/kg)	**Carbon fuel (Coke)** (32,780 kJ/kg)	**Heavy fuel oil** (44,200 kJ/kg)	**Methane (Natural Gas)** (55,536 kJ/kg)
Mass of Fuel Consumed (kg/tonne CaO)	**221** (155)	**148** (104)	**101** (71)	**86** (60)
Nett Energy Consumption (MJ/tonne CaO)	**4997** (3503)	**4866** (3411)	**4484** (3143)	**4761** (3338)
Mass of Combustion Air (kg/tonne CaO)	**1736** (1217)	**1711** (1200)	**1370** (960)	**1475** (1034)
Combustion Air Preheat Temperature (K)	**654** (934)	**659** (944)	**750** (1105)	**717** (1048)
Quantity of Exhaust Gas (kg/tonne CaO)	**2742** (2158)	**2646** (2090)	**2257** (1817)	**2346** (1880)

The results of the idealised analysis provided trends rather than absolute values. As can be seen from Table 3-1, there is an inverse relationship between fuel calorific value and mass of fuel consumed, which is fairly intuitive because the energy quantity requirements for the calcination process does not change. Less obviously, even though the air/fuel ratio of coal is lower than that for methane (7.85 as opposed to 17.2), there is a direct relationship between the mass of combustion air and the mass of exhaust gas produced. This indicates that using a low-grade (low calorific value) fuel, produces more exhaust gases, thereby increasing the quantity of carbon within the gas and thus increasing its greenhouse gas emission.

The choice of fuel type is usually process specific and can have a significant effect on furnace performance (Mullinger and Jenkins, 2008; pg 81). It should be noted that the mode of heat transfer is ignored within this heat and mass balance calculation. In most high temperature industrial processes, heat transfer through radiation is significantly more than through convection and conduction. For lime manufacture, a luminous, highly radiant flame

increases heat transfer to the feedstock, and an increase in process efficiency can be achieved. The result being a reduction in overall fuel consumption. Therefore the specific energy consumption for lime manufacture (kW/tonne CaO) in order of highest to lowest would be natural gas, heavy fuel oil, coal and then coke. This is different than is seen in Table 3-1.

For all the 80% effective cases, the heat recovered from the lime product is insufficient to raise the combustion air temperature to 900°C; the temperature required for the calcination reaction to occur. The combustion air therefore requires additional energy, supplied by using additional fuel, to increase its temperature to the 900°C kiln temperature. Further analysis and comparison of these results is provided in Section 3.2.6.

This same heat and mass balance technique has been applied to a lime kiln which uses solar energy as the heat source rather than fossil fuels. This analysis will be used to better quantify the characteristics of solar lime furnaces and provide a theoretical comparison.

3.2.4 Heat and Mass Balance for Solar Lime Furnaces

Three separate heat and mass balance calculations were conducted to evaluate the effects of using solar energy as the sole heat supply for the manufacture of lime. These balances use the same calculation methods and assumptions as were used for the fossil fuelled systems in Section 3.2.3.

The three solar balance cases differ in their use of air as a heat recovery medium. The first system utilises enough air to fully preheat the limestone feed, the second uses no air for heat recovery, and the third uses enough air to recovery all of the heat in the lime product but not enough to fully preheat the limestone feed. The general heat and mass energy flow diagrams for the three solar cases are seen in Figures 3-2 to 3-4.

The first solar system evaluated by the heat and mass balance represents the direct replacement of a fossil-fuelled system with solar energy, as can be seen in the process diagram, Figure 3-2. The same mass flows are used between each zone, including the combustion air, which is now redundant for the combustion process, but is still utilised to collect energy from the cooling zone and transfer it to the preheating zone. To fully preheat the limestone to the 900°C furnace temperature, a mixture of the evolved carbon dioxide from the calcination reaction and a specific quantity of preheated air from the cooling zone is used. The quantity of air is calculated by considering the sensible heat required to preheat the limestone feed. Similar to the air preheating zone for the combustion kilns, the

temperature of the heated air received at the solar calcination zone is not 900°C owing to the amount to heat available from the lime product. Therefore some solar energy is used to increase the air temperature within the calcination zone. The significant results from the analysis can be seen in Table 3-2 and a full list of parameters in Appendix A.

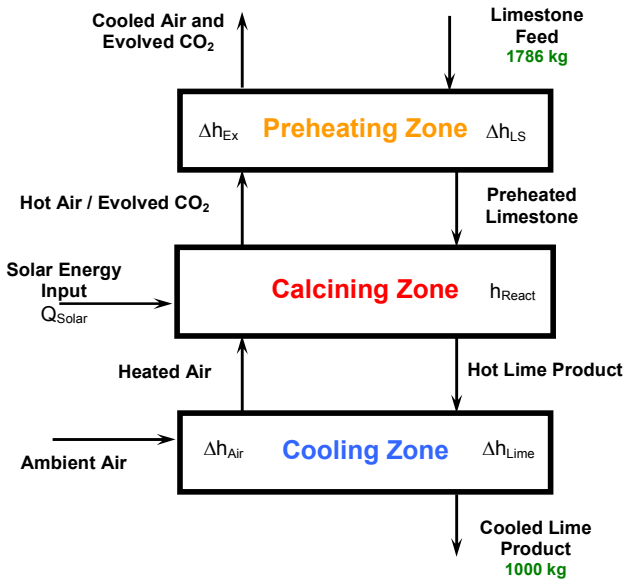

Figure 3-2: Solar system evaluation case 1: Generic lime kiln with sufficient air to fully preheat the limestone.

The second solar system evaluation by a heat and mass balance, seen in Figure 3-2, does not use any air to preheat the limestone. It uses only the evolved CO_2 from the calcination zone as the sole heat transfer medium. The heat capacity of the CO_2 is insufficient to fully preheat the incoming limestone, therefore additional solar energy is required to bring the limestone up to temperature before the calcination reaction begins. In addition, the heat contained in the hot lime product is completely lost from the system.

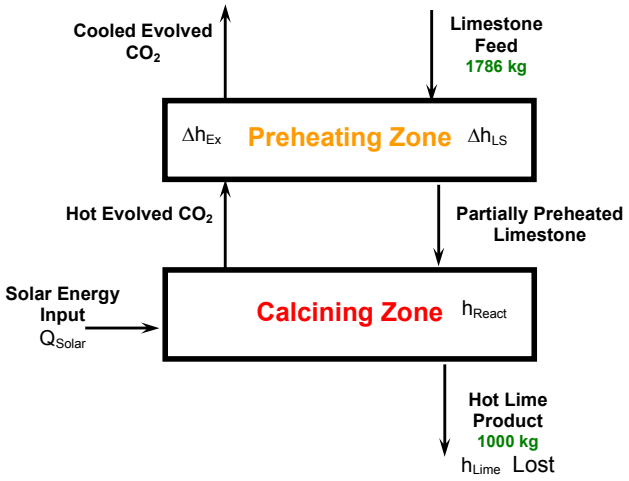

Figure 3-3: Solar system evaluation case 2: Evolved CO_2 as sole preheating medium, heat from hot lime product lost from system.

The third solar heat and mass balance evaluation, which can be seen in Figure 3-4, uses an air bypass system to transfer the heat from the lime product to the limestone feed. The heat transfer air stream bypasses the calcination zone and is directed into the preheating zone to preheat the limestone feed. The evolved CO_2 from the calcination zone is also utilised to preheat the limestone feed within separate preheating chambers within the preheating zone. A multi-chamber preheating zone separates the air and CO_2 streams using a series of baffles to minimise the amount of gas mixing and therefore maintain a relatively pure CO_2 stream.

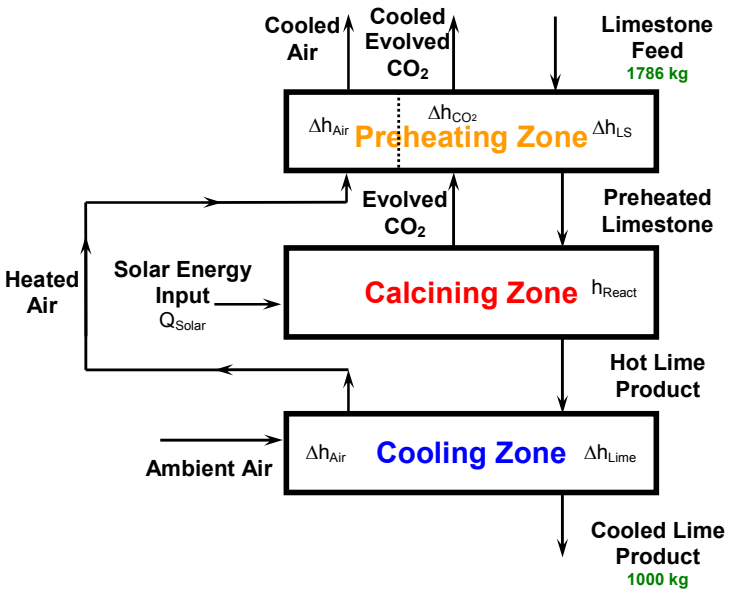

Figure 3-4: Solar system evaluation case 3: Heated air bypasses calcination zone. Evolved CO_2 used for preheating limestone within separated chamber.

An alternative system similar to Case 3, as displayed in Figure 3-5 could recycle the cooled CO_2 from the preheating zone back into the cooler to recover the heat from the lime product. The exhaust gas stream could therefore be kept reasonably homogenous in CO_2 without the need for separation of the two exhaust gas streams. A significant drawback of this system is that a substantial amount of re-carbonation that may occur within the cooling zone, which is undesirable. The process efficiency analysis for this system was therefore not conducted.

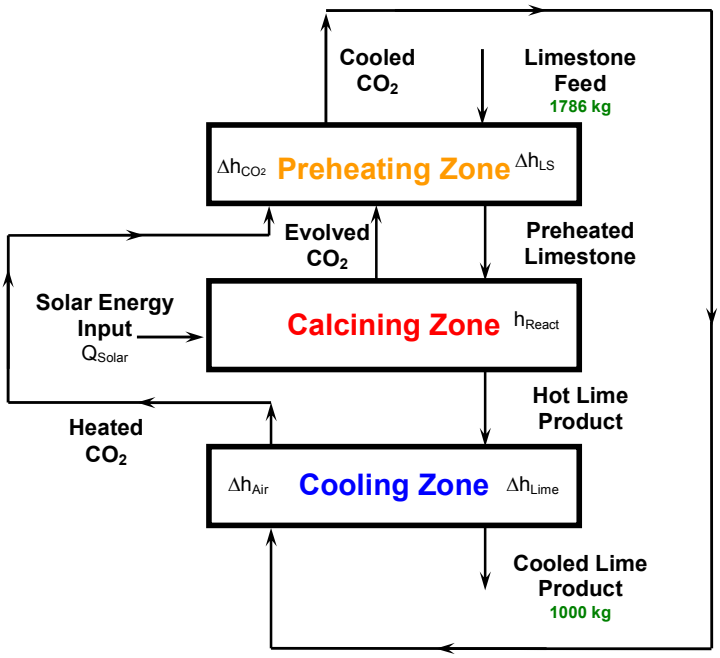

Figure 3-5: Alternative case 3 solar system: Preheated CO_2 bypasses calcination zone and preheats the limestone feed.

Table 3-2 compares some of the more important results found from the energy balances conducted for the three different solar furnaces. The bold numbers show the 80% effective heat exchange scenario, while the bracketed numbers are for the ideal situation. The full version of the tabulated parameters is shown in Appendix A.

Table 3-2: Results from energy balance analysis of three solar energy lime furnaces with 100% and 80% effective heat transfer.

80% Effective heat transfer ~ in **Bold** 100% Effective heat transfer ~ in parenthesise	**Energy Consumption** (MJ/tonne CaO)	**Mass of Air** (kg/tonne CaO)	**Air Temperature Entering Preheat Zone** (K)	**$CaCO_3$ Preheat Temperature** (K)	**Mass of Exhaust Gas** (kg/tonne CaO)
Case 1 Air heat transfer stream through calcination zone	**4560** (3197)	**1520** (1063)	**705** (1027)	**1173** (1173)	**2306** (1849)
Case 2 No air heat recovery from lime	**5384** (4044)	ZERO	NR	**588** (662)	**786** (786)
Case 3 Air stream bypass and separate CO_2 stream	**4560** (3197)	**709** (886)	**1173** (1173)	**929** (1088)	**1495** (1672)

3.2.5 Analysis of the Solar Furnace Heat and Mass Balances

As can be seen in Table 3-2, the energy consumption is highest for the solar with no-air heat recovery, Case 2. This is due to the stored energy in the hot product not being recovered. Therefore an additional 824 MJ per tonne of CaO is required to preheat the $CaCO_3$ prior to achieving calcination. Cases 1 and 3 show the advantages of using heat recovery from the product.

Direct contact heat exchange between the lime product and limestone feed is not possible because the two streams would become intimately mixed. However a fluid passing over the stone can be used, such as in cases 1 and 3 where air is used. With this type of heat exchanger and with a recovery effectiveness of 80%, the amount of solar energy consumption could be reduced to around 4560 MJ/tonne of CaO; a 15.6% improvement in the energy consumption compared to the no heat recovery, case 2.

Cases 1 and 3, where air is used for heat recovery, have the same energy consumption but differ in the mass of air used. Case 3 shows that the limestone does not become fully preheated. The additional energy required is transferred directly via the radiation illumination rather than through the use of additional air. A saving of 811 kg of exhaust gases per tonne of CaO is achieved.

3.2.6 Comparison of the Heat and Mass Balances

The histogram seen in Figure 3-6 compares the calculated nett energy consumption for the energy sources analysed within these heat and mass balances. The consumption is based on a constant mass (1000 kg) of limestone which (theoretically) produces 786 kg of quicklime. The graph shows that the solar systems compare favourably with the fossil fuel systems if heat recovery is used. Although it should be noted that this analysis is for a steady state operation and therefore does not include the energy (or time) required to preheat the calcination chamber, which could be detrimental to production when using the solar system.

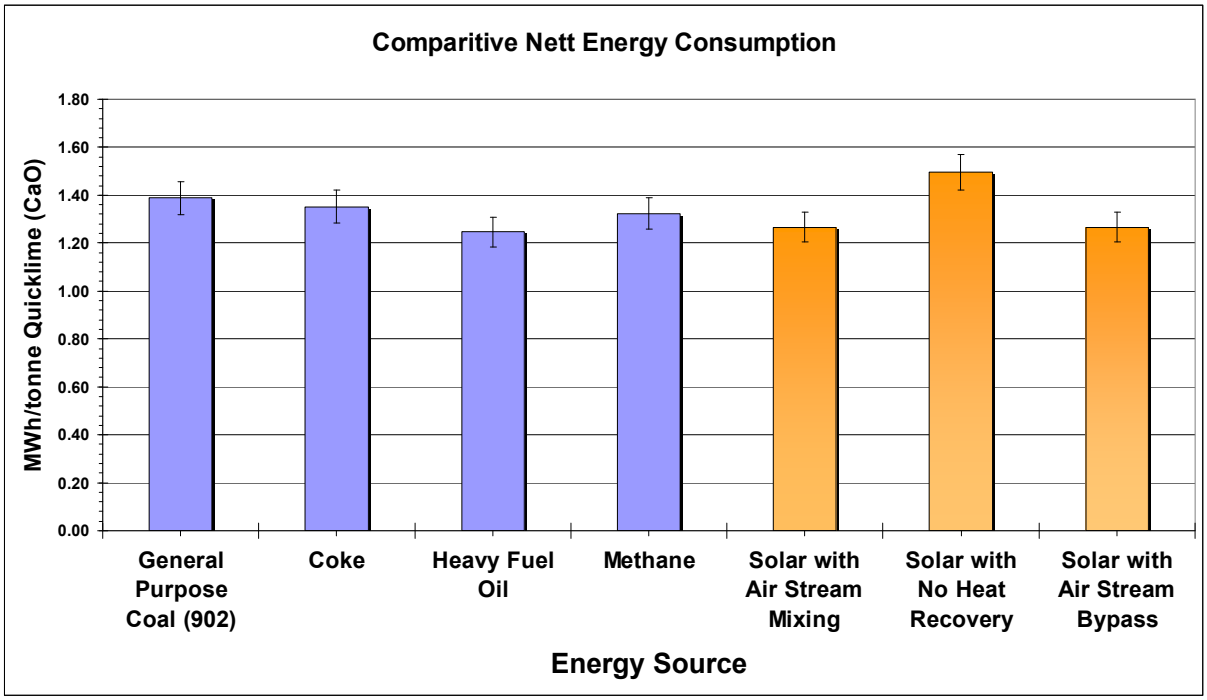

Figure 3-6: Calculated comparative nett energy consumption for a typical lime manufacturing process using different forms of energy based on a constant mass of limestone.

3.2.7 Conclusions from the Process Efficiency Analysis

The main conclusion that can be drawn from this process efficiency analysis is that the thermal efficiency of a solar energy supplied lime manufacture system can compare favourably with the best fossil fuelled system. Good heat recovery from the processed stone as well as a comprehensive preheating system is desirable to minimise the energy losses from the system.

If the exhaust gas contained solely CO_2, it is ideal for collection and subsequent utilisation or sequestration, without costly scrubbing and or separation. Although there is not enough energy within the CO_2 to fully preheat the limestone. The best efficiency requires some additional air. It may be possible with an effective baffle or 'chambering' system within the pre-heater stage to minimise the mixing of the two exhaust gas streams: air and evolved CO_2.

The '*Solar with Air Bypass*', Case 3, is considered a more desirable system because it provides the potential for a homogeneous CO_2 exhaust gas stream. It may be possible, with an effective heat recovery system, to recover the energy from the lime product and use it to preheat the incoming limestone feed. Mixing of the CO_2 gas stream from the calcination reaction and the heat transfer air stream could be minimised within the pre-heater zone by using a series of batch chambers.

3.3 Furnace Design Using a Zero Dimension Thermal Radiation Hottel - Zone Model

Having established that using solar energy with effective heat recovery provides a thermally viable option, the next stage is to determine which furnace shape can make best use of concentrated solar energy. An appropriate furnace shape is one which maximises the heat transfer to the bed while minimising losses. The zero-dimension "Hottel" zone model provides a useful preliminary method to estimate and characterise trends in furnace efficiency as a function of key input parameters (Jenkins, 2002).

Jenkins (2002) documents that the zero dimensional (0-D) modelling was first developed by G. A. Orrok in 1925, with a view to providing a useful formula to increasing furnace efficiency. Hottel and Sarofim (1967) revised and adapted the formula for application to simple furnace designs which can be represented as a 'well-stirred' enclosure. This modelling technique considers the furnace as a 'black box', as shown graphically in Figure 3-7. An energy balance is then conducted around the box, to quantify the input and output energies. Depending upon the characteristics of the input energy (combustion or solar), the thermal properties of the furnace structure walls, the characteristics of the process material (sink), and also considering any other losses (openings, etc), the distribution of output energy is calculated.

Figure 3-7: Representation of the 0-D zone model.

The zero dimensional modelling technique assumes the furnace consists of a single homogeneous gas volume, which exhibits constant thermodynamic properties. This is a reasonable assumption for a solar furnace with an atmosphere which contains only the carbon dioxide product and that the process material (limestone) is fully preheated. The furnace walls and sink are represented as an intimately mixed surface (i.e. speckled wall) which also has constant thermodynamic properties.

The original equation by Hottel and Sarofim (1967, page 461) shown here as Equation [3.1], is the simplified well-stirred furnace model.

$$Q'D'+\tau^4 = (1+\Delta'-Q')^4 \qquad [3\text{-}1]$$

Which equates the following dimensionless groups:

Q' = reduced furnace efficiency,

= the actual efficiency Q/H_F × the temperature ratio $\frac{T_{AF}-T_o}{T_{AF}}$

D' = reduced firing density,

= the ratio of energy input to a type of radiating ability,

$$= \frac{H_F}{\sigma(GS_1)_R T_{AF}^3 (T_{AF}-T_o)}$$

τ = ratio of sink temperature T_1 to pseudo-adiabatic flame temperature T_{AF}

Δ' = the ratio of gas temperature drop (from radiating point to chamber outlet), to the adiabatic flame temperature.

$$= \Delta/T_{AF}$$

The limitation to Equation [3-1] is that it does not make allowance for any structural losses. The equation was therefore revised and improved by Hottel (1974), to allow for the radiative and conductive heat losses through the walls and, also any furnace openings. The revised design Equation [3-2], as reported by Jenkins (2002) matches general furnace performance data reasonably well, with an error band of approximately ±5%.

$$\mathbf{Q'D'} = \left(\mathbf{1}-\frac{\mathbf{Q'}}{\mathbf{d}}\right)^4 - \tau^4 + \mathbf{L_R'}\left[\left(\mathbf{1}-\frac{\mathbf{Q'}}{\mathbf{d}}\right)-\tau_o\right] + \mathbf{L_o'}\left[\left(\mathbf{1}-\frac{\mathbf{Q'}}{\mathbf{d}}\right)^4 - \tau_o^4\right] \qquad [3\text{-}2]$$

Where:

d = dimensionless constant from gas temperature difference equation,

L_R' = loss coefficient for heat loss through refractory walls,

L_o' = loss coefficient for radiative flux through furnace,

τ_o = ambient to flame temperature ratio.

Full details of the derivation of equations [3.1] and [3.2] can be found in Appendix B.

3.3.1 Application of the 0-D Zone Model

A well-stirred furnace heat transfer computer program was developed by Jenkins (1999) to quickly evaluate the dimensionless furnace efficiency for a cement process. The original program, using a Microsoft Excel spreadsheet, was developed to simulate a flash-calciner, but can also be easily adopted for any well-stirred kiln design. Jenkins (2002) version of the 0-D model evaluates the energy source to sink ratio as a function of heat transfer between a pulverised coal flame and a 40% pre-calcined clinker within a rotary kiln. The present research seeks to evaluate a 100% limestone process without any pre-calcination, so the Jenkins model was revised. Additionally, a rotary kiln is not being considered as a viable option for the conceptual design of the proposed solar lime furnace, but is used here for reference purposes.

For ease of use, the original excel spreadsheets were transformed into a 'MatLab' code. The use of MatLab software allowed the physical dimensions of the furnace to be altered and the consequences evaluated while still keeping computational times relatively short.

The original 0-D Hottel zone model was developed for analysis of combustion driven furnaces, but because this type of modelling technique is dimensionless (black box), it does not differentiate between the types of energy input. For ease of investigation, the solar energy input for this 0-D Zonal Model will be approximated as an energy release of 43,830 kW which is the same as would be released by a pulverised coal flame.

Oates (1998) and Boynton (1980) report that the diameter of a typical rotary kiln ranges between 1.2m to 6.5m and have lengths between 25m to 230m. The MatLab code was used to vary the internal characteristic equivalent diameter (D_{eq}) of a proposed solar furnace from 1m to 9m, and the kiln length (L) from 20m to 250m. These ranges provide a comprehensive analysis of kiln efficiency as a function of the dimensionless furnace length (L/D_{eq}). The kiln efficiency in this case is defined as the useful energy out divided by the total input energy. The length (L) is the total furnace length and the characteristic equivalent diameter (D_{eq}) is the diameter of a circle with an equivalent cross sectional area as the furnace being analysed.

The internal surface area coverage of the limestone bed is also varied over the range 10% to 40% which provides an additional variable for the analysis. This percentage range encapsulates the fully range of bed surface areas that can be found historically in commercial rotary lime kilns.

Any kiln must allow the limestone feed material to enter, and the product to leave. For a rotary kiln, the feed entry is typically through the upper end of the cylinder, and the product is discharged from the lower end. The fuel and air enter through the lower end to provide a counter flow heat exchange which preheats the in feed. For each material, entry and exit openings must be provided. Within this mathematical model the size of these openings has been approximated to be equal to 20% of the cross sectional area of the kiln and are located equally at each end of the kiln. Because the area of these openings are a function of the furnace cross sectional area (rather than set to a specific dimension), energy loss through the openings of a short, large diameter furnace are substantial.

3.3.2 Assumptions used in the 0-D Zonal Model

Major assumptions used in the 0-D Hottel model include:

- The solar energy input is constant at 43.8 MW and is the same for all kilns under investigation.
- A grey gas assumption for the furnace atmosphere. The primary air temperature is 305K and secondary air temperature of 973K. The exhaust gases consist of air and evolved CO_2.
- A specked wall assumption. The sink (limestone) and furnace walls are intimately mixed. The sink and walls have constant thermodynamic properties.
- All limestone particles within the kiln are exposed to the same amount of heat energy. The location of the limestone particle within the limestone bed is neglected.
- Emissivity of limestone is 0.7 and does not change with temperature.
- Exhaust gases leave the furnace at a uniform temperature.
- Convective heat transfer between the furnace atmospheric gases and the limestone sink are negligible.
- Heat losses from the furnace structure are due to conduction through the walls, then convection from the external shell surface. Wall thickness is 0.15m.

- There is one opening at each end of the kiln, which allows the feed to enter and product to exit. Each opening area represents 20% of the cross sectional area of the kiln.
- Radiative heat loss only through furnace openings. Remainder of furnace is enclosed.
- The internal wall temperature is the same as the furnace atmospheric gases. The outside wall temperature is the same as the ambient air temperature.
- Ambient air is at a constant temperature of 288K (15°C).

It also should be highlighted that, due to the opening area being a function of the furnace cross sectional area, a short, large diameter furnace, could possibly represent losses being greater than the input energy and therefore the thermal efficiency could become zero or negative. Recalling that the thermal efficiency is useful energy used within the furnace divided by the total input energy.

Additionally, it should be noted that the furnace shape is partially account for by calculating the total surface area of the furnace. This does not specifically identify the radiation exchange shape factors between surfaces within the furnace. However the shape factors are explicitly calculated and used within the multi-zone two dimensional zonal models presented in Chapter 9.

The kiln efficiency is defined as the useful energy out divided by the total input energy. The useful energy out is the amount of energy available for the bed of limestone.

The specifications for the initial conditions for all of the 0-D Hottel zone models are shown in Appendix C.

3.3.3 Effect of Changing Kiln Length

The zero dimensional Hottel MatLab code is used to evaluate the affects of varying the internal diameter (D) of a circular cross sectional kiln from 0.25m to 7m, and varying the kiln length (L) from 5m to 100m. Figure 3-8 displays the parameters L and D. The equivalent diameter (D_{eq}) is used if the kiln is not circular in shape and represents the diameter of a circle with an equivalent cross sectional area as the kiln being analysed.

For each 'change of kiln length' modelling run, the length of the kiln is varied between 5m and 100m, while the internal diameter of the kiln is held constant. The kiln diameter is then varied between each modelling run. Additionally, the '*degree-of-fill*' that the limestone occupies within the kiln was varied between 2.5% to 20%. Mullinger (2007) discussed that typically the degree-of-fill for "normal" rotary kilns within industry is between 10% to 15%, although there are few examples of kilns where 'dams' are used to increase residence times which have fill factors up to 30%.

NOTE:
This figure is included on page 89 of the print copy of the thesis held in the University of Adelaide Library.

Figure 3-8: A representation of a rotary kiln showing the total length and characteristic diameter dimensions.

Source: Linguistic Demographer (2006)

A conversion between 'degree-of-fill' to surface area was calculated using Equation [3.3], which equates the percentage of cross sectional area (X) that is occupied by the limestone with the percentage of wall surface area (S) that is covered by the limestone, for a constant internal kiln radius.

$$X \pi r^2 = S 2\pi r \qquad [3.3]$$

Figure 3-9, shows the change in kiln thermal efficiency for variation in 'degree-of-fill' for a cylindrical shaped lime kiln with an internal diameter of 4m.

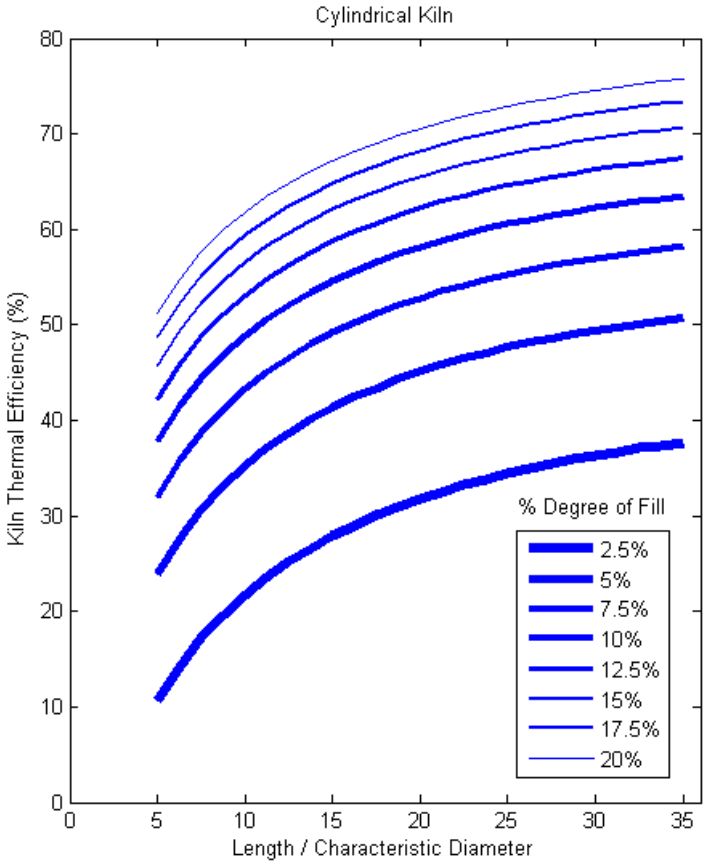

Figure 3-9: Predicted thermal efficiency of a 4m diameter rotary kiln, for increasing kiln length and percentage of limestone fill within the kiln.

Figure 3-9 reveals an increase in thermal efficiency, for increasing kiln length for each increase in degree of fill. The low efficiency at short kiln lengths is caused by a relatively greater heat loss through the furnace openings. As the kiln length increases the thermal efficiency also increases for all degrees of fill. The reduction in slope with increasing L/D is due to heat losses from the kiln structure as its surface area increases with increasing kiln length.

The next aspect seen in Figure 3-9 is a logarithmic relationship between thermal efficiency and degree of fill. Intuitively, the thermal efficiency increases with increasing bed surface area coverage, because more limestone is exposed to the heat energy. The efficiency increases, as the effective heat transfer area of the bed becomes larger. This may indicate that higher efficiencies could be achieved by increasing the percentage of surface area available to the limestone bed.

Similar trends were observed for other characteristic kiln diameters.

The next step is to evaluate the effects of changing cross-sectional shape of the kiln.

3.3.4 Effect of Changing Kiln Shape

A comparison between different internally shaped kilns is undertaken by varying kiln shape while maintaining a constant cross sectional area. Figure 3-10 shows potential kiln cross sectional shapes with the same cross sectional area. Using the 4m diameter cylindrical kiln for reference the cross-sectional area is 12.57m^2. Using this cross sectional area an equivalent:

- square sectioned kiln has sides with 3.55m in length,
- equilateral triangular cross sectional kiln has sides of 5.39m in length,
- right angled triangle which has 45° angles and equal length horizontal (floor) and vertical wall dimensions of 5.01m has the hypotenuse (roof) being 7.09m, and
- an elliptical shaped kiln which has a semi-minor axis dimension of 1.41m and major axis dimension of 2.82m, which equates to an eccentricity (ε) of 0.866.

The eccentricity can be varied to produce other elliptical shaped kilns with equivalent area. Because these kilns all have the same cross sectional area of 12.57m^2 their characteristic equivalent diameter (D_{eq}) of 4m is the same.

Maintaining the cross sectional area ensures that the losses through the openings will be the same for each kiln. However the unused surface area of each different shape, and thus the heat loss through the kiln structure will differ.

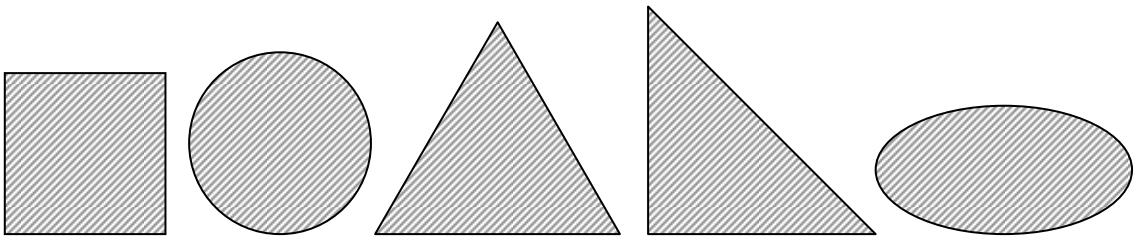

Figure 3-10: Kiln cross sectional shapes with the same cross sectional area.

Physical limitations within different cross sectional area kilns were discussed in Section 2.5.4. It is anticipated that the transport of limestone through non round kilns will be performed by a flat grate which moves longitudinally through the furnace. Grates in non-circular kilns are limited to be placed on the 'floor' of the kiln. The realistic percentage of bed area coverage of the total internal area is therefore 33% for the equilateral triangle, 30% for the right angle triangle, 25% for the square and approximately 20% for the elliptical kilns. For the modelling analysis the limestone bed area coverage over the floor of these kilns has

been set to 95%, which allows for clearance of the travelling grate system. The longitudinal length for each kiln is varied between 5m and 100m, while the characteristic diameter remains constant at 4m. The results from the thermal efficiency modelling for the various shaped kilns shown in Figure 3-10 are presented in Figure 3-11.

Figure 3-11 shows that for all kiln shapes the efficiency increases as the length of the kiln is increased. The plot also indicates, through the reduction in slope with increase in length on characteristic diameter ratio (L/D_{eq}), that the heat losses through the walls of the kiln play a significant role as the length of the kiln structure increases. The kiln with the highest thermal efficiency for any given length ratio is the equilateral triangle.

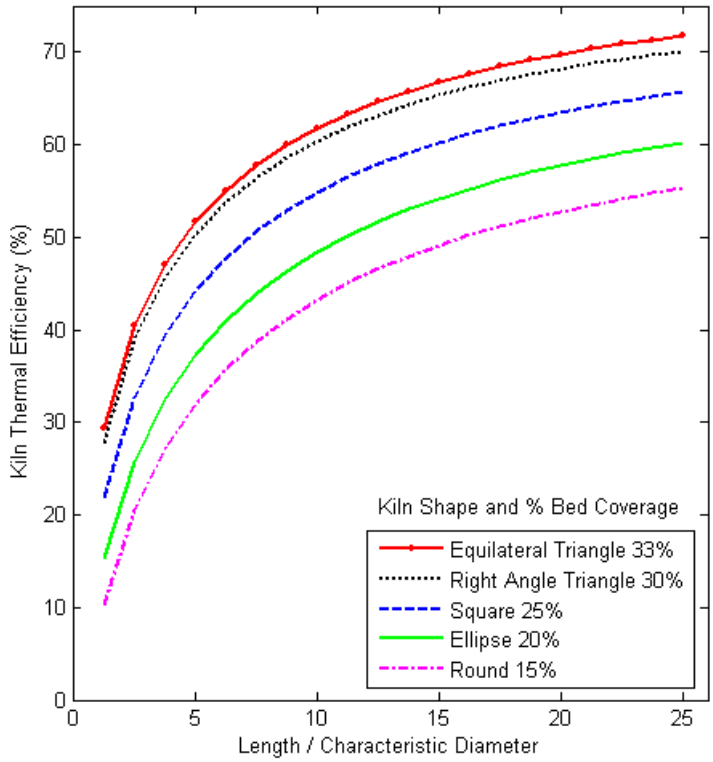

Figure 3-11: Comparison of round, square, triangular and elliptical cross-section kilns, with 95% of base bed area coverage.

The length to diameter ratio, $L/D_{eq} = 20$ is chosen as a reference for direct comparison of the efficiencies of the kiln shapes. At this L/D_{eq} the equilateral triangle has an efficiency of approximately 70%. The efficiency of the right angled triangular shaped kiln is approximately 68%, which is 2.5% less than the equilateral triangle. The square cross sectioned kiln then follows with an efficiency of approximately 64%, which is 7% less than the equilateral triangle. Followed by this is the ellipsoidal shaped kiln with an efficiency of approximately 58%, then the round (rotary) kiln with an efficiency of approximately 53%. These are 17% and 27% less efficient than the equilateral triangle respectively. The difference in efficiency

follows the percentage of bed coverage. The difference in efficiency between these kilns is primarily a function of available limestone bed area coverage.

To directly compare the furnace shapes a limestone bed area coverage of 25% has been chosen. The modelling results are displayed in Figure 3-12. The bed area coverage is calculated using the circumference of each shape and then multiplying it with the length of the kiln. The circumference varies for each of the different shapes. A constant 25% bed area coverage can therefore cover a larger surface area for one shape than for another.

Figure 3-12 shows the differences in efficiencies between the kiln shapes. For this case, both of the triangular cross-section kilns have higher thermal efficiency than the square, round and elliptical shapes. At a length on characteristic diameter ratio (L/D_{eq}) of 20 the difference in efficiency between all kiln shapes is only 3.5%, with the highest being the Right Angled Triangular shaped kiln at 65.4% and the lowest efficiency being the Ellipse at 61.9%.

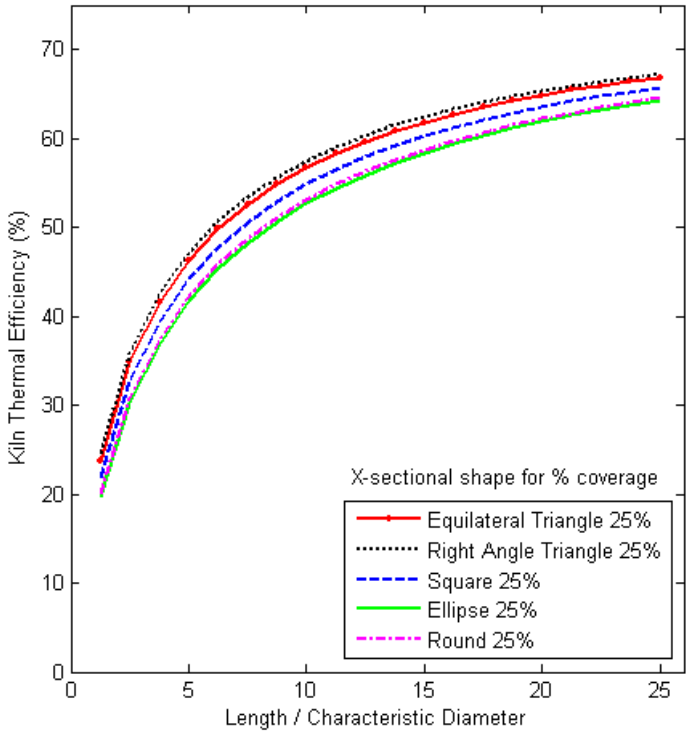

Figure 3-12: Comparison of round, square, triangular and elliptical cross-section kilns, with 25% bed area coverage.

The right angle triangle cross sectional kiln has approximately 0.955 square metres more limestone bed area coverage for the 25% surface area coverage than the equilateral triangle for the same cross sectional area. This extra surface area coverage provides for the extra kiln thermal efficiency. This also indicates that the heat losses from the kiln structure are less than the benefit of having the extra limestone bed area coverage.

The 25% bed area coverage analysis shows the possibility to increase the thermal efficiency for a kiln with a right angled triangular cross section. An evaluation is conducted to determine the effects of varying the roof angle θ from 45° while still maintaining the same cross sectional area.

Changing the roof angle θ alters the height of the vertical wall and floor / bed area as can be seen from Figure 3-13. This analysis assesses θ between 15° and 75° which provide an available floor cross sectional distance of between 9.69m and 2.60m respectively. Again the longitudinal kiln length is varied between 5m and 100m and in the analysis, the limestone bed area coverage over the floor of the kiln is set to 95%.

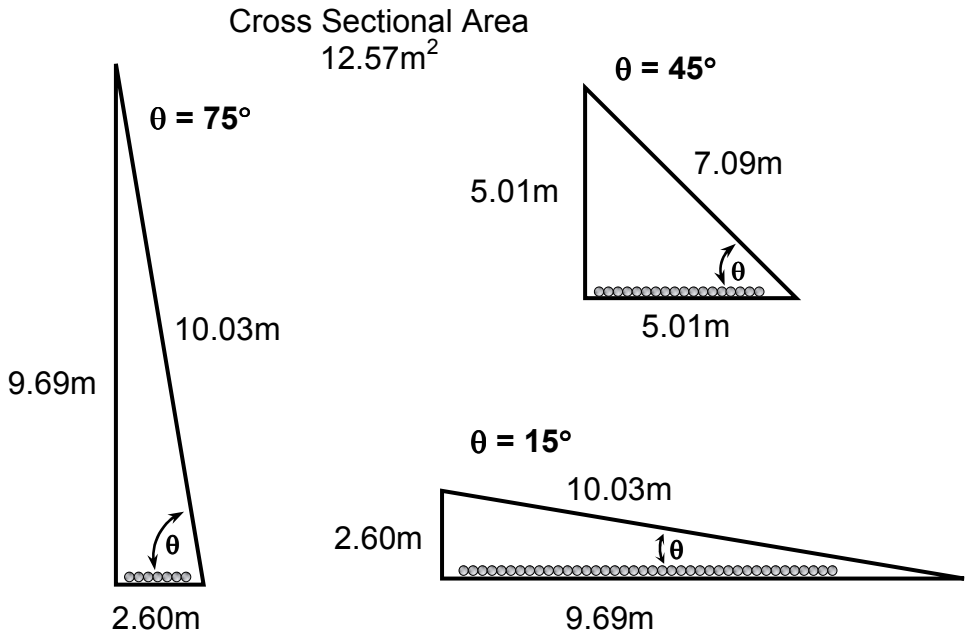

Figure 3-13: Cross sectional diagrams of furnace shape for right angle triangle with varying θ between 15° and 75°.

Figure 3-14 shows the change in thermal efficiency for varying the roof angle. For a constant kiln cross sectional area, the decrease in roof angle provides an increase in available floor area which increases the useful heat transfer to the limestone and thus increases the thermal efficiency.

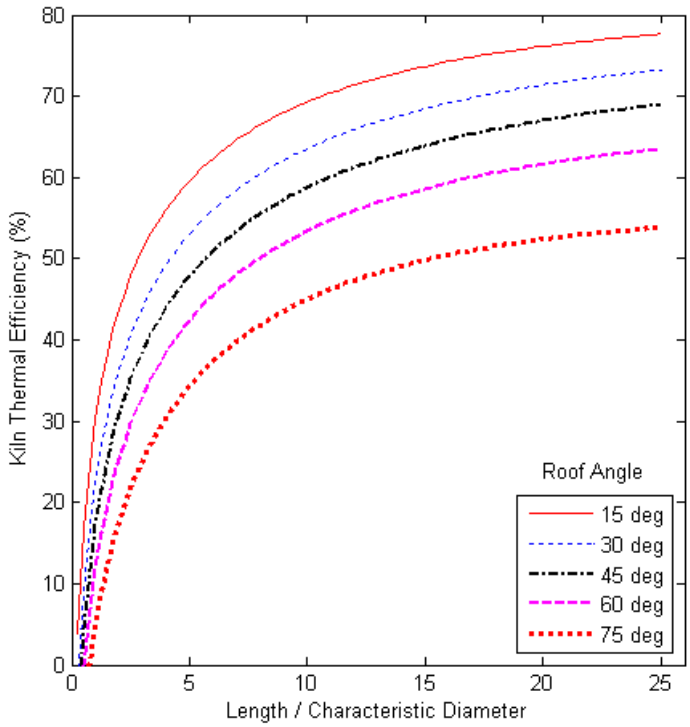

Figure 3-14: Thermal efficiency of a right angled triangle cross-section kiln with increasing length and change of roof angle from 15° to 75°.

The results from the change in kiln shape analysis using the zero dimensional Hottel zonal model show that there is an optimum kiln shape to maximise thermal transfer of heat to the bed of limestone by minimising heat loss through the kiln structure. Furthermore, an increase in thermal efficiency can be achieved by increasing the available limestone bed surface area. This could be accomplished by changing the cross sectional shape of a kiln. It appears that varying the aspect ratio of the kiln can provide increased thermal efficiency. Further analysis of this effect will therefore be undertaken.

3.3.5 Effect of Varying Aspect Ratio

The 0-D zone model is used to analyse the effects of changing aspect ratio on the thermal efficiency. The cross sectional shape of the kiln was altered by changing its width and height dimension. This has the effect of varying the surface area of the roof, floor and wall area, as can be seen in Figure 3-15. Rectangular shapes were chosen for this assessment with a square cross section as the reference. The reference square has a cross sectional area of 12.56m^2, which gives an equivalent diameter (D_{eq}) of 4m. A constant cross sectional area is maintained between all kiln shapes and therefore the openings area (inlet and outlet) also remain the same size.

To provide a comprehensive investigation the changes in kiln width are multiples of the original width dimensions, i.e. 2 × 3.54m, 4 × 3.54m, 10 × 3.54m, and 20 × 3.54m. The two later cases, 10 × width and 20 × width, are used for demonstration purposes only because of the impracticalities of suppling an even energy spread over the limestone bed with such low roofs.

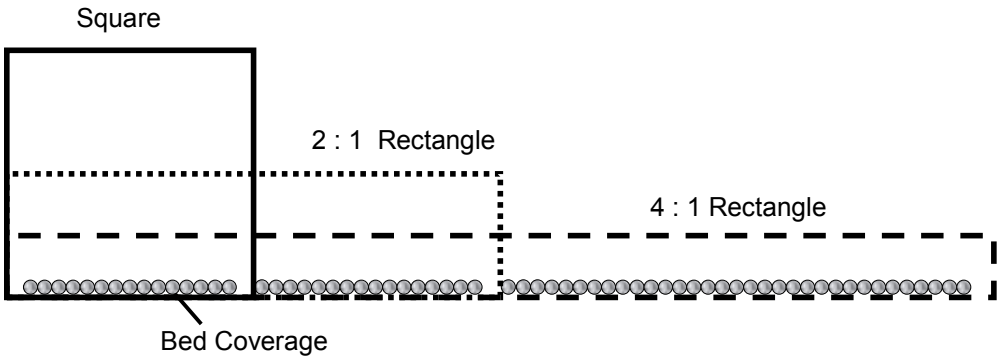

Figure 3-15: Cross-sectional view of a square kiln showing the change in cross sectional shape as the kiln width is increased but the cross-sectional area remains constant.

The limestone bed surface area is again set to 95% of the floor area. An increase in kiln width or length increases the limestone bed surface area. The 95% floor surface area coverage has been chosen to account for the area taken up by a grate system, which may be employed to transport the bed of limestone through the kiln.

Figure 3-16 shows that a 30% increase in the kiln thermal efficiency occurs by changing the kilns width from 3.54m (a square cross section) to 7.09m (the 2× width case). Additionally a 16.5% increase in thermal efficiency is achieved by increasing the kiln width from 7.09m (2× w) to 14.18m (4× w). The 10× width case shows a 13% improvement over the 4× case, but then the percentage of improvement decreases substantially to 3% between the 10× for the 20× width case.

Figure 3-16 indicates that a maximum efficiency of 82.7% at a kiln length of 58m for the 10× width case and 82.9% at 30m for the 20× width case. The decrease in thermal efficiency after the maximums is because of heat losses from the kiln structure. A plot of heat loss from the kiln structure for all the kilns considered can be seen in Figure 3-17. The plots indicate a relatively linear relationship between the structural heat loss and kiln length. The plot lines also show a substantial increase in structural heat loss for the larger width kilns. A point of interest in Figure 3-17 is the higher structural heat loss from the square kiln than the 2× width case. This is because the limestone bed surface area is larger for the 2x width case than the square case, while the refractory area is approximately the same between the two, which is shown in Figure 3-18. The larger limestone bed surface area utilises more of the

available heat energy and therefore less energy available to be lost through the kiln structure.

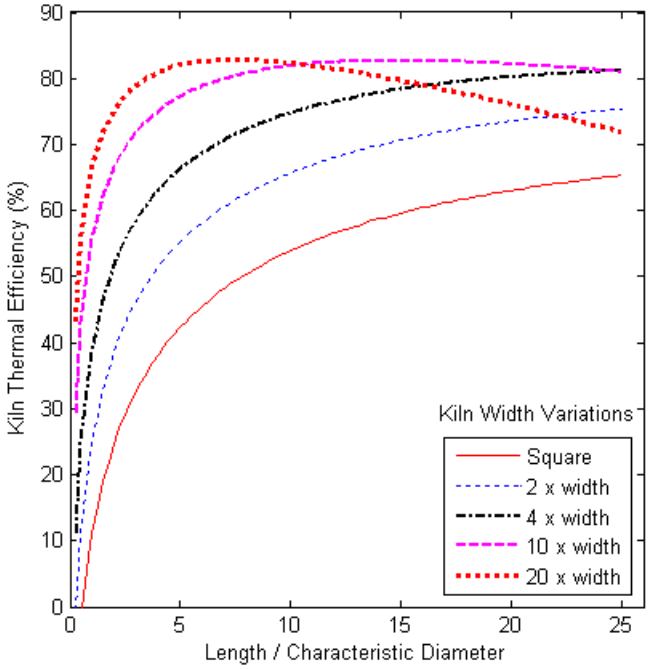

Figure 3-16: Effects of changing the kiln width on thermal efficiency while maintaining a constant cross sectional area, but increasing kiln length.

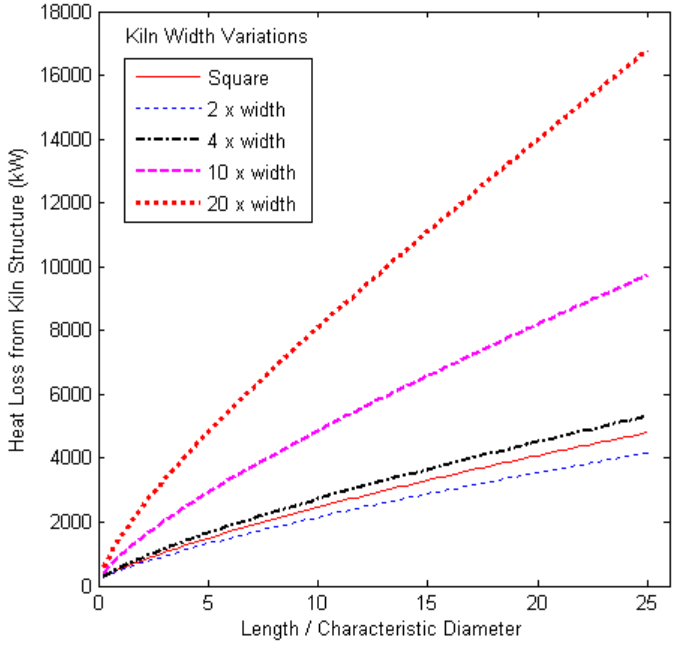

Figure 3-17: Plot of heat loss from the kiln structure for kiln length for variations in kiln width.

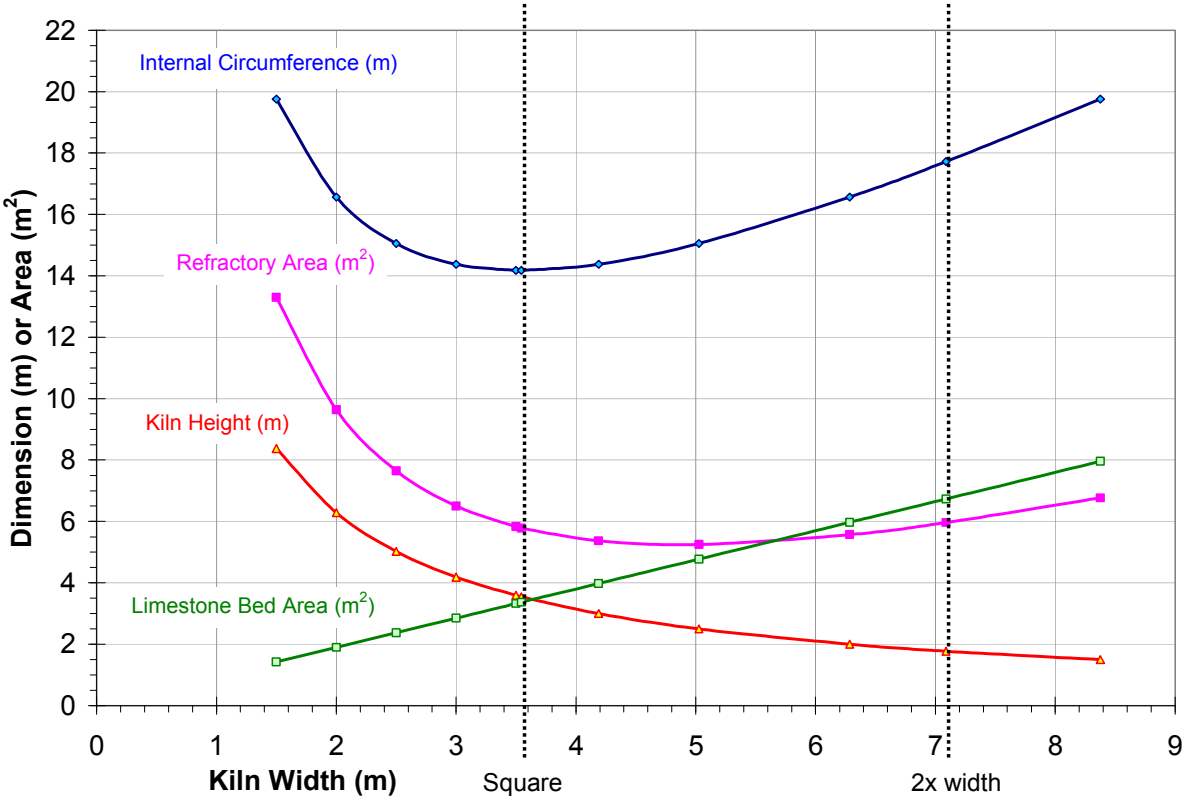

Figure 3-18: Characteristic dimensions and surface areas for changes in kiln width. The differences between the square cross sectional kiln and 2x width kiln cases are indicated.

The 0-D zone model has been used to analyse the effects of changing the aspect ratio of a square cross-section kiln while maintaining a constant cross sectional area. This analysis shows that it is possible to optimise the aspect ratio of a kiln by examining the relationship between the limestone bed surface area and the unused refractory internal surface area. A balance between the kilns width and height is required to ensure that heat losses are minimised and thus an improvement in thermal efficiency can be achieved.

3.3.6 Effect of Varying Kiln Opening Size

The aim of this analysis is to assess heat losses through openings in the walls of the kiln structure. Openings are required to allow exhaust gases to escape, the process material to enter and exit and allow for the concentrated solar radiation to reach the limestone. The effects of altering the size of the openings were assessed by changing the openings area and maintaining constant kiln dimensions.

A rectangular cross sectional kiln of internal dimensions 3m high, 6m wide and 75m long, was chosen as the base-line reference within the MatLab 0-D zone model. This kiln has a

cross sectional area of 18m^2, a D_{eq} = 4.78m and an L/D_{eq} = 15.67. The openings area for this reference configuration was set to or 7.2m^2. This represents approximately 0.5% of the total kiln surface area of 1386m^2. This open area represents 20% of the two 6m wide x 3m high 'end' walls, as discussed in section 3.3.2. The energy input for this 0-D Zonal Model is the same as for the previous sections, which is 43.8 MW.

The thermal efficiency of this reference case is first calculated. This thermal efficiency value then provides a comparison base so that as opening areas are varied the change in thermal increase or decrease can be quantified. The effects of varying the opening size can then be assessed. Figure 3-19 shows the variation in efficiency due to variation in limestone bed coverage for this reference kiln. It can be seen that a minimum 2% limestone coverage is required to provide a positive energy transfer. It can also be seen that the 95% limestone bed surface area coverage used in the previous sections, gives a thermal efficiency of approximately 68.6%.

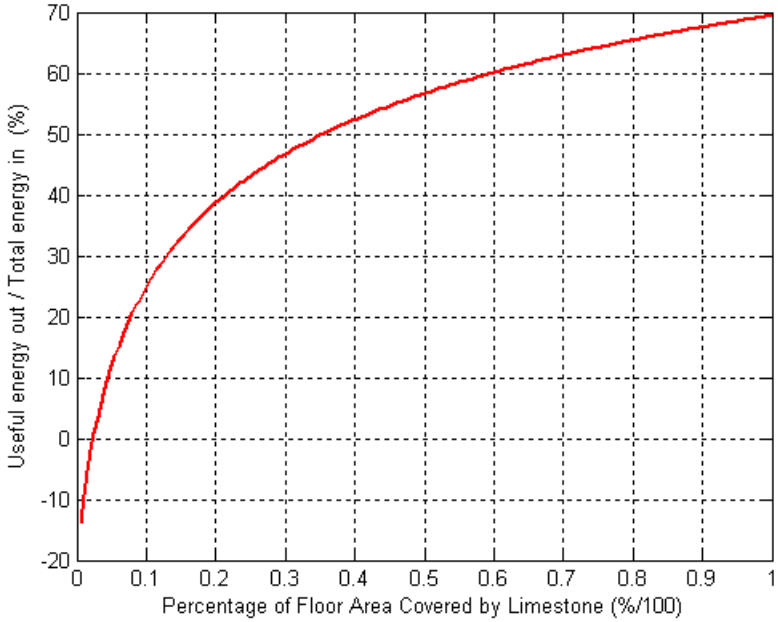

Figure 3-19: Variation in thermal efficiency as the floor area coverage is increased.

Figure 3-20 shows the reduction in thermal efficiency e.g. heat loss through the kiln openings, as the openings area is increased. The figure shows a linear relationship between the heat loss and the opening area. It also shows that at 19% open area (or 293m^2) the thermal efficiency is zero. This indicates that there is no useful energy reaching the limestone bed.

Similar linear relationships were calculated for larger sized rectangular cross sectional kilns 6m (H) x 12m (W) x 100m (L), the difference being a larger open area (600m^2), but a lower

percentage of total kiln area (16%) at which zero efficiency is obtained. For smaller sized rectangular kilns 1.5m (H) x 3m (W) x 50m (L), smaller open areas (94m^2), but higher percentage of total open area (20.5%) were calculated for zero efficiency.

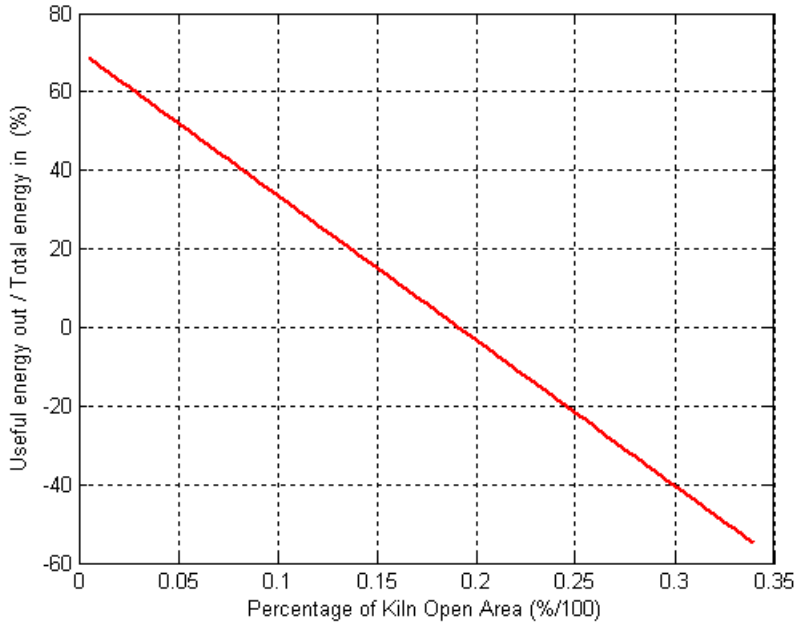

Figure 3-20: Variation in thermal efficiency as the area of openings is increased with all other kiln parameters remaining constant.

3.3.7 Effect of Varying Kiln Structural Dimensions

This analysis will assess the heat losses through the kiln structure. To evaluate the effect of structural dimensional change on the thermal efficiency, the height (H), width (W) and length (L) of the kiln are systematically varied. These dimensional changes will cause the area of the limestone bed to increase and decrease in proportion to the length and width changes. The openings area and energy input was maintained constant.

A base-line reference rectangular kiln is again used which has internal dimensions of 3m high, 6m wide and 75m long. This kiln has a D_{eq} = 4.78m and an L/D_{eq} = 15.67 and for a thermal efficiency of approximately 68.6% for the 95% limestone bed surface area coverage.

The H, W and L dimension are varied from 0.5m to 'twice the specified base-line dimension'. That is H is varied from 0.5m to 6m, while the W and L constant at 6m and 75m respectively. W is varied between 0.5m and 12m while maintaining constant H and L. The L is then systematically varied.

The first aspect to note from Figure 3-21 is that by increasing the height dimension the thermal efficiency decreases. This is because increasing the height increases the wall surface area and thus an increase in structural heat loss from the kiln. Increasing the length or width dimension, increases the thermal efficiency of the kiln. This is because of the increase in available limestone bed surface area. The gradient of the change in width dimension curve is 3.5 times higher than the gradient of the length dimension curve. This difference comes from the 95% of limestone bed coverage, ie 5% bed loss, which is maintained for length variations but is proportionally reduced for width variations.

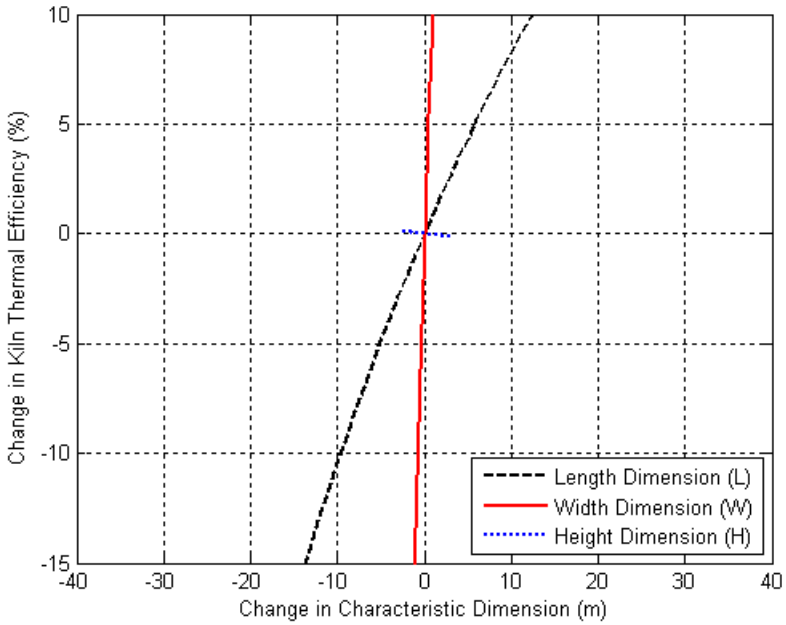

Figure 3-21: Variation in kiln thermal efficiency as the characteristic dimensions of the kiln are altered for constant opening area.

3.3.8 Comparison of Structural and Openings Heat Losses

A comparison is made between the heat loss from the kiln structure and heat loss from kiln openings area. To determine which heat loss has more effect, a plot of structural heat loss and radiant heat loss through the openings, for changes in wall height from 0m to 6m were calculated. The openings area represented 20% of the wall area and therefore increased as the wall height increased. The remaining kiln dimensions 6m (w) x 75m (L) and energy input parameters were the same used in Sections 3.3.3 to 3.3.6 above and remained constant during the calculations.

Figure 3-22 shows the calculated heat losses. The structural heat losses are consistently 48% more than the openings heat loss, but the surface area of the structure is more than 100 times larger than the area of the openings. The heat flux losses from the openings on

average is 33 kW/m^2 compared to 0.98 kW/m^2 for the structural loss. Figure 3-22 therefore indicates that the kiln height should be kept as low as possible. While this has some value, physical constraints on providing heat transfer to the entire process material may limit this.

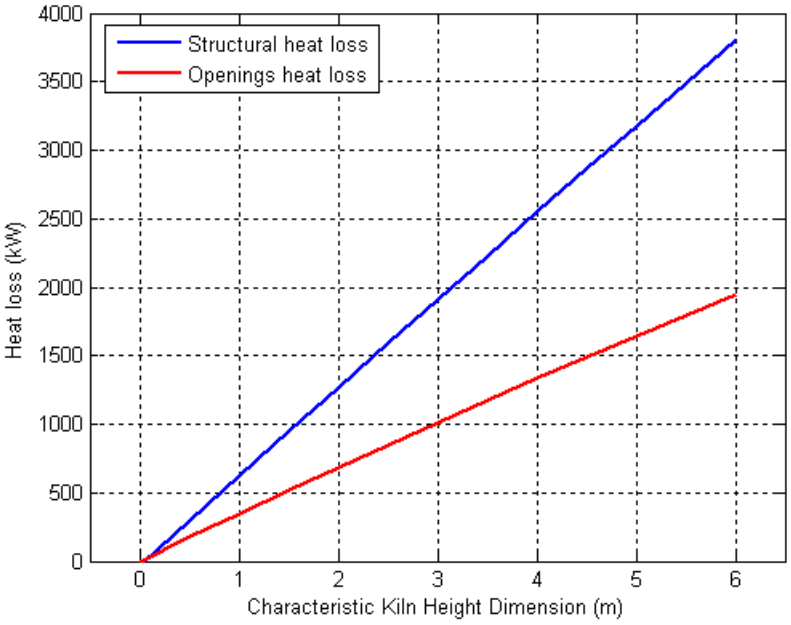

Figure 3-20: Distribution of heat loss from a 3m high, 6m wide and is 75m long kiln when changing the kilns height up to 6m.

It is clearly very important to reduce the impact of the opening losses by reducing the size of the opening(s). While this has some value, physical constraints on providing heat transfer to the entire surface of the process material may limit this. The openings should therefore be kept as small as practically possible.

3.3.9 Conclusions from the 0-D Zone Modelling

The analysis using the zero-dimensional Hottel zonal model has shown that the thermal efficiency of a limestone manufacturing kiln can be optimised through the methodical variation of kiln dimensions and observing its effects. This modelling has shown that it is possible to optimise thermal efficiency of a kiln using several methods including:

1. maximising the percentage of kiln surface area covered by the limestone bed to maximise heat transfer,

2. the careful choice of the internal cross sectional shape of the kiln,

3. minimising heat loss through the kiln structure by minimising ‘unused’ kiln surface,

4. minimising the area of any openings through the kiln enclosure to reduce heat losses.

For a kiln with a cross-sectional area of 12.57m^2 and an equivalent diameter of 4m, the cross sectional shape with the highest calculated efficiency of 70% was the equilateral triangle. This configuration maximises the percentage of surface area covered by the bed.

Comparing potential kiln shapes with the same limestone bed surface area of 25%, and for a L/D_{eq} = 20, the right angled triangular cross sectional kiln provided the highest calculated efficiency by around 3.5%. To minimise heat loss from the kilns vertical wall the lowest realistic vertex angle should be used. Solar kilns with triangular cross sections have not previously been assessed within literature.

The 0-D zone model has also shown that a width to height ratio of approximately 2 should be used if a rectangular cross sectional shaped kiln with a cross sectional area of 12.57m^2. This provided a 30% increase in thermal efficiency over the square cross sectioned kiln. Maximising the available limestone bed surface area can be achieved by either increasing kiln length or increasing the kiln width. Lower structural heat losses are achieved by increasing the kiln width and thus a higher thermal efficiency was calculated. Again minimising the height of the vertical walls helps reduce structural heat losses and thus improve thermal efficiency.

The area of entrance and exit openings, which allow the process materials to flow through the kiln and the exhaust gases to escape the kiln, should be minimised. For a 43.8MW solar energy input the heat flux losses from the openings on average is 33 kW/m^2 compared to 0.98 kW/m^2 for the structural loss. Minimising the openings area improves kiln thermal efficiency.

This modelling technique has provided general design parameters which can be used to maximise kiln thermal efficiency. While the absolute accuracy of the zero-dimensional model is inferior to more complex methods owing to the numerous simplifying assumptions, it has provided some powerful insights into trends and preferred configurations. A more comprehensive higher order zone model is therefore used within Chapter 9 for a more accurate calculation.

Chapter 4

Experimental Apparatus and Techniques

4.1 Introduction

This chapter describes the equipment and procedures used for the experimental aspects of this research investigation. The experiments are used to evaluate the effects of using radiation as the sole heating source for the calcination of Penrice Angaston marble. This is achieved by quantifying the relationships between radiation intensity, stone size and calcination rate for small to medium sized Penrice Angaston Marble.

An electric muffle furnace is used for the calcination experiments first, to quantify the relationships between calcination temperature, particle size and sample size (bed thickness). These relationships are also used as a comparison base for the solar radiation experiments. The muffle furnace provides a repeatable and temperature controllable environment.

Concentrated solar simulator experiments are then used to investigate the effect of radiation intensity on the calcination kinetics of the limestone as a function of stone size. The intensity of the radiation which illuminates the marble is varied as is the size of the marble stone. The results from these experiments are used for validation of the calcination mathematical model used within the solar furnace model.

This chapter begins by briefly describing the method used to calibrate the numerous thermocouples used for temperature measurements. Following this the procedures used to prepare and sort the marble samples are described along with a compositional analysis of the material. The equipment and experimental procedures used within the muffle furnace calcination experiments are then presented. The five-kilowatt xenon arc lamp used to simulate the solar radiation is described, followed by the design of the calcination platform and methods used within the open solar calcination experiments. The chapter concludes with the design and experimental methods used within the experimental solar furnace.

4.2 Temperature Measurement

Type K (chromel–alumel) thermocouples were used for all temperature measurements. Three styles of K-type thermocouple were used; surface contact, bare wire and stainless steel protection sheathed.

Calibration of each thermocouple was conducted before and after each usage. The calibration consisted of measuring and recording the temperature of both iced distilled water and then boiling distilled water. The recorded data was used to calculate measurement errors and adjust the data collection apparatus to provide the 100°C of the boiling water. Due to time and economic constraints the calibration of the thermocouples was conducted at a significantly lower temperature than expected for the actual measurements. While it is recognised that this procedure is not ideal, higher temperature calibration tools were not readily available.

The ice water calibration involved locating the thermocouples centrally within an isothermal (foam) container which was filled with clean crushed ice and distilled water. The thermocouples were positioned to ensure that they did not contact the bottom or sides of the container, which could affect the temperature measurement. The mixture was then thoroughly mixed for 3 minutes to ensure a homogeneous solution and to allow the thermocouples to stabilise before the temperature measurements taken. The temperature measurements were displayed on a Digitech QM-1600 digital multimeter and recorded manually.

The boiling point calibration involved locating the thermocouples centrally within an electric kettle. Again the thermocouples were positioned to ensure they did not contact the bottom or sides of the kettle, especially the heating element! The distilled water was boiled for 3 minutes before the measurements were taken, again using the Digitech QM-1600 digital multimeter.

Table 4-1 shows the measurements for the twelve K-type thermocouples when exposed to the iced and boiling water for both before and after their use within the experiments. The maximum measurement error for each thermocouple has also been calculated and is displayed.

Table 4-1: Measured thermocouple temperature for iced and boiling water for both before and after (in parenthesise) use within the experiments.

Thermocouple Identification	Iced Water Temperature	Boiling Water Temperature	Maximum Measurement Error
A	0.3°C (0.3°C)	100.4°C (100.3°C)	0.4%
B	- 0.1°C (- 0.1°C)	99.8°C (99.9°C)	0.2%
C	- 0.2°C (- 0.3°C)	99.4°C (99.8°C)	0.6%
D	0.0°C (0.2°C)	100.1°C (100.0°C)	0.1%
E	0.1°C (0.0°C)	100.3°C (100.2°C)	0.3%
F	- 0.1°C (- 0.2°C)	99.8°C (100.0°C)	0.2%
G	0.0°C (0.1°C)	100.1°C (100.1°C)	0.2%
H	0.1°C (0.1°C)	99.9°C (99.7°C)	0.3%
I	0.0°C (-0.1°C)	100.0°C (99.8°C)	0.2%
J	0.2°C (0.2°C)	100.2°C (100.2°C)	0.0%
K	- 0.1°C (- 0.1°C)	99.8°C (99.9°C)	0.2%
L	0.1°C (0.3°C)	99.8°C (100.2°C)	0.3%

4.3 Sample Collection and Preparation

The limestone used within these experiments comes from Penrice Soda Holding Limited's open cut quarry located 77 km north-east of Adelaide City at Angaston, South Australia. The limestone deposit is a fine to medium grained marble that originated from an early Cambrian marine transgression dominated by carbonate sedimentation (Graetz, 2000). This limestone was subsequently metamorphosed (i.e. temperature and pressure) to marble and subjected to intense folding and faulting.

The quarry at Penrice, Angaston utilises a crushing and screening plant and numerous stock piles of the sized and sorted marble-limestone. The extraction rate from the quarry face is approximately 1.2 million tonnes of marble per year. Penrice's soda ash manufacturing plant uses 47% of the marble within its Solvay process. Adelaide Brighton Cement use approximately 24% of the marble for the manufacture of lime and cements, while 10% is sold for use in the manufacture of plate glass, metallurgical fluxes, plasters, tiles, whitening and fillers. The remaining 19% is sold as gravels and rubbles for road construction and other civil engineering uses.

The Angaston crushing and screening plant uses an Allis Chalmers gyratory crusher for primary crushing. It operates at an aperture set to 450mm and was rated to a maximum 1,200 tonnes per hour. The primary crushed stone was first scalped (screened) to remove impurities (overburden) and sorted into initial stockpiles. All +120mm sized stone were then directed to a Jaques gyratory secondary crusher for further size reduction and again scalped. Six shaker screens were used to sort the limestone into numerous sizes required by Penrice and their customers. Table 4-2 shows the current screen sizes at the crushing and screening plant. Using these, Table 4-3 shows the sizes of marble currently available from the Angaston quarry.

Table 4-2: Screen Sizes at Penrice quarry, Angaston.

		Primary Screen	Secondary Screen	Upper Gravels Screen	Lower Gravels Screen	LOP Screen	Auxiliary Screen
Screen Deck	Top	120mm	120mm	32mm	20mm	55mm	15mm
	Middle	60mm	-	20mm	10mm	-	1st Middle 4mm 2nd Middle 2.5mm
	Lower	25mm	45mm	12.5mm	3mm	-	1mm

Table 4-3: Marble size ranges stockpiled at the Penrice quarry, Angaston.

A	-120mm to +60mm	**H**	-32mm to +20mm
B	-120mm to +45mm	**I**	-20mm to +12.5mm
C	-60mm to +45mm	**J**	-20mm to +10mm
D	-60mm to +25mm	**K**	-15mm to 4mm
E	-45mm to +32mm	**L**	-10mm to +3mm
F	-45mm to +20mm	**M**	-4mm to +2.5mm
G	-45mm to +15mm	**N**	-2.5mm to +1mm

Samples of between 5 kg to 10 kg of each of the sizes shown in Table 4-3 were taken from the Angaston quarry on the 19th of July, 2004. The simple grab sample method as outlined within the Australian Standard, AS 1199-2003 was used. Briefly, this involves scooping a quantity of rock for collection from the same location within a stockpile. The selection of location for taking the sample within the stockpile and the size of the sample should not be predetermined. Additionally the sample should not be sorted to select stones with desirable attributes.

The samples were placed within sealable plastic containers and labelled with the collection location, time and date. The samples were then stored in a dry location within the laboratory until prepared for use.

4.3.1 Composition of Penrice Marble

Penrice, Angaston marble is considered industrial grade, being typically 96% to 98% calcium carbonate ($CaCO_3$). An oxide analysis was conducted on two 200 gram samples of the Penrice marble using an X-Ray Fluorescence fused bead technique, which complies with AS 4489.5.1-1997. The chemical composition testing was performed within Adelaide Brighton Cement, Birkenhead Division Laboratory on the 20th of June 2005. The Penrice marble is compared with limestone samples collected from Mataranka, Northern Territory and Klein Point, York Peninsula South Australia.

Table 4-4: Component weight % dry basis, of some South Australian limestone.

Compound	Penrice Marble July 2004	Mataranka Limestone November 2004	Klein Point Limestone May 2005
CaO	54.4	53.7	45.4
MgO	0.6	0.3	1.0
$CaCO_3$	97.14	95.89	81.07
$MgCO_3$	1.5	0.75	2.5
SiO_2	1.6	1.7	11.4
Al_2O_3	0.3	0.5	1.8
Fe_2O_3	0.1	0.5	1.2
TiO_2	0.01	0.03	0.10
K_2O	0.05	0.012	0.35
Na_2O	0.04	0.02	0.10
SO_3	0.02	N/A	0.04
P_2O_5	0.02	0.35	0.02
SrO	0.03	0.01	0.03

N/A - analysis Not Available

4.3.2 Sample Preparation

Each grab sample was spread over a plastic sheet on the ground so that the stones could be visually inspected. Stones with significantly different size ratio (length to width) were removed from the sample. Boynton (1980, pg 178), and Oates (1998, pg 127), both suggest that a size ratio of approximately 2 to 1 is desirable to lime makers because it promotes a uniform calcination time and therefore encourages high product consistency and quality.

Less than a dozen stones from each grab sample were found to be out of size ratio. These stones were collected and further crushed within a *Fritsch Pulverisette 1* reciprocating jaw crusher operating with an aperture of 4mm. The crushed rock was collected from the bottom of the crusher and visually inspected. Any stone with a size ratio larger than 2:1 was reprocessed through the jaw crusher. The samples were then collected and placed back into dry, sealed plastic containers waiting further sorting. The dust residue which remained on the sheets was also collected and sealed within a labelled plastic container.

4.3.3 Sieving

The grab samples with stones smaller than 10mm (samples L, M & N in Table 4-3) were further sorted into more distinct size ranges using a collection of Endocotts sieves which are shown in the first column of Table 4-5. The sieves use stainless steel wire cloth apertures which comply with BS410-1986.

The second column of Table 4-5 shows the nominal diameter of each stone size range. The sieves were selected to provide marble which are a multiple of the 0.375mm nominal diameter stones. The third column of Table 4-5 shows these diameter ratios, while the forth column shows the calculated nominal mass of the average nominal diameter stone. These stone sizes have been specifically chosen to provide a good representation of the marble used within many flash calciners (and some rotary kilns) as well as other local industrial processes such as glass and metal refining. It also represents the size of particles desirable for slaking moderate to low reactivity quicklime without forming excessive grit, Oates (1998, pg 231).

Table 4-5: Selected sieve sizes and resulting nominal diameter of marble particle.

Sieve Aperture Size µm	**Marble Nominal Diameter (*ND*) mm**	**Diameter Ratio** $\frac{ND_i}{ND_1}$	**Nominal Mass mg**
250 µm	0.375	1	0.075
500 µm			
850 µm	0.925	2.5	1.13
1.00 mm			
1.70 mm	1.850	5	9.02
2.00 mm			
2.36 mm	2.855	7.5	33.2
3.35 mm			

The sieving method utilised was based on the methods as set out by AS 3638 – 1993 Australian Standard for Test Sieving Procedures.

The marble was first divided into 500 g lots. Each marble lot was then placed into the largest sized aperture sieve located at the top of the sieve stack that contained 5 sieves and a collection bowl. A tight fitting lid was placed on top and the stack fitted to an Endocotts, ELF2 Mk3 430 Watt electric shaker. The shaker was operated for a minimum of 5 minutes, after which the sieve stack was removed and samples checked for size consistency. The samples were each transferred to sealable plastic containers, which were labelled with the name of the material, the date of collection, the date of sieving, and the size range. The sieves were then thoroughly cleaned and the sieve stack reassembled ready for the next 500 gram marble charge.

Marble that did not fit through the 3.35mm sieve was further pulverised using a *Fritsch Pulverisette 1* reciprocating jaw crusher operating with a 2mm aperture, and re-sieved into the size ranges shown in Table 4-5.

4.3.4 Mass Sizing

Grab samples with marble particles between 20mm and 4mm (samples I, J & K in Table 4-3) were manually sorted into mass size ranges using a process of selection, weighing and grinding. Mass sizing was used to provide stones of similar size range to that used within rotary and Calcimatic kilns (Table 2-1).

The manual selection process involved visually identifying desirable stones of a spherical - cuboid shape. Each stone was then weighed using the GX-600 analytical balance and excess material removed by grinding, until the desired mass was achieved. Table 4-6 shows the selected stone masses, the mass tolerance and the calculated nominal characteristic diameter of each marble particle.

Table 4-6: Mass sizes of marble and nominal characteristic diameter.

Mass of marble g	Tolerance g	Nominal Characteristic Diameter mm
0.333	0.005	6.54
1.000	0.005	9.44
2.000	0.005	11.90
3.000	0.005	13.62
5.000	0.005	16.15

A mass ratio of approximately 3 was chosen between each stone size to provide a good distribution within the calcination measurements.

4.3.5 Drying

The sized and sorted samples were first sun dried in open topped containers prior to use. This involved spreading the samples onto flat plastic trays and setting them on a north facing window sill, with the window closed. In the late afternoon the trays were collected and stone placed within air tight containers until morning when they were laid out again. After 3 days of sun drying, the samples were collected and sealed within small air tight plastic containers and stored in a dry dark location. It should be noted that the Australian Bureau of Meteorology cite the average maximum temperature within Adelaide in October to be 21.8°C with 8.3 hrs of sunshine providing a mean daily solar exposure of 5.64 kWh/m^2.

Immediately prior to each experimental regime, the marble samples were weighed using the GX-600 analytical balance then placed into individual open topped containers, which were in turn placed within a Watson Victor drying cabinet set at a temperature of 130°C. This was considered essential to remove any remnant moisture that would affect mass loss measurements during calcination, especially in the smaller sized samples.

The samples were dried until no further weight loss was recorded. The minimum time that a particular sample stayed within the dryer was 60 minutes, with the longest sample being dried for approximately 14 days. Each sample was reweighed and the loss of moisture calculated before being used for the calcination experiments. Figure 4-1 shows the measured mass change due to moisture loss during dying for four nominal diameter marble samples. The maximum measured mass loss was 0.1 g, with the average being 0.04 g.

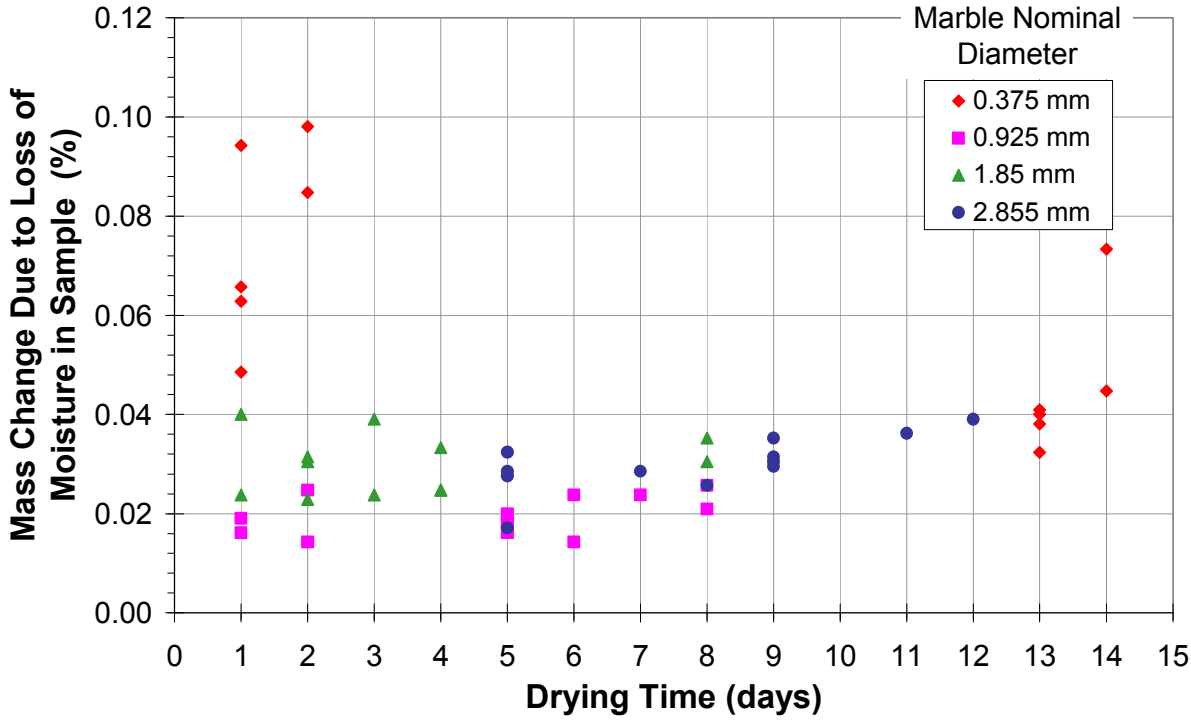

Figure 4-1: Mass loss from marble samples dried for varying lengths of time.

4.4 Muffle Furnace Experimental Apparatus

The muffle furnace experiments involved calcining samples of the different characteristic diameter Penrice marble at furnace temperatures of either 900°C or 1000°C. The samples were placed either within a crucible bowl or on top of a refractory brick and then positioned within the preheated furnace. This section describes the procedures used for the muffle furnace calcination experiments. Further experimental procedures used within the muffle furnace experiments are outlined in Chapter 6.

4.4.1 Electric Muffle Furnace

An Electric Carbolite Furnace, Type HTF1 ELP was used for the muffle furnace calcination experiments. With the front door of the furnace closed, the internal dimensions of the enclosure were approximately 110mm wide, 110mm high and 100mm deep. A photo of the muffle furnace is shown in Figure 4.2 a). The furnace had an integrated electronic control system that allowed the operator to set a furnace temperature with an accuracy of one degree Celsius. The digital display on the controller provided the set point temperature and the current furnace temperature. To verify the temperature within the furnace, the calibrated thermocouple identified as “D” in Table 4-1 was inserted into three small access ports

located along each side of the electric muffle furnace as shown in Figure 4-2 b). Each furnace 'set-point' temperature was maintained for 30 minutes, after which the thermocouple was inserted into the furnace. The first temperature measurement location (A) was at the upper centre at the rear of the furnace, the second measurement (B) taken at the geometric centre of the furnace, and the third location (C) on the lower centre near the front door of the furnace.

a). b).

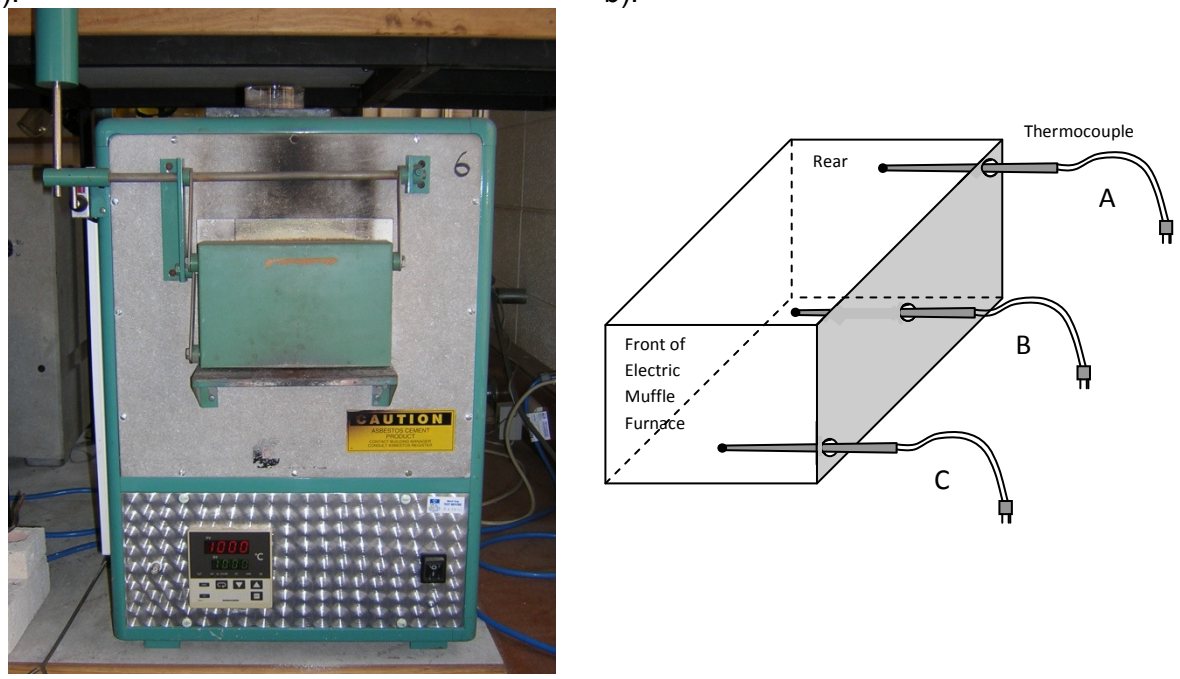

Figure 4-2: a). Photo of the electric Carbolite muffle furnace used for the muffle furnace experiments. b). schematic showing location of the temperature measurement points within the muffle furnace.

The 'D' thermocouple temperature was displayed on a Digitron - Model 3900 and manually recorded. The recorded furnace temperatures and percentage differences are displayed in Table 4-7.

The calcination experiments were conducted in the middle of the furnace making it desirable to record the temperature of the furnace at this location. The furnace was adjusted and calibrated against the thermocouple temperature measurements at Location B. This provided a tolerance of less than ±1% in furnace temperature between the front and rear of the furnace.

Table 4-7: Furnace temperatures measured using thermocouple D.

Furnace Display Temperature Set Point	Thermocouple Temperature Location A	Thermocouple Temperature Location B	Thermocouple Temperature Location C	Maximum Temperature Difference as Percentage %
800°C	804°C	802°C	799°C	+ 0.50
900°C	909°C	904°C	898°C	+ 1.00
950°C	960°C	955°C	947°C	+ 1.04
1000°C	1009°C	1005°C	995°C	+ 0.89

4.4.2 Crucible Bowl

A 150ml translucent silica “Vitreosil” broad based, squat form crucible bowl was used to contain the Penrice marble. The crucible was 82mm in diameter and 51mm in height. The lid of the crucible bowl was not used. The crucible was thoroughly cleaned between each experiment to ensure no remnant material remained. The mass of the empty crucible was also measured before and after each calcination experiment as a verification of cleanliness.

The crucible was placed onto a small fire brick when inserted into the preheated furnace. The fire brick was used firstly to position the bowl in the middle of the furnace, and also to protect the floor of the furnace from further abrasion.

The total mass of the crucible and contents were measured immediately after removal from the furnace. The crucible was then placed within a desiccator to cool to approximately 50°C. The desiccator was used to maintain a moisture free environment during cooling of the lime product. During the cooling process, lime can absorb significant amounts of moisture, which could affect subsequent reactivity or loss on ignition test.

4.4.3 Flat Bed Ceramic Fibre Refractory Board

Further muffle furnace experiments were conducted by spreading various sizes of Penrice marble over the top surface of a ceramic fibre refractory board, which was then placed within the muffle furnace for various periods of time. The fibre refractory board was a commercially available FiberFrax Ceramic Fiber Duraboard. This type of board was selected because it exhibits Lambertian reflectance and so radiation falling on it is scattered such that the apparent brightness of the surface is the same regardless of the angle of view. This

becomes useful for the solar radiation heat flux measurements and is discussed further in Chapter 5.

The refractory board was cut to dimensions of 10mm thick, 100mm wide and 100mm long so that it could fit within the furnace. The fibre board has a density of 270 – 300 kg/m^3 and a maximum thermal conductivity of 0.309W/m.K. It also retains thermal and physical stability for temperatures up to 1260°C.

The refractory board was thoroughly cleaned between each experiment to ensure no remnant material remained and the mass of the board was measured before and after each calcination experiment as a verification of cleanliness.

The total mass of the refractory board and sample were measured immediately after removal from the furnace. The refractory board was then placed within a desiccator to cool until the surface temperature was 50°C. Again the desiccator was used to maintain a moisture free environment during the cooling of the lime product.

4.4.4 Analytical Balance

An A&D, model GX-600 analytical balance was used to measure the mass of the crucible, refractory board and Penrice marble samples before, during and after the experiments. The balance has a weighing capacity of 610 grams and resolution of 0.001 grams.

Calibration of the balance was conducted each time the balance was operated using the internal calibration mass and the automatic self-calibration. Calibration testing using certified external masses was also conducted every 30 hours of balance operation.

The balance includes an automatic self check function, which adjusts the measurement response time and also displays a warning to conduct a calibration if there is a significant temperature variation. The self check also adjusts the response time if there are fluctuations in the measurements due to air drafts or vibration.

Real time, and automatic data collection and storage was available through manually programming the balance. The data was then transferred via an RS-232 serial interface port of the analytical balance, to a personal computer. A Microsoft Windows based communication tool called Win CT, was used to collect and save the data within comma separated values (csv) files. The data collection frequency for the balance was 10Hz and the data transferral was set to be averaged over 3 seconds.

4.5 Solar Simulation Experimental Apparatus

The choice to use a solar simulator for the supply of high intensity radiation followed an extensive review of existing solar research facilities. It was determined that the availability and unpredictability of solar energy could be restrictive for some experiments. Real time measurement of the available and supplied radiation needs to be conducted so that the effects of clouds, dust and pollution can be taken into account. Additionally the scale and length of experiments could also be restricted by the size of the collection heliostats. A solar simulator on the other hand can provide a consistent radiation source independent of the time of day or night. The measurement and monitoring of exactly how much power is being supplied can be easily facilitated. An assessment of the most significant advantages and disadvantages of using a solar simulator was made and it was decided that the fundamental experiments should be conducted using a solar simulator.

A radiation light source that mimics natural daylight was therefore required. The following high-intensity discharge (HID) light sources were identified:

- The high pressure short arc mercury lamp
- The metal halide lamp
- The exposed carbon rod arc lamp
- The xenon arc lamp
- The high pressure sodium lamp
- The mercury vapour lamp

These lamps are all considered to be "point" light sources which make them ideal for focusing, and therefore can potentially produce high energy fluxes. The Xenon short arc lamp was finally selected due to its availability and closeness in electromagnetic radiation spectrum to natural daylight. Unfortunately the Xenon short arc lamp does exhibit several strong Infrared spectrum components as described in Section 4.5.2, but these could be filtered if deemed necessary.

Standards relating to solar simulators are specific to either the testing of photovoltaic devices, for sun tanning devices in solariums, and for sunscreen testing. These standards include IEC 60904-9:2007, ASTM E927, ASTM E948, ASTM E1036, ASTM E1362, and JIS C 8912:1998. These standards relate to constant density insolations of roughly 1000 W/m^2, which is defined as the standard “1 Sun” value, with spectrum consistent to an air-mass (AM) global value of 1.5 (AM 1.5G), at an ambient temperature of 25°C. The most popular ‘standard recognised’ solar simulators use a Xenon arc lamp. To obtain the desired air-mass spectrum, correction filters are used to modify the xenon lamp spectral output to fall within

the IEC, JIS, and ASTM requirements for Class A solar simulators. Different filters can be used to simulate sunlight at different times of the day or in different geographic regions.

4.5.1 General Description of Apparatus

A photograph of the general arrangement of the solar simulator apparatus used for the solar calcination measurements is shown in Figure 4-3. A 5000-watt xenon short-arc bulb was used to provide the constant high intensity radiation source required for the experiments. The bulb was horizontally mounted at the foci of an elliptical (f2) reflector that was located within a Cinemeccanica projection lamphouse. The elliptical reflector creates a converging radiation beam that passes through a focal point 208mm $\pm$ 2mm from the front face of the lamphouse. A flat highly polished aluminium mirror was mounted at an angle of 45° to the radiation beam between the lamphouse exit opening and the focal point. The horizontal radiation beam was therefore directed vertically downwards to illuminate the marble from above. A heat resistant platform, onto which the marble was placed, was positioned below the mirror. The rate of calcination was directly measured and recorded using an analytical balance. An alumina tube was used to thermally isolate the analytical balance from the heated limestone and platform above. The analytical balance rested upon a scissor lifter, which was used to adjust the vertical distance of the platform from the aluminium mirror and thus control the intensity of radiation heat flux by changing the radiation path length. The mass measurement was transferred to a personal computer for storing, display and analysis. The experimental equipment was supported within a fully adjustable metal frame approximately 2.5m long, 1m wide and 1.2m high.

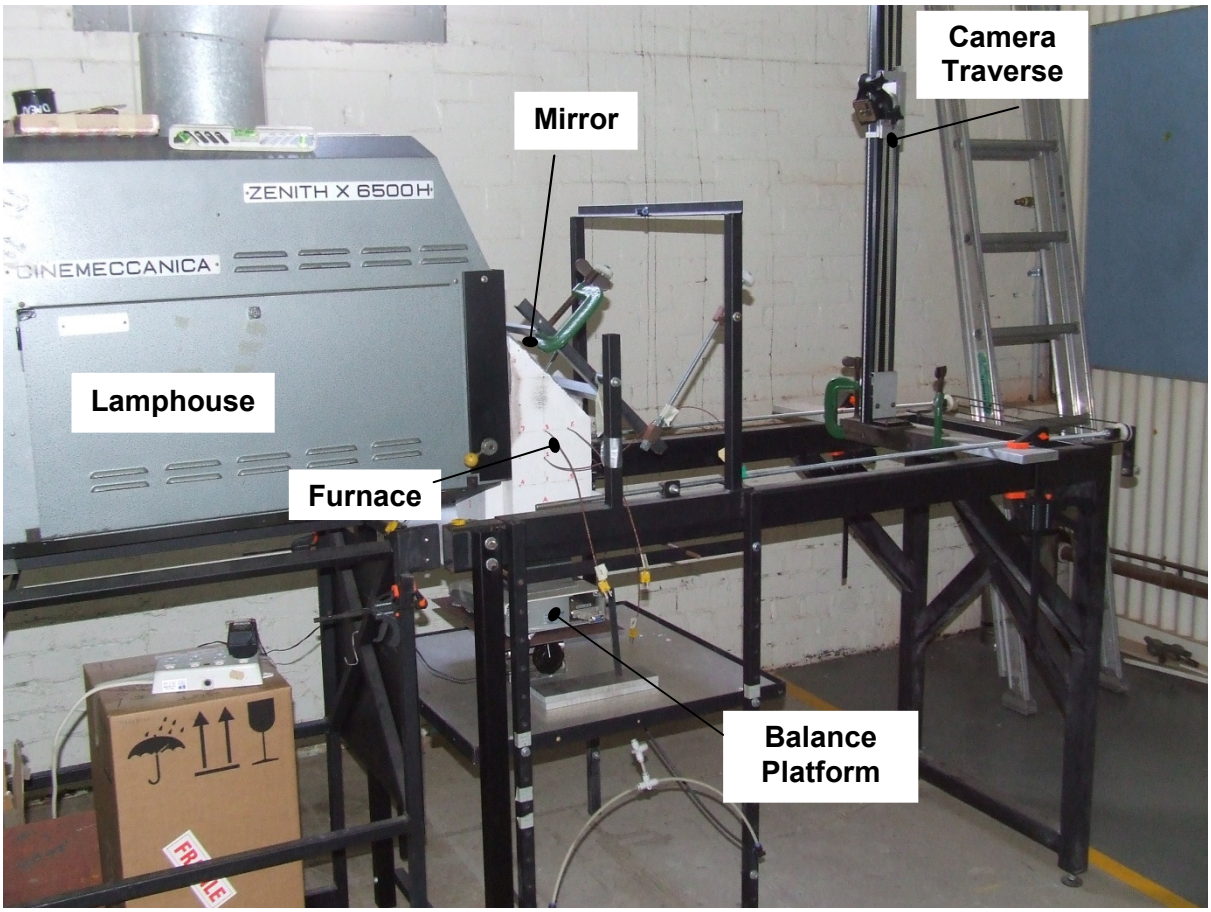

Figure 4-3: Photograph of the solar simulator apparatus showing the lamphouse, the solar furnace, the mirror mounting, the analytical balance platform and the camera traverse.

4.5.2 Xenon Short Arc Radiation Source

Over a hundred years ago, it was found that if the ends of two carbon rods were touched together and then connected to a powerful electrical source, some of the carbon would vaporize. If the rods were then moved apart a few millimetres, current would flow between the rods and a plasma "arc" would form. Thus the "Carbon Arc" light source was invented.

Carbon arc lamps were originally designed to use alternating-current (AC), but it was soon identified that using direct current (DC) produces a steadier and more satisfactory plasma arc operation. Values of 125-150 Amps at 20 – 35 Volts are used commonly for lamps within movie projectors and for theatre spotlights. During operation the supply voltage is maintained constant to ensure a constant plasma arc and thus radiant heat flux.

A carbon arc light source can produce an intense and brilliantly white light with an electromagnetic radiation spectrum similar to natural sun light given a suitable composition of the carbon rods and atmosphere through which the plasma discharge flows. In an open

atmosphere the plasma arc slowly consumes the tip of the carbon rod about 1.5mm per minute, and so continuous adjustment of the gap between the electrodes is required to ensure a consistent light source. A glass enclosure surrounding the arcing tips, which can be seen in Figure 4-4, was designed to slow the burning of the carbon and thus made the lamps last significantly longer. Current bulbs typically last for several thousand hours prior to needing replacement. Typically, these bulbs use a noble gas such as argon, neon, krypton and xenon or a mixture of these gases. Some lamps are also filled with additional materials, like mercury, sodium, and/or metal halides.

NOTE:
This figure is included on page 119 of the print copy of the thesis held in the University of Adelaide Library.

Figure 4-4: Photo of a HLR Osram 3kW Xenon short-arc lamp.

Source: Hyperlight (2007)

Xenon short arc lamps contain pressurised xenon gas at between 12 to 75 bar, through which high electrical current is passed, usually 100 to 150 Amps at a voltage of between 30V to 50V as described within OSRAM (1996). A Xenon bulb will provide a continuous electromagnetic spectrum from 240nm up to 3000nm. Figure 4-5 shows the comparison between a typical xenon short arc lamp and solar extraterrestrial irradiance and for air masses (AM)[7] of 1.5. Seen in Figure 4-5 are the pronounced peaks within the xenon spectrum between 850nm and 1000nm which are reported by Oriel Instruments (1998) to provide approximately twice as much infrared radiation in proportion to the ground level global solar irradiance.

7 The Air Mass (AM) describes the effect of absorption and diffusion by mainly CO_2 and H_2O within the atmosphere. AM 0 is the extraterrestrial spectral distribution. AM 1 is the incident radiation measured at sea level perpendicular to the earth's surface. AM 1.5 is the incident radiation on an inclined plane tilted 37° toward the equator, facing the sun.

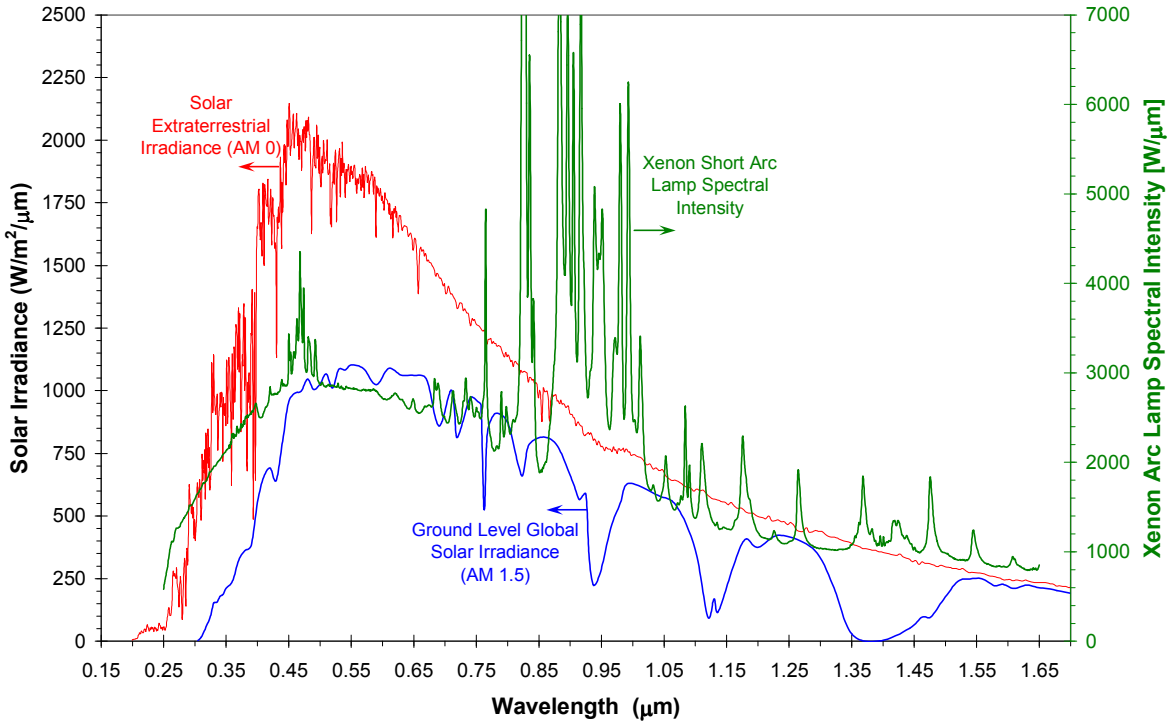

Figure 4-5: Spectral intensity of a Xenon arc lamp compared with extraterrestrial and ground level solar irradiance.

Source: American Society for Testing and Materials (2003), and Dimitriadis (2002)

Due to its availability, an Osram XBO 5000 W/HBM OFR Xenon short arc bulb was selected. OSRAM (1996) specify that approximately 80% of the electrical input is converted into radiation (60% radiated by the electric arc, 20% radiated by the electrodes), 20% is lost through conductive and convective heat loss for xenon short arc bulbs. The manufacturer also specifies an average luminance from the lamp as 95,000 cd/cm^2 (luminous area 2.2mm x 1.3mm) which is only marginal smaller than the luminance of a midday sun (100,000 to 150,000 cd/cm^2). Other specifications for the Xenon Lamp XBO 5000 W / HBM OFR can be seen in Table 4-8.

Table 4-8: Specifications for the Xenon XBO 5000W / HBM OFR lamp.

Rated Lamp Wattage	5,000 W
Rated Lamp Voltage	34 V
Rated Lamp Current	140 A
Luminous Flux	225,000 lm
Luminous Intensity	27,000 cd

4.5.3 Cinemeccanica - Milano Lamphouse

There was very little choice of locally available equipment to house the xenon bulb. An older style Italian made theatre projector lamphouse called a Cinemeccanica - Milano Zenith X6500H became available after an extensive search. The lamphouse can accept xenon arc lamps up to maximum of 6500 watts. The lamp was mounted horizontally within the lamphouse as seen in the orthographic drawing, Figure 4-6. The lamphouse facilitates three dimensional movement of the Xenon bulb within the elliptical (f2) reflector. The light emitted from the lamphouse can therefore be adjusted and focussed by adjusting the plasma arc around the foci of the reflector. The elliptical reflector has a diameter of 381mm (15 inches), a focal distance of 802mm and a divergence half angle of 12.85 degrees. The reflector was made from Pyrex glass which was front silver coated. The reflectivity of polished silver as documented in Nostell (2000), is approximately 0.97 over most wavelengths. This reflectivity value is used within the radiation modelling presented in Chapter 9.

NOTE:
This figure is included on page 121 of the print copy of the thesis held in the University of Adelaide Library.

Figure 4-6: Orthographic drawing of a Zenith X6500H lamphouse.

Source: Cinemeccanica – Milano (1990)

The cross sectional diameter of the focal point of the radiation beam produced by the elliptical reflector is approximately 12mm. The reflector was adjusted to move the focal point to a location 208mm ± 2mm from the front face of the lamphouse.

The diverging radiation beam leaves the Cinemeccanica lamphouse horizontally through a 110mm diameter opening on the front face of the lamphouse. Figure 4-7 shows the change in diameter of the illumination spot as the radiation beam converges to the focal point and then diverges again. The heat flux distribution becomes inverted both vertically and horizontally after it passes through the focal point.

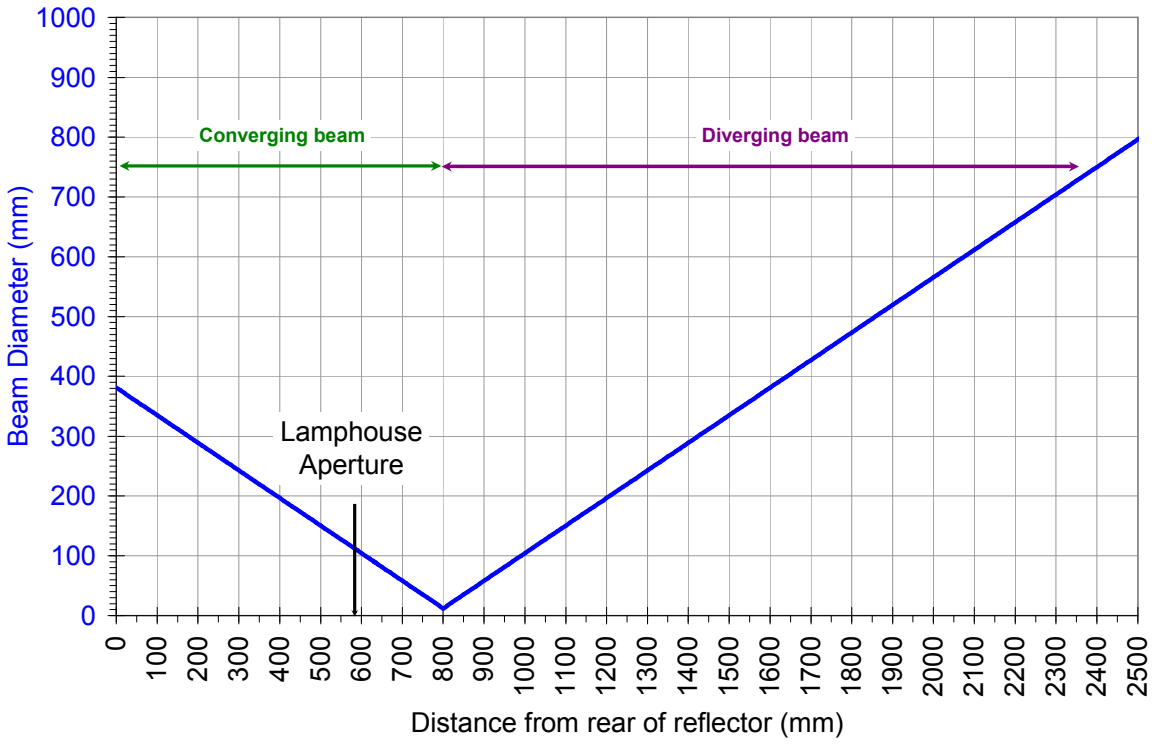

Figure 4-7: Calculated beam diameter as a function of distance from the rear of the lamphouse's reflector.

The input voltage and amperage were digitally displayed on the rear of the lamphouse. These power values could be recorded both manually and automatically through standard BNC connectors and a suitable data collection module. Due to the relatively steady operating conditions, the electrical input power was recorded manually.

An IREM N3 - X140DM / B rectifier power supply was used to supply the lamphouse with the required power for the xenon lamp. Three phase 415 volt AC power was supplied to the rectifier where it was converted into 30 - 39 volt and 70 – 140 amp DC power. The output power range was varied using an adjustable magnetic shunt, which allowed continuous output regulation over the entire operating range.

4.5.4 Total Heat Flux Transducers

The radiant heat flux from the xenon arc lamp radiation source was measured directly using two Medtherm 64-Series Schmidt- Boelter heat flux transducers. These total heat flux transducers directly measure radiant heat transfer rates. The transducers provide a linear output, in millivolts (mV), which is directly proportional to the net heat transfer rate absorbed by the sensor. The Schmidt- Boelter thermopile type sensors absorb energy at the sensor surface which causes it to heat. This surface then transfers the heat to an integral heat sink, which is held at a temperature below that of the sensor surface. The difference in temperature between the sensor and the sink is proportional to the heat being transferred and therefore proportional to the heat flux being absorbed. A thermocouple junction is positioned at both the sensor and the sink which form a differential thermoelectric circuit providing a self generated electromotive force (EMF). The scale of the EMF is directly proportional to the heat transfer rate.

The two 64P-1-24 model transducers (serial numbers 92241 and 92242) were water-cooled and air purged. Each transducer was supplied with a calibration certified between 0 to 11.35kW/m^2 (i.e. 0 to 1 BTU/ft^2.sec.). The calibration curves provide the relationship between the millivolt output and the measured heat flux. The transducers had an over-range capacity of up to 500% (i.e. up to 56 kW/m^2), with a maximum non-linearity within ±2% of the full range, with an accuracy of ±3%, and repeatability within ±0.5%. The viewing angle of the sensor window was approximately 150°, with a nominal absorptance of 92% over the 0.6 to 15.0 μm wavelength range. The sensor inlet was covered by a 0.5 mm thick sapphire glass window which eliminated convective heat transfer. The sapphire window had a nominal spectrum transmittance of 85%. The transducer's maximum allowable operating body temperature was approximately 204°C (400°F).

4.5.5 Beam Deflection Mirror

The horizontal beam from the Cinemeccanica lamphouse was impractical to use for direct heating because of the difficulty in supporting vertically arranged marble samples. To maximise the proportion of stone directly illuminated by the radiant energy it was desirable to illuminate the stone from above. The diverging high intensity beam therefore needed to be deflected (reflected) vertically downwards.

Only polished aluminium and silver exhibit high reflectance throughout the entire wavelength interval of the solar spectrum Nostell (2000). Of these two materials aluminium is considerably cheaper and is more frequently used for radiation reflection. Figure 4-8 shows the reflectance of radiation by stainless steel, aluminium and silver between the wavelengths of 0.3μm and 2.5μm. Stainless steel does not have a high reflectivity, but it is highly resistant to mechanical wear and chemical corrosion, whereas aluminium continually oxidises and silver tarnishes easily. The mirror was used within a laboratory environment and therefore it was decided that a highly polished aluminium mirror would be preferred for the present investigation. The mirror was mounted immediately in front of the lamphouse outlet and positioned at 45° from the horizontal.

The mirror was made from 5083 marine aluminium 200mm high x 140mm wide x 12mm thick. The aluminium was mechanically polished to a very high mirror finish and further enhanced using clay based gold and silver polish made by Autosol. No additional coating or anodizing was put on the surface of the aluminium. Additives in the clay polish are claimed by the manufacture to provide some protection against oxidation and tarnishing.

NOTE:
This figure is included on page 124 of the print copy of the thesis held in the University of Adelaide Library.

Figure 4-8: Reflectance of stainless steel, aluminium and silver between 0.3μm and 2.5μm.

Source: Nostell (2000)

Being a base metal, the aluminium reacts immediately with oxygen in the surrounding air and forms a thin, compact, tough, stable and inert (passive) film of natural oxide (alumina, Al_2O_3), which provides protection to the base aluminium from further corrosion and tarnishing. A layer of Al_2O_3 one nanometre thick is formed in 2 hrs and depending on the humidity within

the atmosphere, the thickness of the alumina film grows to between 4 and 10 nanometres, as explained within Bartl and Baranek (2004) and De la Fuente *et al*. (2007). The thin Al_2O_3 layers are optically transparent to most wavelengths, but this transparency reduces as the layer grows, as described by the Optical Coating Laboratory Inc (2003). Nostell (2000) explains that the anodising on the reflective surface reduces the reflectivity of the polished aluminium over time as seen in Figure 4-9.

NOTE:
This figure is included on page 125 of the print copy of the thesis held in the University of Adelaide Library.

Figure 4-9: Solar reflectance from an aluminium mirror as the surface anodises over time.

Source: Nostell (2000)

The reflectivity of the mirror was therefore monitored by measuring the steady state temperature of the aluminium. An increase in the temperature would indicate an increase in the absorptivity of the radiation beam and therefore a decrease in the reflectivity of the mirror. Many researchers, including Mills (1999), quote a black body emissivity coefficient, ε, for highly polished aluminium of between 0.037 and 0.069. An average value of 0.053 has been selected for the emissivity coefficient of the aluminium mirror. The reflectivity value of 0.947 is therefore used within this thesis.

It was calculated that an increase of approximately 1% in absorptivity would be indicated by a measured temperature increase of 20°C, from 483 K to 503 K. This calculation assumes that the emissivity of the aluminium is independent of temperature and of the spectral absorptivity of the mirror surface. The energy balance calculation was conducted over the entire aluminium mirror, and takes into consideration the incident radiation heat flux and the convective and radiative heat loss of the heated aluminium, but does neglect the thermal

conductivity through the 4 mounting bolts. The recorded temperature rise was found not to change appreciably throughout the experimental campaign.

4.5.6 Calcination Platform

The radiation beam was directed vertically downwards onto a platform on which the Penrice marble was placed. A pictorial representation of the general arrangement of the calcination platform used for the solar calcination measurements is shown in Figure 4-10. The platform was made from a sheet of FiberFrax Ceramic Fiber Duraboard, the same material as discussed in Section 4.4.3. The platform refractory board was cut to provide a platform with dimensions 10mm thick, 100mm wide and 100mm long. A small sheet of stainless steel was used to attach the platform to a tube of high purity alumina which provided thermal isolation of the analytical balance from the high temperatures associated with the radiant heat flux intensities expected. The alumina tube passes through a sheet of FiberFrax refractory board which provided additional heat shielding for the analytical balance. The GX-600 Analytical balance has a maximum operating temperature of 40°C, in addition to requiring the temperature to be relatively stable. The heat shielding was independently secured to the equipment frame 150 mm above the analytical balance. The analytical balance rested upon a scissor lifter which was used to adjust the height of the platform and thus control the intensity of radiation heat flux by changing the radiation path length.

The weighing capacity of the balance was approximately 610 g and the mass of the smallest Penrice marble particle was approximately 0.333 grams. To maintain the sensitivity of the GX-600 analytical balance, the mass of the calcination platform system was minimised. Each component of the system was weighed and any excess material removed. By far the heaviest component was the alumina tube. The diameter of the tube was considered on its stability, strength and mass. A thin walled, larger diameter tube was considered to be most beneficial. The length of the tube was calculated by performing heat transfer calculations so that the 40°C maximum operating temperature of the analytical balance was preserved. A length of 150mm was determined to be thermally adequate. The standard stainless steel weighing tray on the analytical balance was replaced with an equivalent sized lightweight aluminium tray to further minimise excess mass on the balance. The total mass of the calcination platform system was 258 grams.

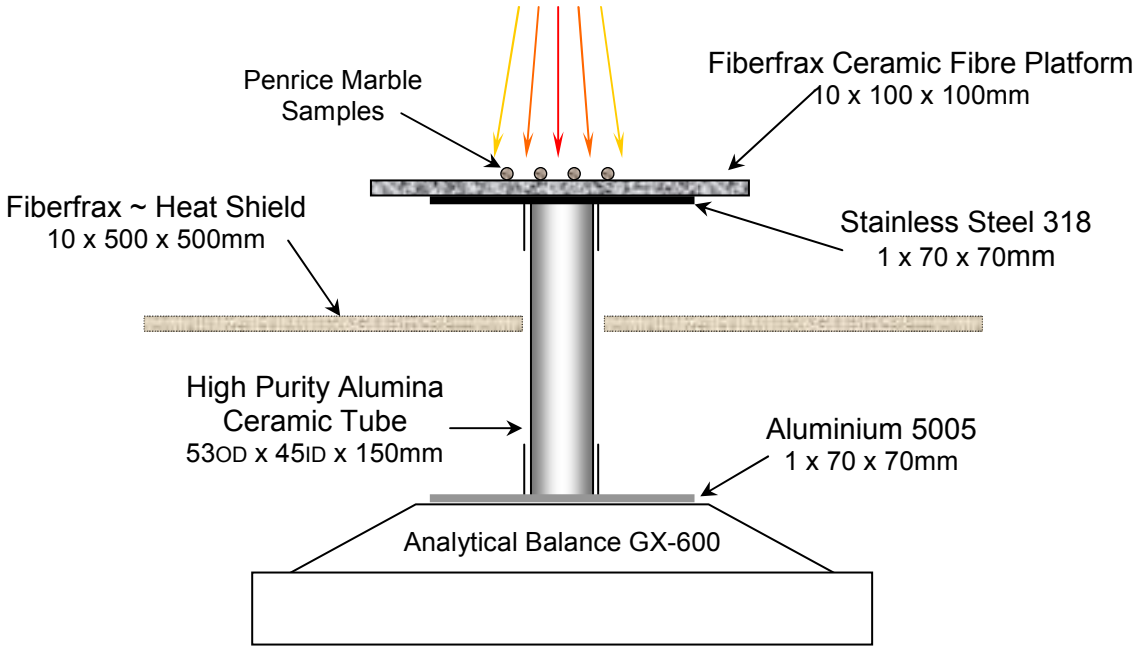

Figure 4-10: A pictorial view of the calcination platform showing the locations of the analytical balance, isolation tube, heat shield and calcination platform.

The temperature of the FiberFrax ceramic fibre platform was measured using the K-type surface thermocouple identified by the letter “L” in Table 4-1. The thermocouple was placed centrally on the rear surface of the platform, between the stainless steel and the platform. The thermocouple wire to the data collector was positioned such that it did not adversely affect the operation of the balance.

4.5.7 Equipment Frame

An isometric drawing of the general arrangement of the equipment frame used for the solar calcination measurements is shown in Figure 4-11. The frame was constructed from low carbon, mild steel. The frame could be adjusted or altered at any stage of an experiment through the use of interchangeable components and adjustable threads. The ‘mirror frame’ and ‘balance rest frame’ could be moved towards or away from the lamphouse as desired, while the mirror framework could be tilted to any desired angle. The pictorial insert shown in Figure 4-11 displays the mirror framework adjusted to 45° as was required for the radiation beam deflection. The analytical balance rest was vertically adjustable to provide coarse adjustment in calcination platform height.

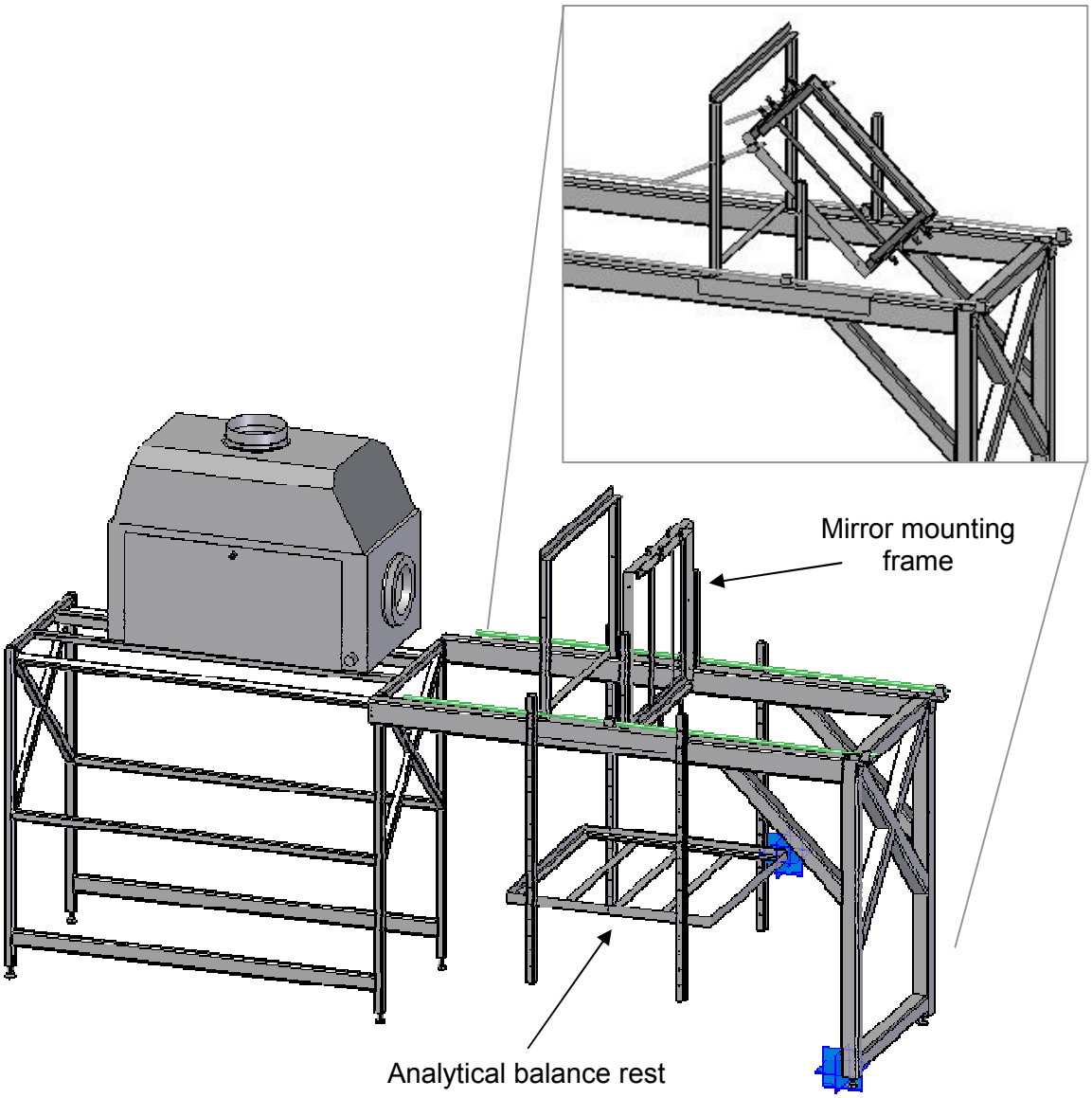

Figure 4-11: An isometric view of the equipment frame showing the lamphouse, mirror mounting and analytical balance rest.

4.5.8 Data Collection and Analysis

The A&D model GX-600 analytical balance was used to measure the change in mass of the Penrice marble during the calcination reaction. The analytical balance, data collection and logging techniques used for these calcination reaction measurements are the same as those described in Section 4.4.4. Real time data collection, logging and display of the weight change due to the release of the carbon dioxide from the marble sample were conducted.

The mass loss was quantified by dividing the measured mass loss by the theoretical mass loss required to achieve complete calcination, i.e. 55.2% of the original mass of the particle. This 55.2 % weight loss comprises 97.15% $CaCO_3$ and 1.5% $MgCO_3$ totalling 98.64% (from

Table 4-4) multiplied by the theoretical percentage of remaining product ~ 56%. This calculation provides the percentage of conversion from $CaCO_3$ to CaO over the reaction time. The rate of calcination was calculated from the rate of the mass loss over time using Microsoft Excel.

A visual inspection and photograph of each Penrice marble particle was taken before and after each experiment. The inspection identified any hard burning present on the surface of the particle or any unusual irregularities.

Cooling of each marble sample took place within a glass desiccator. Once cooled within the moisture-free environment, the sample was sealed within a sealable plastic container and stored within a dry and dark location awaiting the slaking test.

4.6 Solar Calcination Experiments

Solar calcination experiments were conducted in two experimental regimes. The first was an open system where single stones of Penrice marble were placed onto the top surface of a refractory board and directly exposed to the high intensity heat flux. The second regime made use of an enclosed furnace structure to surround the base refractory board, while still directly exposing the marble to the high intensity heat flux. Each experiment utilised one of the three Penrice marble stone sizes seen in Table 4-6.

The open bed experiments were used to provide a comparison between the experiments conducted within the electric muffle furnace and the experiments conducted using solar simulator. The solar furnace experiments are used to quantify the benefits of using a closed system. These experiments were also used to validate the mathematical calcination modelling and multi-zone two-dimensional modelling.

4.6.1 Experimental Procedure

The initial open system experiments involved placing a collection of mono-sized marble in a square grid pattern onto the calcination platform, as shown in Figure 4-12, and illuminating it with radiant heat. Individual stones were systematically lifted from the platform and then returned to their original location to allow the mass of each stone to be calculated by the difference in measured mass. This experimental method provided a quick way to measure multiple stones during a single experiment. Additionally, the heat flux intensity differed between stone locations further optimising experimental time. The heat flux was measured

several times during each experiment to ensure that the lifted stone was placed into the same heat flux. After each experiment, the stones were collected and their quality assessed using Australian standard test methods for limes and limestone. The intensity of the radiation to which each marble sample was exposed varied between successive experiments of the same sized stone until hard burning of the surface of the Penrice marble became obvious.

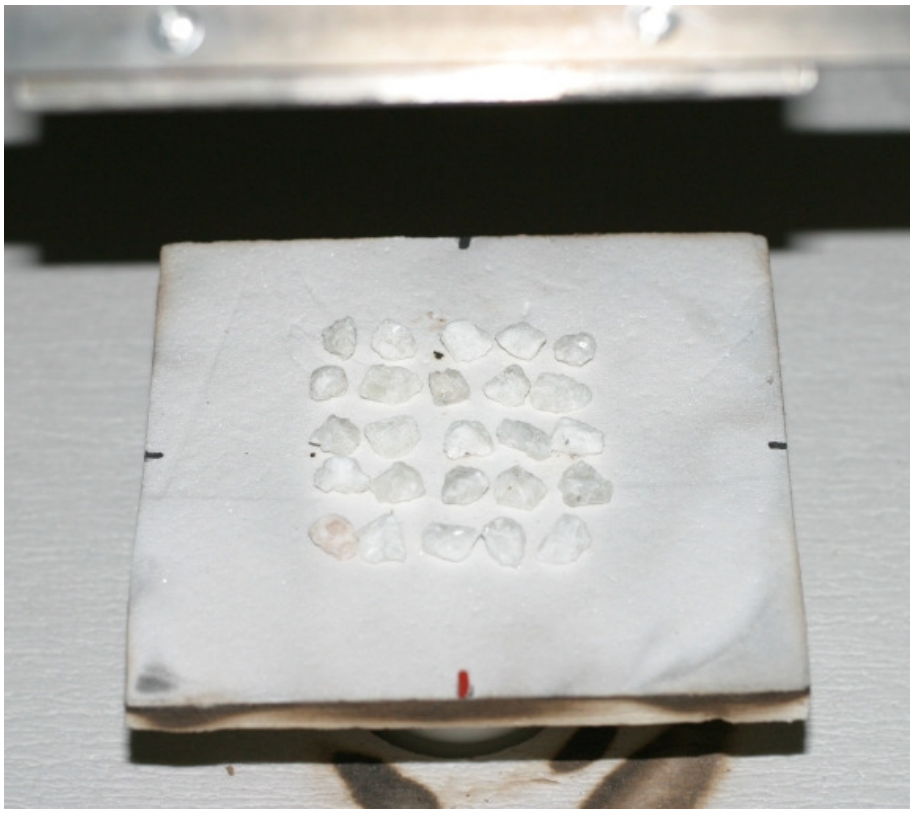

Figure 4-12: Photograph of one gram marble samples placed on the calcination platform ready for exposure to the simulated solar radiation.

The closed system solar furnace experiments involved placing a single stone of either 0.333g, 1.000g, or 3.000g onto the calcination platform, closing the furnace and exposing it to the radiation beam. The multiple stone experimental procedures were not adopted for the closed furnace experiments since it was not possible to employ the same lifting technique without fully opening the furnace and thus loosing substantial heat. The mass of the stone was continually measured and recorded during the decomposition reaction. The single stones were placed at the same location within the radiation beam to ensure a consistent heat flux and also a comparison between open and closed systems. The intensity of the radiant heat flux was increased, until significant hard burning of the surface became apparent for each of the three stone sizes.

4.7 Experimental Solar Furnace

The size and shape of the solar furnace was restricted by the power output of the xenon radiation source and the results from the zero dimensional modelling respectively. The walls of the experimental furnace were constructed from 50mm thick FiberFrax Ceramic Fiber Duraboard, which is the same material used for the calcination platform. The calcination platform provided a false floor within the furnace that could be raised or lowered to increase or decrease respectively the intensity of the direct radiant heat flux onto the marble stones. The indirect (reflected and emitted) radiant heat flux also varied according to the internal surface area of the furnace. A sectional drawing (with the side wall removed) of the solar furnace positioned in front of the lamphouse is shown in Figure 4-13.

The uninsulated mirror formed the roof of the furnace. The mirror was angled at 45° and measured 200mm high x 140mm wide. The temperature of the mirror was continually measured so that the heat loss from the heated mirror was able to be calculated. This temperature measurement also allowed the reflectivity of the mirror to be monitored.

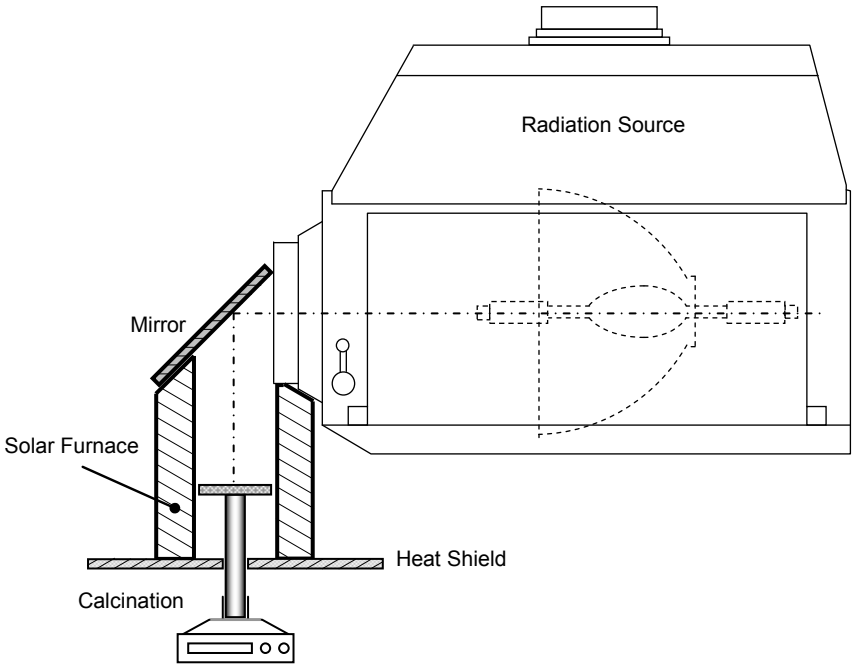

Figure 4-13: Sectional drawing of the solar furnace in front of the lamphouse with side wall removed for clarity.

The cross sectional profile of the solar furnace was square in shape with internal wall lengths of 110mm. A gap of approximately 2mm was maintained between the edge of the platform and the furnace wall to ensure free vertical movement of the calcination platform on the analytical balance. Unfortunately this gap allowed a small amount of convective heat loss. The height of the platform was adjusted by 75mm with the maximum and minimum distance

of the platform surface being 100mm and 50mm from the focal point, respectively. The heat shield, through which the alumina tube penetrated, further enclosed the furnace at the bottom. A gap of approximately 2mm was maintained between the alumina tube and the heat shield to allow free movement of the tube. This gap allowed a small amount of heat loss through convection. Pins were used to secure the side walls to the heat shield.

Figure 4-14: Photograph of the solar furnace with the rear wall removed, showing the calcination platform system.

The radiation beam passed through the lamphouse outlet into the furnace through an inlet of 110mm in diameter. The side walls were positioned between the mirror and the front of the lamphouse to completely seal the top section of the solar furnace. The rear wall provided access to the interior of the furnace as shown in Figure 4-14. It was positioned between the

mirror at the top, the heat shield at the bottom and the walls on each side. The rear wall was removed by tilting the top of the refractory into the furnace and sliding the bottom out. With the wall removed full access to the top surface of the calcination platform was achieved. Pins were used to secure the rear wall to the side walls.

4.7.1 Temperature Measurements within the Furnace

The temperature within the solar furnace was measured at 25 locations within the walls of the furnace, shown in Figure 4-15. Bare wire K type thermocouples were inserted from the outside of the furnace into the FiberFrax material at a distance of approximately 0.5mm from the inner surface of the furnace. The thermocouples were calibrated using the methods described in Section 4.2.

Eight permanent thermocouples were inserted at the locations shown as solid circles in Figure 4-15 and remained there for all of the experiments. Heat transfer compound was used to enhance heat transfer between the walls surface and the thermocouple. A single movable thermocouple was used for the remaining temperature measurement locations. This thermocouple was inserted into each measurement position and allowed to reach a steady state which was assumed to be ±1°C for 2 minutes, before the measurement was recorded. The external wall temperature was also measured in the middle of each of the four walls using a hand held K-type thermocouple, surface probe. The full set of measured temperatures for both the internal and external wall surfaces are displayed in Appendix E. A summary of these measured temperatures is displayed in Chapter 8 as Table 8-8.

Temperature measurements were taken twice during each experiment with the average temperature being calculated. The first measurement was taken 3 minutes after stone insertion and the second measurement a time identified to be halfway through the calcination process, through the use of the continual mass measurement. The temperature measurement positions lower on the furnace walls became obscured by the calcination platform when it was raised for the higher heat flux calcination experiments.

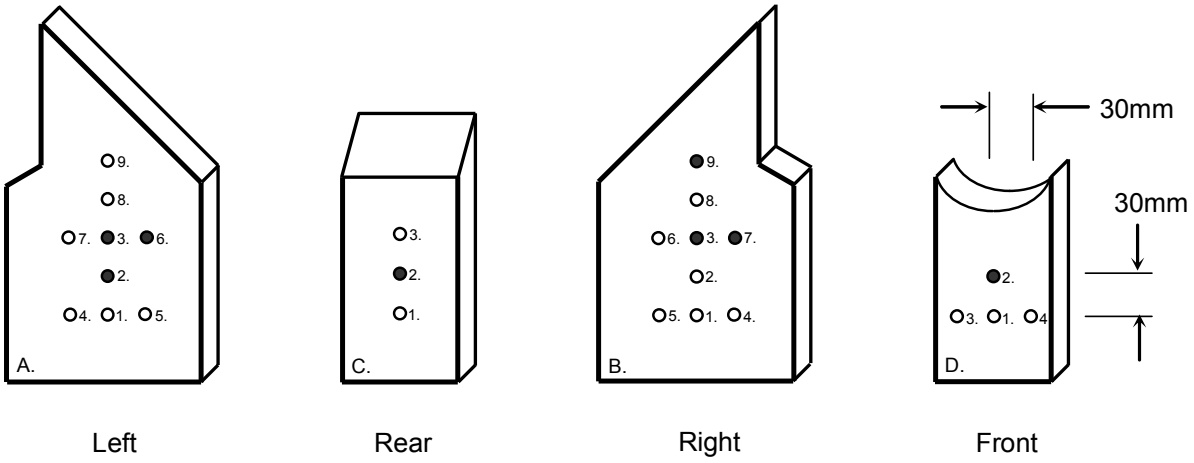

Figure 4-15: Pictorial representation of the walls of the solar furnace showing the locations of the permanent (solid) and transitional (white) temperature measurement points.

4.7.2 Experimental Procedure

With the solar furnace closed, the radiation source was turned on and allowed to reach operating temperature, which occurred approximately within 1 hour. The deflection mirror and solar furnace temperatures were monitored to ensure a steady state temperature was reached. A steady state was assumed to be when the temperature had not changed by more than 1% for 2 minutes. The analytical balance was then calibrated and re-zeroed. A scaled photograph was then taken from the top of the stone, which was used to show (and compare) the size and shape of the marble sample. The initial mass of the stone was also displayed as well as the time and date of the experiment.

The rear wall of the furnace was removed and the single stone placed on to the calcination platform. A digital image of the calcination platform with stone was then taken so that the heat flux could be calculated using the digital imagery methods discussed in detail in Chapter 5. The rear wall was repositioned to close the furnace and the data collection and temperature measurement process begun. The internal and external temperature of all the walls were measured and recorded periodically as described in Section 4.7.1 above.

The mass loss measurements were displayed on a computer and continually monitored. The calcination reaction was considered finished when the mass of the stone stopped reducing and remained relatively stable for approximately 5 minutes. As an additional check, the measured mass was compared to the theoretical loss on ignition mass to verify the completion of calcination.

The stone was then carefully removed from the furnace and placed within a desiccator and allowed to cool. A photograph of the stone was then taken which recorded the size and shape of the specimen after calcination. It was then placed within a plastic bag and a partial vacuum made before sealing the bag. The bag was then labelled and placed within a cool, dry location.

The recorded mass loss data was analysed and displayed within calcination profile plots which showed the loss of mass over time. The rate of the calcination reaction was calculated from the slope of the calcination profile. The radiant heat flux which the stone was exposed to was calculated.

Chapter 5

Radiant Heat Flux Distribution Measurement

5.1 Introduction

This chapter describes the four methods used to measure and calculate the distribution of heat flux within the radiation beam from the lamp. These measurements provide the heat flux that the Penrice marble was exposed to during each of the calcination experiments.

The 5000 W bulb was located horizontally within a cinema projection lamphouse, as shown in Figure 5-1. The radiation-emitting plasma arc within the bulb was positioned at the foci of an elliptical reflector, which directed the radiation beam horizontally through the aperture at the front of the lamphouse. The elliptical nature of the reflector produced a converging radiation beam with a focal point approximately 210mm from the aperture.

Distances from the focal point are defined using the letter S and the beam diameter characterised by D_b. The coordinate system is defined such that the X and Y axis are horizontal and Z axis vertical, as displayed in Figure 5-1.

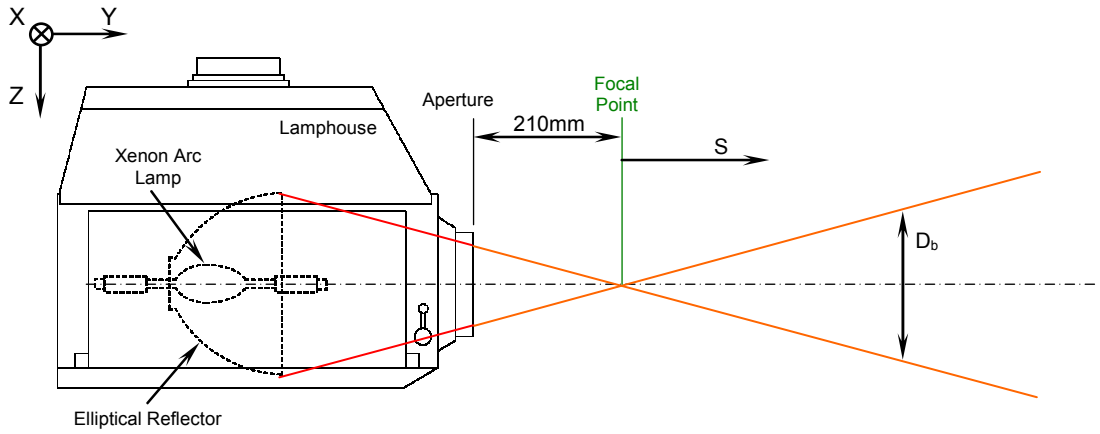

Figure 5-1: Dimensional parameters used to characterise the radiation beam emitting from the lamphouse.

The converging radiation beam increases to a maximum heat flux intensity at the focal point. The intensity then decreases as the radiation beam diverges away from the focal point. To determine the cross sectional area of the beam at the focal point, a K-23 insulating fire brick (Thermal Ceramics, Australia) was placed at the aperture and moved towards the focal point until a minimum beam diameter was observed. The minimum diameter was measured to be 12mm.

Four complementary methods for measuring and calculating the heat flux within the regions of interest were employed. The simplest method involved calculating the conversion efficiency of the xenon short-arc bulb to produce radiation from the electrical energy supply. The second method involved measuring the temperature of a known surface when illuminated by the radiation beam. The third method uses two total heat flux transducers to directly measure the heat flux within the beam and the fourth method involved using digital imagery to compare pixel level intensity with measured heat flux.

5.2 Heat Flux from Electrical Power Supply

The first estimate of the radiant heat flux within the radiation beam delivered by the xenon arc bulb was through the calculation of the conversion of the electrical power supply into radiant energy. This involved using the measured input voltage and amperage supplied to the bulb and determining the efficiency of the conversion of the electrical energy into useful radiation energy. The efficiency of the conversion is defined as being the usable output energy divided by the input energy. This calculation is often confused with the luminous efficacy, which is the efficiency of conversion of electrical power into light; the visible spectrum of radiation.

During the experiments, the voltage and direct current (DC) power supply to the bulb was measured and recorded. Both remained relatively constant throughout the experiments with the current measured at 137.3 ± 0.2 Amps and the voltage at 30.8 ± 0.2 Volts. The total power supplied was therefore: Volts x Amps = 4229 ± 34 Watts.

As discussed in Section 4.5.2 about 80% of the electrical energy put into XBO lamps is converted into electromagnetic radiation. The rest is lost through conduction through the electrode holders and convective heat loss due to the cooling fans incorporated into the lamphouse. Only about 60% of the electrical energy used is radiated by the electric arc, and most of this is in the invisible near infrared region. The remaining 20% of the radiation originates from the electrodes (mainly the anode) and from the bulb glass which reaches a temperature of approximately 700°C.

Oriel Optics, a supplier of specialty optics such as solar simulators, provided a breakdown for a typical xenon arc lamp of the percentage of energy emitted within each spectral band in their optical instrumentation book, Oriel Instruments (1998). The table has been reproduced in Table 5-1. it should be noted that there is an inconsistency of 0.2% within this data, since

the total cumulative percentage is more than 100%, but this accuracy is sufficient for the present purposes.

Table 5-1: Percentage of the total radiant energy emitted within the UV, Visible and IR spectral bands from a xenon-arc bulb. Note: total = 100.2% (Source: Oriel Instruments,1998).

NOTE:
This table is included on page 138 of the print copy of the thesis held in the University of Adelaide Library.

There was also inconsistent data supplied by Dimitriadis (2002), from Nevtech Systems, who provided a table of spectral energy distribution between 200nm and to 1400nm for xenon-arc bulbs as a percentage of the electrical input. A shortened version of the table is shown in Table 5-2. The total conversion efficiency is 49%. It should be noted that this table does not include the spectrum range above 1400nm, which could contribute a further 9% according to Table 5-1.

Table 5-2: Conversion of electrical energy into radiation from xenon arc lamps. Note: total = 49%.

Total ultraviolet (200nm to 400nm)	2.32 %
Total visible (400nm to 700nm)	11.79 %
Total Infrared (700nm to 1400nm)	34.84 %
Total output energy to input energy	48.95%

No other conversion efficiency data for xenon arc lamps was available. Additionally the direct measurement of the percentage of radiation emitted from the bulb that it makes it through the lamphouse opening, as opposed to being ‘absorbed’ within the lamphouse was

also not possible. The measurement of the conversion efficiency of the 5000 Watt xenon short-arc bulb was unfortunately not practically feasible using the available tools.

Using the 4229 ± 34W electrical power supplied to the bulb during operation and assuming the conversion percentage of 49%, the output power within the radiation beam was calculated to be Q_{elec} = 2072 ± 17W. On this basis, and using the measured focal point diameter of 12mm, the average heat flux (q_{elec}) at the focal point was calculated to be 18.32 MW/m^2. The q_{elec} at any S distance from the focal point was then calculated by first calculating the beam diameter. This was achieved using the elliptical reflector diameter of 15" (381mm) and the half angle of the reflector which is 12.85° (see Section 4.5.3).

Figure 5-2 shows the calculated average heat flux q_{elec}, for the 49% conversion efficiency case at varying axial distances S along the beam from the focal point. Note the logarithmic second y-axis scaling for the q_{elec} heat flux which reaffirms the inverse squared nature of heat flux from a radiation source.

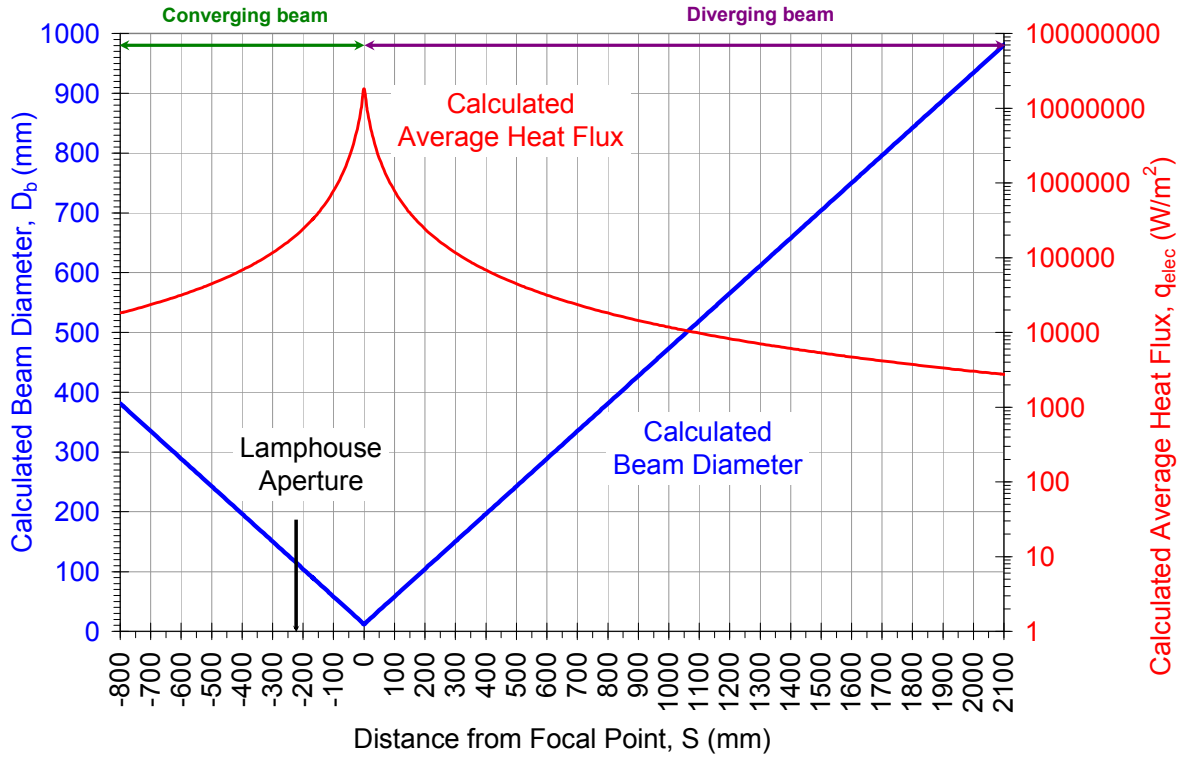

Figure 5-2: Calculated beam diameter D_b, and average heat flux q_{elec}, as a function of distance S, from focal point for 49% conversion efficiency.

This method of calculating the heat flux within the radiation beam is approximate due to the assumptions used. Nevertheless it provides a useful cross-check for other radiant heat flux measurement methods.

5.3 Surface Temperature Measurement

This method of calculating the heat flux within the radiation beam involves measuring the temperature on the surface of a ceramic fibre board illuminated by the radiation beam. The heat flux can be inferred from temperature since the two are directly related through emissivity.

The accurate measurement of the temperature on a surface is difficult. Mounting thermocouples directly upon the exposed surface does not measure the correct temperature because a thermocouple has different emissivity, and hence temperature, than the surface. Shielding the thermocouple from the direct radiation can provide some advantages, but this also introduces shading of the thermocouple and surface being heated. Additionally, the time lag between placing the thermocouple and recording the temperature can cause errors because either the steady state temperature is not reached or the shield becomes hotter than the surface being measured. The colour and shape of the shield needs careful consideration due to the possibility of reflection or concentration of the radiation.

Alternatively the use of an energy balance to mathematically account for all heat transfer processes to the thermocouple can be employed. The main variable within the energy balance is the physical size of the thermocouple junction. It is desirable therefore to minimise the size of the junction to reduce radiant and convective heat transfer and also to minimise its intrusiveness into the system. This approach is complex, and Brohez *et al*. (2004) recommend that it should be avoided when designing of the experimentation apparatus.

An approach to avoid direct radiation heat transfer to the thermocouple is to install it slightly below the surface. Using this approach, no radiation is directly incident upon the thermocouple, and the temperature measured would be solely of the material on which the radiation is incident. Holes are drilled from the opposite side of the material without penetrating the measuring surface. The remaining thickness of material between the end of the hole and the measuring surface should be no more than around 0.5mm thick. The thermocouple can then be inserted and temperature measurements taken on the inside the

measuring surface. The heat transfer via conduction through the thin layer of material can be calculated and the measured temperature adjusted as required.

Temperature measurements using the insertion method were therefore conducted using a 10mm thick sheet of FiberFrax Ceramic Fiber Duraboard mounted normal to the beam at various ‘S’ distances from the focal point. Two K-type thermocouples with 3mm diameter stainless steel (304) sheaths were calibrated as discussed in Chapter 4, and then inserted into the 3.1mm diameter holes drilled into the rear of the ceramic board. The locations of the measurement holes on the ceramic board are seen in Figure 5-3. The holes were drilled in a square grid pattern with equal Y and Z increments that were varied between 10mm to 50mm for the different diameter illumination spots depending on the diameter of the particular illumination spot. Conductive heat transfer in the X-Y plane between each measurement location was considered negligible because of the comparatively large distance between each location compared to the small surface to thermocouple distance.

The mirror mounting frame, discussed in Chapter 4, was removed from the equipment frame and the ceramic board positioned directly in front of the lamphouse aperture at distances from the focal point (S) of 400, 300, 250, 200, 150, 125, 100 and 90mm. Heat transfer compound was injected into each of the temperature measurement holes and then one of the two thermocouples inserted into the hole. The second thermocouple was used in an adjacent hole to measure the temperature in tandem and therefore reduce total measurement time. The temperature was manually recorded after a steady state was achieved which generally took around 2 minutes.

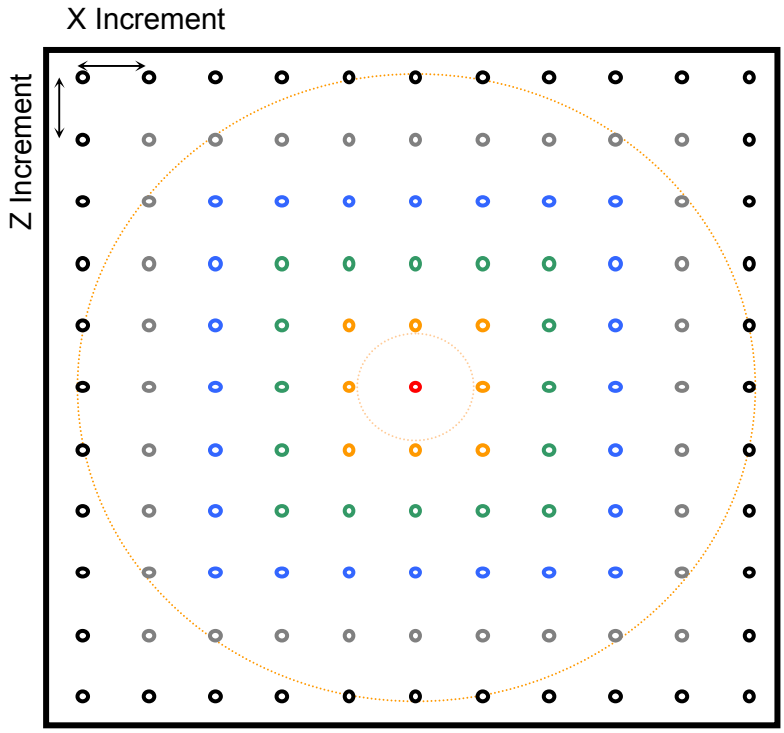

Figure 5-3: Diagram showing the temperature measurement locations on the ceramic board target illuminated by the radiation beam.

Tables 5-3 to 5-5 show the measured temperatures for S = 150mm, 100mm and 90mm respectively from the focal point. The D_b of the illumination spot for these S distances were approximately 90mm, 65mm and 55mm and the Y and Z measurement increments were 30mm, 22.5mm and 20mm respectively.

Table 5-3: Measurement of temperatures in centigrade taken at 30mm intervals with the board positioned normal to the beam at S = 150mm.

Z \ Y	-90mm	-60	-30	0	30	60	90
90mm	624 °C	645	626	633	614	646	634
60	630	674	678	675	660	698	661
30	627	680	762	799	805	720	675
0	612	655	740	646	820	730	682
-30	607	659	750	772	741	710	658
-60	638	655	664	669	664	658	607
-90	605	625	619	625	624	623	586

Table 5-4: Measurement of temperatures in centigrade taken at 22.5mm intervals with the board positioned normal to the beam at S = 100mm.

Z \ Y	-67.5mm	-45	-22.5	0	22.5	45	67.5
67.5mm	736 °C	737	752	765	746	696	715
45	741	813	824	847	832	788	726
22.5	726	819	901	911	895	829	764
0	685	738	823	845	942	847	779
-22.5	654	772	863	902	865	817	745
-45	696	768	777	826	788	792	721
-67.5	679	683	702	752	718	717	644

Table 5-5: Measurement of temperatures in centigrade taken at 20mm intervals with the board positioned normal to the beam at S = 90mm.

Z \ Y	-60mm	-40	-20	0	20	40	60
60mm	692 °C	716	812	805	822	826	742
40	707	830	939	954	937	873	770
20	813	930	993	965	974	945	833
0	860	976	984	910	1001	959	856
-20	789	911	959	967	960	918	805
-40	670	820	928	930	883	875	747
-60	643	682	784	742	752	748	733

Tables 5-3 to 5-5 show the considerable variability in the measured temperatures. This indicates a variation in the heat flux intensity within the radiation beam and can be attributed to the light bulb not being a point source and to imperfections in the surface of the elliptical reflector. An interesting aspect is that the central measured temperature, for all positions, is up to 21% lower than the measured temperatures surrounding it. The reason for this is the bulb is positioned axially in the ellipsoidal reflector (as shown in Figure 5.1), which reduces the reflection and emission of radiation along the centreline of the beam. The tables also show the location of the maximum measured temperature which is in the same location (immediately to the right (Y direction) of the central measurement) for all distances from the focal point. The bulb was re-aligned several times to try and increase uniformity, but without success.

To quantify the variation in measured temperature, a heat balance calculation was conducted. The heat balance calculation used the radiation Equation [5.1] and assumes that the ceramic board is a grey body at steady state and therefore the absorptivity and emissivity are constant and equal. The calculation also assumes that heat loss through conduction and convection are negligible.

$$q_{board} = \varepsilon\sigma\left(T_{board}^4 - T_{ambient}^4\right) \qquad [5.1]$$

where: Stephan~Boltzmann constant (σ) = 5.67×10^{-8} W/m^2 K^4

emissivity (ε) = 0.9 (source: Unifrax FiberFrax Duraboard (1999))

$T_{ambient}$ is the ambient temperature, and

T_{board} is the measured temperature of the board.

The calculated heat flux from the board, q_{board}, is then used to calculate the heat flux within the radiation beam illuminating the board, q_{beam}, by multiplying it by 110%, to account for the radiation reflected from the board's surface using the grey body assumption.

$$q_{beam} = 110\% \times q_{board} \qquad [5.2]$$

Tables 5-6 to 5-8 show the calculated heat flux for the temperatures measured previously at distances of S = 150mm, 100mm and 90mm respectively from the focal point.

Table 5-6: Calculated average heat flux (W/m^2) within the radiation beam at S = 150mm

Z \ Y	-90mm	-60	-30	0	30	60	90
90mm	35903 W/m^2	39428	36229	37384	34310	39602	37551
60	36886	44709	45477	44900	42098	49463	42281
30	36392	45864	63977	73694	75367	54141	44900
0	33998	41194	58673	39602	79675	56373	46254
-30	33226	41916	61041	66503	58906	51975	41735
-60	38226	41194	42832	43763	42832	41735	33226
-90	32921	36066	35100	36066	35903	35742	30126

Table 5-7: Calculated average heat flux (W/m^2) within the radiation beam at S = 100mm.

Z \ Y	-67.5mm	-45	-22.5	0	22.5	45	67.5
67.5mm	57744 W/m^2	57975	61524	64727	60085	49053	53050
45	58906	77643	80855	87890	83252	70698	55472
22.5	55472	79383	106196	109876	104033	82347	64476
0	46844	58207	80559	87260	121891	87890	68315
-22.5	41014	66503	93046	106560	93706	78800	59848
-45	49053	65484	67793	81449	70698	71776	54361
-67.5	45670	46450	50290	61524	53703	53484	39255

Table 5-8: Calculated average heat flux (W/m^2) within the radiation beam at S = 90mm.

Z \ Y	-60mm	-40	-20	0	20	40	60
60mm	48241 W/m^2	53267	77356	75367	80263	81449	59141
40	51339	82648	120687	126795	119889	96381	65992
20	77643	117129	143759	131420	135296	123103	83555
0	92062	136169	139702	109504	147439	128882	90763
-20	70966	109876	128882	132274	129302	112508	75367
-40	43951	79675	116349	117129	99805	97059	60323
-60	39082	46254	69631	59141	61524	60562	57056

These calculated heat fluxes assume that the manufacturer's specifications for the emissivity of the ceramic board, (ε) = 0.9, are correct. Unfortunately the independent measurement of the board's emissivity was not possible and the test methods used by the manufacturer were not available.

The total power Q_{temp}, at each measurement distance, S, was calculated by multiplying the heat flux by the square of the distance between each temperature measurement, i.e. an integration of the heat flux profile. This Q_{temp} is calculated for each S distance and compared to the total power Q_{elec} calculation from Section 5.2 and display in Table 5-9.

Table 5-9: The total power within the radiation beam calculated from the temperature measurements.

Distance from focal point S (mm)	**Surface temperature method Q_{temp} (Watts)**	**Electrical conversion method Q_{elec} (Watts)**	**Percentage difference $\frac{(Q_{elec} - Q_{temp})}{Q_{elec}}$ %**
150	1978	2072	4.54
100	1732	2072	16.41
90	1825	2072	11.92

The Q_{temp} column shows a 12.4% difference between the maximum and minimum values. There appears to be no particular pattern when comparing column S and Q_{temp}. This may be because the power in the wings of the profile has been accounted for by assuming that the beam profile is Gaussian.

The percentage difference column displays a maximum of 16.41% difference between the two total beam power calculation methods. It should be noted that the calculation of Q_{elec} assumes that the electrical conversion efficiency is 49% and that the entire radiation beam is used. Clearly if this percentage was lower or some of the beam was attenuated, then this percentage difference could be lower.

This method of measuring and calculating the heat flux profile is time consuming and cumbersome to measure and assumes the heat flux surrounding each measurement point is uniform in intensity. Like the electrical conversion calculation method of Section 5.2 the surface temperature method has provided useful information regarding the variation in heat flux across the beam, i.e. the heat flux profile of the beam. The next stage is to use total heat flux transducers to measure the heat flux within the radiation beam.

5.4 Heat Flux Transducer Measurement

The radiant heat flux from the xenon arc lamp radiation source was measured directly using two Medtherm 64-Series Schmidt- Boelter heat flux transducers. The specifications for these heat flux transducers can be seen in Chapter 4, Section 4.5.4. These heat flux transducers are calibrated up to 11.35 kW/m^2 with an over-range capacity of up to 56 kW/m^2. The heat flux in the near focal region where calcination experiments were conducted is considerably

higher than this. Measurements at distances from the focal point, denoted here using the letter 'S', at lower heat flux were taken and an extrapolation of the data calculated for the heat flux in the near focal region. The value of the maximum heat flux, denoted here as Q_{max}, at the various distances from the focal point, S, were used for this extrapolation, because the maximum heat flux was easily identified within the beam and its radial location within the beam remained relatively constant.

5.4.1 Measurement Procedure

The transducer heat flux measurements were taken both with and without the aluminium deflection mirror placed in front of the lamphouse opening. The comparison between these heat flux measurements is used to quantify the reflectivity of the mirror. A pictorial representation of the experimental set-up without the aluminium mirror, as well as the transducer measurement locations, is shown in Figure 5-4. A similar schematic, but with the aluminium mirror in location and showing relevant dimensions is shown in Figure 5-5. Two separate mirror positions were used.

The no mirror measurements were taken at four distances from Focal Point A, corresponding to S_1 = 540mm, S_2 = 690mm, S_3 = 790mm, and S_4 = 1040mm. Using the maximum over range of 56 kW/m^2 the closest distance to the focal point that the transducers could be placed was S = 460mm. It should be noted that 56 kW/m^2 is outside of the nominal calibration range.

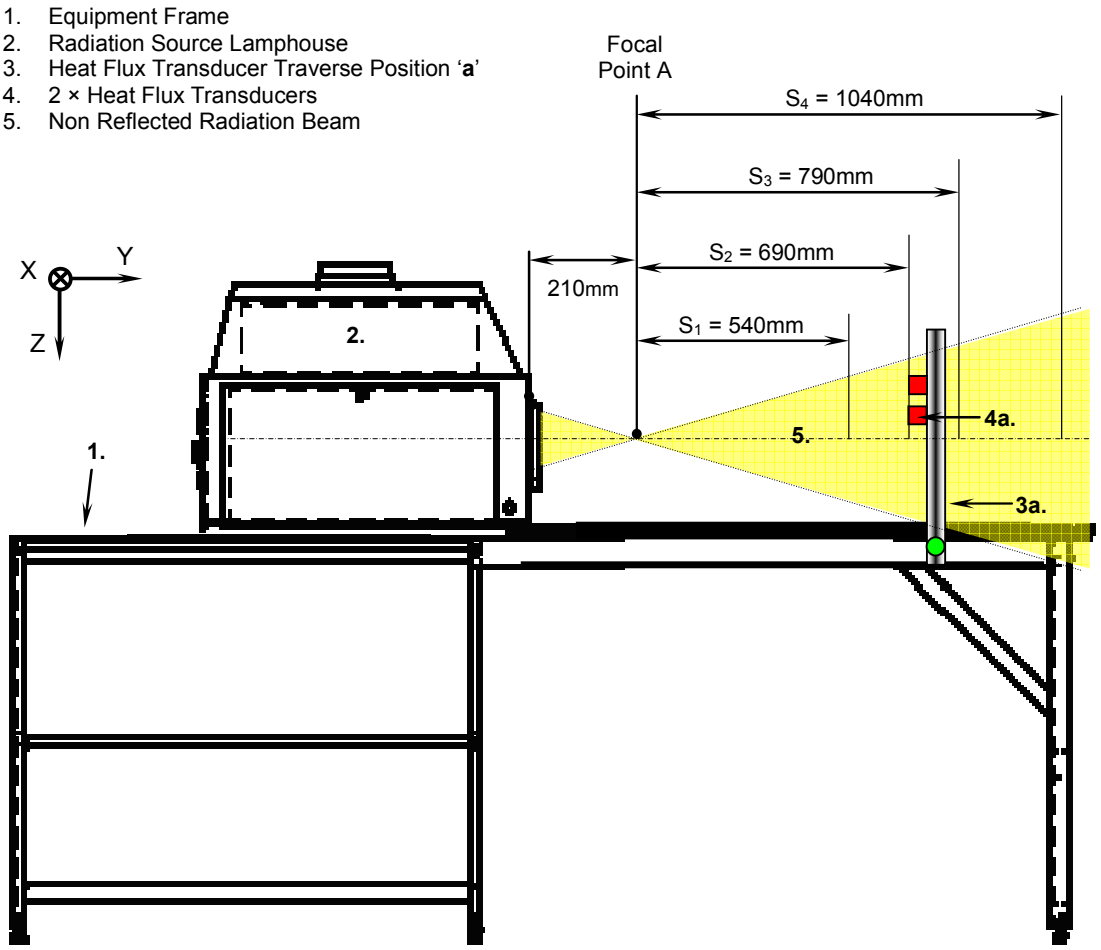

Figure 5-4: Heat flux transducer distances from the focal point for the 'no mirror' measurements.

The two total heat flux transducers were mounted alongside each other on a two dimensional traverse (up and down (Z direction) and side to side (X direction)) which was also incrementally repositioned at the four S distances from the focal point (Y direction)). The transducers were mounted 50mm apart, which was the size of the measurement grid, similar to that shown in Figure 5-3.

With the mirror placed in front of the lamphouse, two separate mirror positions were used, which are shown in Figure 5-5. The first mirror position was located 300mm from the front of the lamphouse, which is 90mm from the focal point on the diverging (far) side of Focal Point A. The transducer measurement locations were taken vertically below the mirror at distances of 450mm, 600mm, and 700mm from the centre of the mirror. These therefore correspond to a distance from focal point A of S_5 = 540mm, S_6 = 690mm, and S_7 = 790mm. The second mirror position shown in Figure 5-5 was on the converging side of the focal point i.e. the mirror placed between the focal point and xenon lamp. The centre line of the mirror was 70mm from the front of the lamphouse with the focal point (Focal Point B) therefore

being located 140mm below the mirror. The heat flux transducer measurements were taken at 680mm from the mirror, which gives a beam path length of S_8 = 540mm from focal point B.

For both mirror positions, the two total heat flux transducers were mounted 50mm apart on a two dimensional (X, Y) plane traverse, which was incrementally repositioned for the third direction, Z axis, to vary the S distance. The traverse was moved in 50mm increments to achieve the measurement grid.

It should be noted that for each of the measurement points within the grid (up to 12×12 locations), 10 measurements were taken at a rate of 2 hertz over a measured time of 20 seconds.

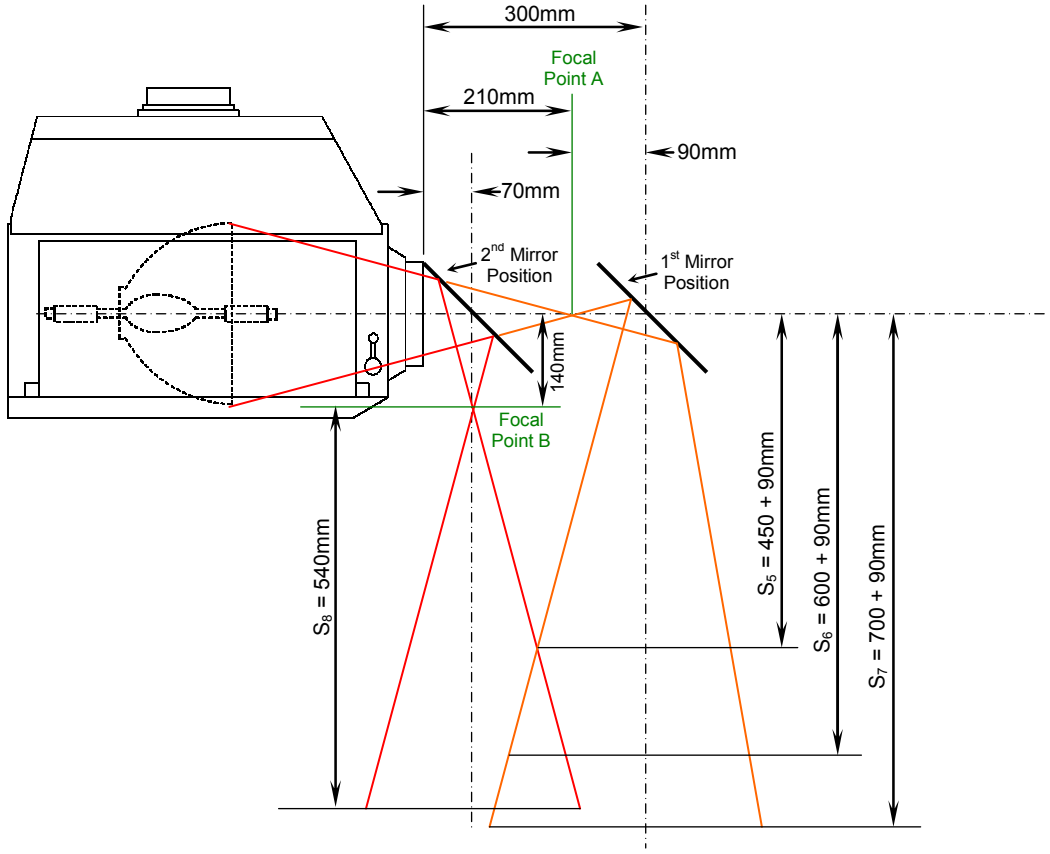

Figure 5-5: Transducer measurement distances for the two mirror positions.

5.4.2 Data Collection and Analysis

Data logging was achieved through a Datascan analogue scanner module 7220 unit. The logger provided a 16bit, real time interface (RS-232) between the sensors (in this case heat flux transducers and thermocouples) and the computer, which was used for saving the data. The data acquisition software, RS Recorder Application Version 2.3 by Measurement

Systems Ltd, recorded the data as CSV-files, which was easily transferred to Microsoft Excel for analysis.

The recorded data was first transferred into an excel spreadsheet where the measured milli-volt values were transformed into matrix form. Using the calibration curves for the transducers, the milli-volt values were transformed into heat flux. A plot of the heat flux profile verses radial distance from the centre of the beam were made. The data was then transferred into MatLab where it was easier to manipulate into contour plots. The centred, contour plots from each S distance were collated and an average taken to produce a single heat flux profile of the beam. Interpolation was used on the contour plots to calculate the heat flux between the measurement locations. The contour plots were then averaged and normalised so that the location of the maximum heat flux for each distance from the focal point could be overlaid and calculations made to predict the maximum heat flux at distances closer to the focal point. It should be noted that the ambient room lighting represented approximately 1% of the maximum average heat flux for the S_4 measurement. This reduced to 0.6% for S_3, 0.4% for S_2 and 0.3% for S_1.

5.4.3 Transducer Measurement Results

The first heat flux transducer measurements were taken without the mirror in place. Figures 5-6 to 5-9 show the measured heat flux within the radiation beam for the axial distances from the focal point, S_1 = 540mm, S_2 = 690mm, S_3 = 790mm, and S_4 = 1040mm, respectively. Contour lines of equivalent radiation intensity (isorad) were produced, with the intermediate locations between measurement locations being calculated using interpolation. ISO 9488:1999 currently defines an *isorad* as ' a curve, drawn on a map, indicating sites of equal solar irradiation (W/m^2) during a given interval of time.

The displayed measurements, Figures 5-6 to 5-9, are from the same heat flux transducer, No. 92242. Measurements from the other heat flux transducer, No.92241 vary by a maximum 1% due to minor differences in horizontal and vertical alignment.

Comparing the heat flux profiles, Figures 5-6 to 5-9, there is a distinct decrease in the diameter of the illumination spot as the distance to the focal point decreases. There is a low intensity at the centre of the heat flux profile surrounded by two crescent shaped regions of higher intensity. Within the middle of these crescents, the heat flux appears to be relatively uniform in intensity, compared to the large variation seen towards the middle and outer edges, where the isorad lines are closer together. The maximum heat flux is located to the

right and slightly lower of the centre. The value of the maximum measured heat flux for each axial distance from the focal point is shown in Table 5-10. It should be noted that the value of maximum heat flux is desired because it is the heat flux that the single Penrice marble samples were exposed too during the calcination experiments. The maximum measured heat flux increases as the distance to the focal point decreases.

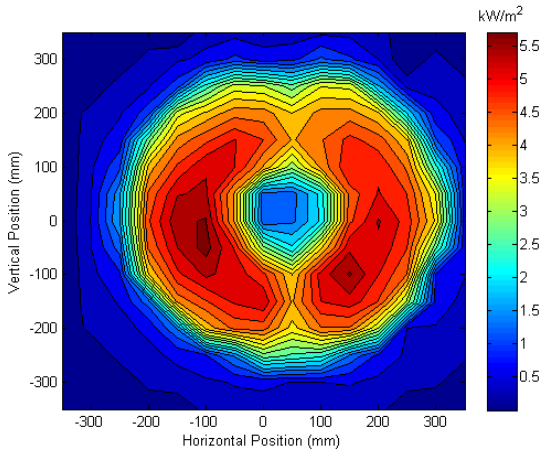

Figure 5-6: Transducer (92242) measurement of the heat flux at an axial distance S_4 = 1040mm from the focal point.

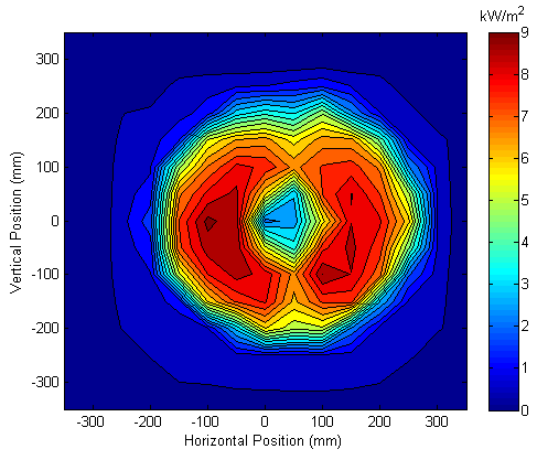

Figure 5-7: Transducer (92242) measurement of the heat flux at an axial distance S_3 = 790mm from the focal point.

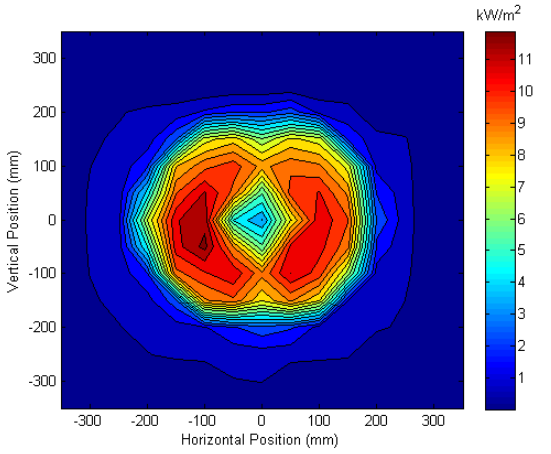

Figure 5-8: Transducer (92242) measurement of the heat flux at an axial distance S_2 = 690mm from the focal point.

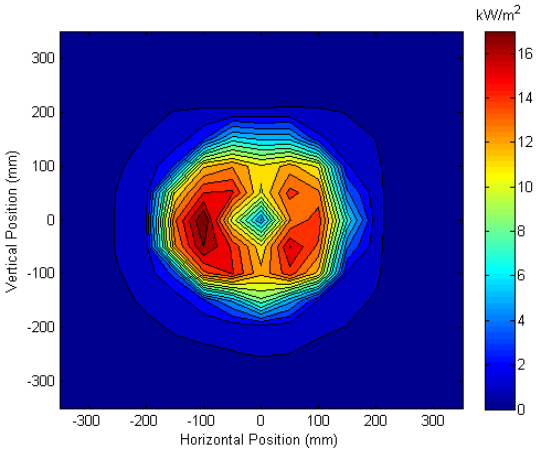

Figure 5-9: Transducer (92242) measurement of the heat flux at an axial distance S_1 = 540mm from the focal point.

Table 5-10: Maximum heat flux measured for the 'no mirror' case at four axial distances S, from the focal point.

Distance from focal point S (mm)	**Maximum measured heat flux without mirror q_{max} kW/m^2**
S_4 = 1040	5.82
S_3 = 790	9.15
S_2= 690	12.16
S_1 = 540	18.04

The values in Table 5-10 were used to calculate a power law Equation [5.3] which can be used to describe the maximum heat flux at any distance (**S**) from the focal point.

$$q_{max} = 6211.8 \times S^{-1.7408} \quad W/m^2 \qquad [5.3]$$

A plot of this equation is displayed in Figure 5-10 which shows the comparison between the measured heat flux values and the calculated power law Equation [5.3].

There is uncertainty within the measured maximum values and therefore also in the calculated extrapolation. To ascertain the accuracy of the measured data the coefficient of determination '**R^2**' was calculated using statistical analysis. With a value of R^2 = 0.998, Equation [5.3] represents the measured data closely.

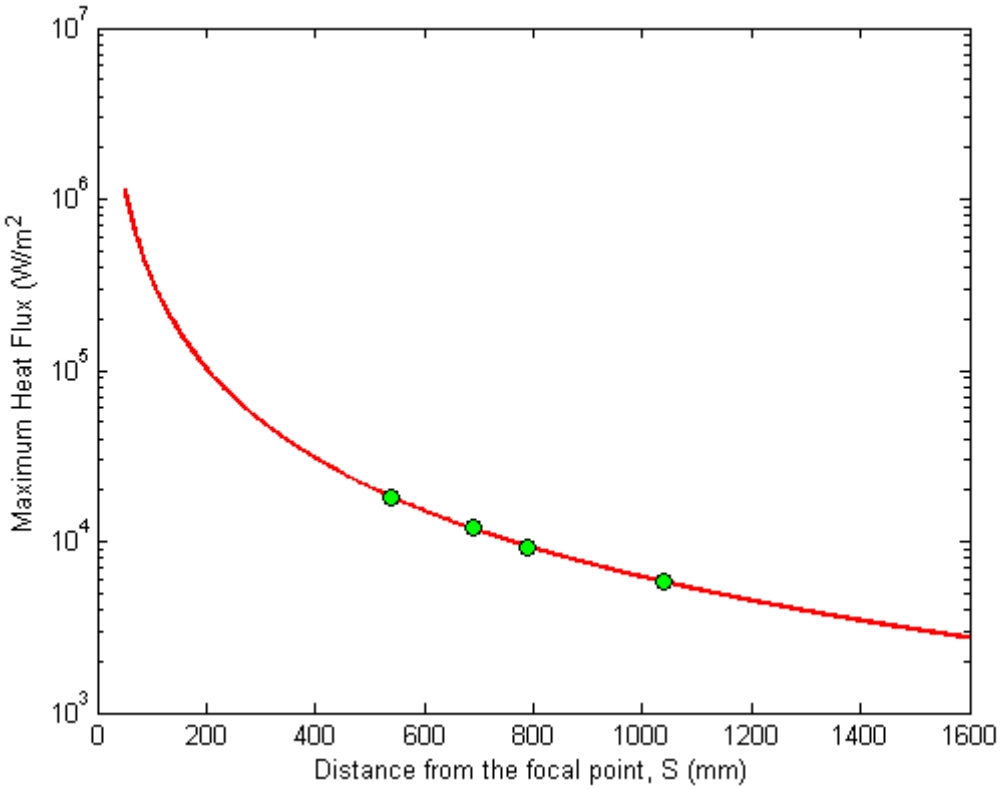

Figure 5-10: Comparison of measured (●) and calculated (—) using Eq [5.3] maximum heat flux for axial distances from the focal point.

The heat flux profile in the near focal region where the calcination experiments were conducted was calculated using the four measurements. The calculation procedure began by first averaging the two transducer measurement sets recorded at each of the four distances S. This produced a single heat flux profile for each distance from the focal point. To directly compare the four resulting measurement sets, the size of the measurement grids needed to be first normalised to a common size. This was achieved by scaling the coordinate position of each measurement, to the radial location of the maximum measured heat flux. The profiles were then centred to ensure the circumferences from all resulting heat flux profiles would superimpose. The heat flux values were then normalised to the maximum measured heat flux and their root mean squared (rms) values calculated using Equation [5.4]. The resulting profile is shown in Figure 5-11.

$$q_{rms} = \sqrt{\frac{1}{4}\sum_{i=1}^{4} q_i^2} = \sqrt{\frac{q_1^2 + q_2^2 + q_3^2 + q_4^2}{4}} \qquad [5.4]$$

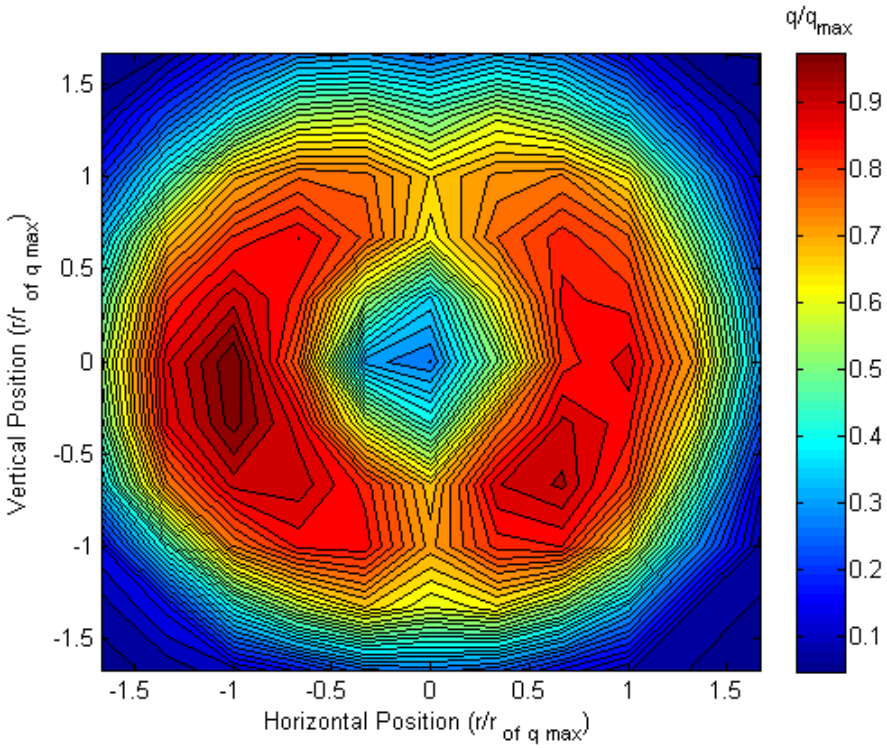

Figure 5-11: Normalised rms heat flux profile of the radiation beam, without a mirror.

The mirror was then placed within the radiation beam at a location 90mm from the focal point, on the diverging side of the beam, as shown in Figure 5-5. Three sets of measurements were taken with the transducers located at distances S_5 = 540mm, S_6 = 690mm and S_7 = 790mm from the focal point. Figures 5-12 to 5-14 were produced from the measurements. The displayed profiles are the average between the two transducer measurements.

The profiles show a low value of heat flux positioned in the middle, surrounded by two crescents of higher heat fluxes. Also seen is a decrease in illumination spot diameter as the distance from the radiation beam focal point decreases. The maximum heat flux is positioned to the left and slightly higher than the centre, which is the expected inverse of the direct 'no mirror' measurements. The maximum heat flux for each axial distance is shown in Table 5-11. A comparison between the heat flux at the same axial distance with and without the mirror is also shown in Table 5-11.

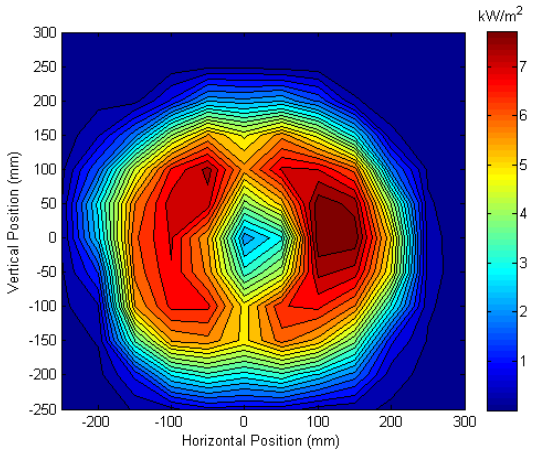

Figure 5-12: Heat flux measurements for S_7 = 790mm, with the 45° aluminium mirror located at 90mm from the focal point.

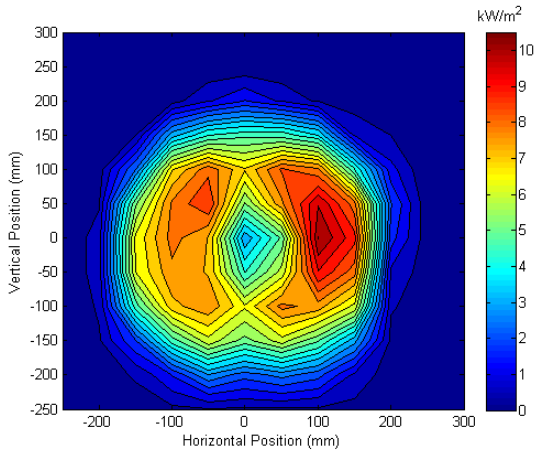

Figure 5-13: Heat flux measurements for S_6 = 690mm, with the 45° aluminium mirror located at 90mm from the focal point.

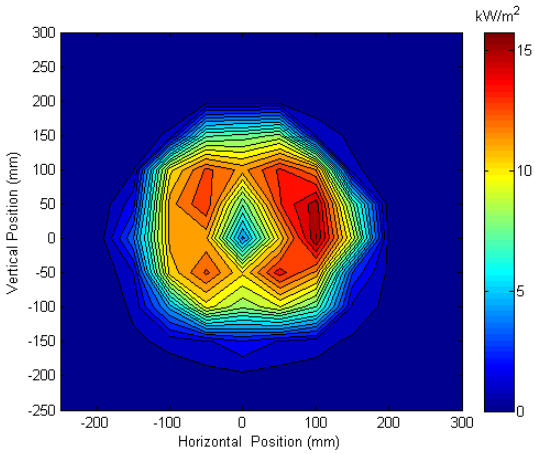

Figure 5-14: Heat flux measurements for S_5 = 540mm, with the 45° aluminium mirror located at 90mm from the focal point.

The comparison of maximum heat flux in Table 5-11 with the 'no mirror' measurements indicates a linear relationship between the distance from the focal point and the difference between the mirror and no mirror measurements. This relationship could have arisen from the degradation of the reflective nature of the mirror. The appearance of white oxidisation on the mirrors surface was observed. The mirror was manually polished but the oxidation tarnish could not be removed. Before removing the mirror and getting it mechanically polished, the remaining transducers measurements with the mirror located in the second position 70mm before the focal point were conducted.

Table 5-11: Maximum measured heat flux for the first mirror case at three axial distances, S, from the focal point and comparison to the 'no mirror' measurement.

Distance from focal point S (mm)	**Distance from centreline of mirror (mm)**	**Maximum measured heat flux with mirror $q_{max,m1}$ kW/m²**	**Difference between mirror and no mirror measurement** $\frac{q_{max,m1} - q_{max}}{q_{max}}$ %
S_7 = 790	700	8.36	- 8.6%
S_6 = 690	600	10.91	- 10.3%
S_5 = 540	450	15.79	- 12.5%

The measured maximum heat fluxes from Table 5-11 were used to produce the power law Equation [5.4] which can be used to describe the maximum heat flux at any distance (**S**) from the focal point for this particular mirror arrangement.

$$q_{max,m1} = 5758.7 \times S^{-1.65} \quad W/m^2 \qquad [5.5]$$

A plot of this equation is displayed in Figure 5-15 which shows the comparison between the measured maximum heat flux values and the calculated power law Equation [5.5]. The coefficient of determination for Equation [5.5] was calculated using statistical analysis and is R^2 = 0.996, which therefore represents the measured data closely.

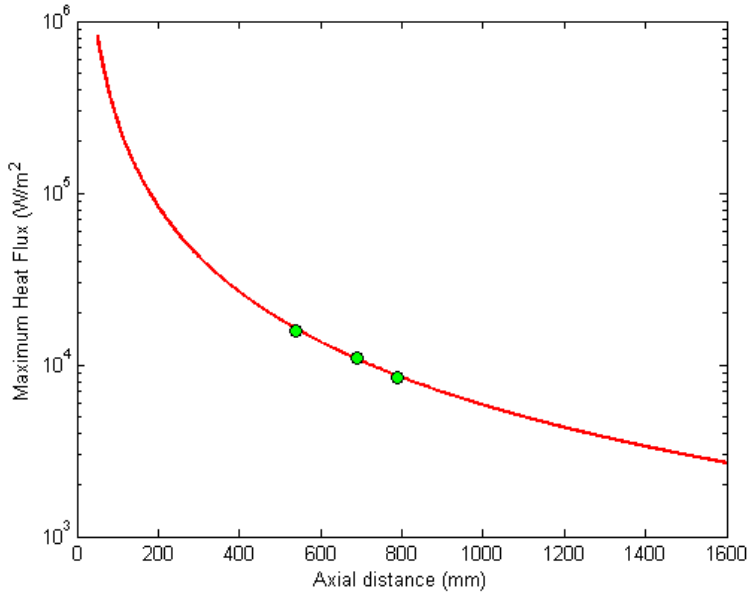

Figure 5-15: Comparison of measured (●) and calculated (—) using Eq [5.5] maximum heat flux for axial distances from the focal point when the mirror was located 90mm from the focal point.

The mirror was then moved to the second location 70mm before the focal point, as shown in Figure 5-5. The location of the focal point was therefore located 140mm below the mirror. The heat flux transducer measurements were taken at 680mm from the mirror, which gives a beam path length, S_8 = 540mm from the focal point. Figure 5-16 shows the results after the two transducer measurements have been averaged. The heat flux profile is similar to the other mirror measurements with two crescents of higher heat flux surrounding the centre lower heat flux. The location of the maximum is to the left and slightly higher than the centre of the illumination. The maximum measured heat flux $q_{max,m2}$ is displayed in Table 5-12. The table also compares the two mirror cases as well as the 'no mirror' case.

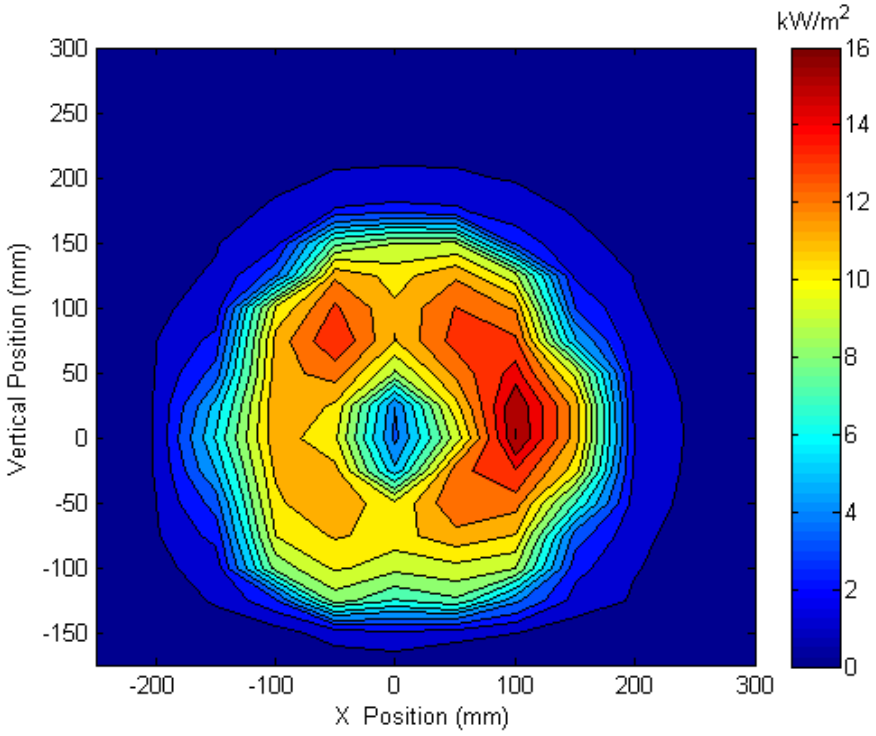

Figure 5-16: Heat flux measurements for S_8 = 540mm with the 45° aluminium mirror located before the focal point.

Table 5-12: Maximum measured heat flux for the second mirror case at an axial distances of S = 540mm from the focal point and comparison with the 'no mirror' and 1st mirror measurements

Distance from Focal Point S (mm)	**Maximum measured heat flux with mirror in second position $q_{max,m2}$ kW/m²**	**Difference between second mirror and no mirror measurement** $\frac{q_{max,m2} - q_{max}}{q_{max}}$ %	**Difference between second mirror and first mirror measurement** $\frac{q_{max,m2} - q_{max,m1}}{q_{max,m1}}$ %
S_8 = 540	16.03	- 11.2%	+ 1.5%

As seen in Table 5-12 the measurements using the mirror located before the focal point (second position) produce a similar maximum heat flux to the first mirror measurements. The slight increase in measured heat flux between the second and first mirror measurements show the increase in reflectivity gained by manual polishing the mirror. Due to time constraints these measurements were not repeated after the mirror was mechanically polished or repeated to directly compare the maximum heat flux between mirror positions only.

As expected the difference between the second mirror measurements and the no mirror measurements indicate the imperfect reflection from the mirror and thus the measured difference is slightly above 11%.

Only one distance S from the focal point was measured with the mirror at this location, the calculation of a power law equation to estimate the maximum heat flux in the near focal region was therefore not possible. The maximum heat flux is of interest here because this is the position that the single marble particles are located in the calcination experiments presented in Chapters 7 and 8.

In summary, the measurement of heat flux using the total heat flux transducers is time consuming and does not provide high spatial resolution. In addition the high intensity energy experienced in the near focal region is higher than the transducers can directly measure and therefore only an estimate can be made. Oxidation of the surface of the mirror over time means that measurement of the heat flux immediately prior to or following the experimental calcination of the stone is desirable. It was therefore decided to investigate an alternative measurement technique such as using digital imagery.

5.4.4 Error Analysis for Transducer Measurements

The specifications provided within the documentation for the two transducers, provided an indication of the measurement errors which can occur. The following tolerances are specified within Medtherm Corporation (2003):

- Accuracy : ± 3% for most ranges,
- Maximum Non-Linearity : ± 2% of full range,
- Repeatability : ± 0.5%,

Using the accuracy range specification, the actual heat flux for a measurement by the heat flux transducers of 16.03 kW/m^2 could range between 15.516 kW/m^2 and 16.484 kW/m^2 (i.e. $\pm$ 484 W/m^2).

The next source of measurement error was from the position of the heat flux transducer from the focal point. The transducers were positioned manually using scaled markings in the X, Y and Z axis of the two traverses. The uncertainty in the position of the transducers was estimated to be ± 0.5 mm in the X axis and ± 2 mm in Y axis and ± 5 mm in the Z axis. It should be remembered that the X and Y axis are perpendicular to the radiation beam and therefore only affect the position of the heat flux profile, while the Z axis is a change in the optical path length and thus the intensity of the measured heat flux.

The intensity of the measured heat flux (irradiance, ***I***) is proportional to the square of the optical path length (S) as seen in Equation [5.6], i.e. the distance of the transducers from the focal point.

$$I \propto \frac{1}{S^2} \qquad [5.6]$$

Using this relationship and Equation [5.5], the relative errors in heat flux measurements due to the possible variation in path length measured within these experiments are given in Table 5-13.

Table 5-13: Error in the heat flux intensity measurement due to path length accuracy.

Optical Path Length S (mm)	Difference in heat flux W/m^2	Percentage Difference
790 ± 5	± 90	± 1.04%
690 ± 5	± 128	± 1.19%
540 ± 5	± 246	± 1.51%

A summation of all the above errors, should the “worst case” in the measurements occur, are shown in Table 5-14.

Table 5-14: Maximum error in the heat flux intensity measurement due to all sources of error.

Nominal Optical Path Length S (mm)	Difference in heat flux W/m^2	Percentage Difference
790	± 349	± 4.05 %
690	± 453	± 4.21%
540	± 733	± 4.55%

5.5 Heat Flux Measurement Using Digital Imagery

This section describes the methods used to calculate and represent the radiation flux density distribution in the near focal region of the high intensity beam. A canon SLR digital camera was used to record an image of the reflected and emitted radiation from the calcination platform. The image was then processed using a computer which quantified the relationship between the recorded pixel level and the measured calibration heat flux. A digital image of the heat flux profile was produced, which displays contour lines of equivalent radiation intensity (isorad).

A Canon EF 50mm f/1.8 lens was used to focus the radiation from the calcination platform onto the Complementary Metal Oxide Semiconductor (CMOS) photoelectric light sensor within the SLR digital camera. The CMOS image sensor converts the optical image to an electric signal. When the radiation strikes the CMOS cell array (the photoactive region), it

causes each pixel cell to accumulate a small electric charge. The size of the electric charge from each pixel cell is directly proportional to the number of photons it receives. Additional circuitry within the camera then converts the voltage into digital information. The CMOS image sensor only responds to visible radiation and so the recorded energy level of each pixel needed to be calibrated against the measured heat flux.

The advantages of using a digital camera include a high spatial resolution, fast and repeatable measurement method in terms of data collection, and involves relatively affordable measurement equipment.

A review of indirect flux density measurement methods used by other researchers such as Schubnell *et al*. (1991), Steinfeld *et al*. (1992), Neumann and Groer (1996) and Ulmer *et al*. (2004) formed the basis of the methods used here. Steinfeld *et al*. (1992) reported using a similar method in which the power into their solar cavity was measured optically, which was then processed using a pixel-by-pixel image processing technique from which the flux contours of the isolation were calculated. Integration of the flux contours over the opening area gave them the total input power into the cavity. Neumann and Groer (1996) used a Flux and Temperature Measurement System (FATMES) within their investigation. Ulmer *et al*. (2004) produced a flux mapping system called PROHERMES which is similar to the digital image processing technique used within these measurements.

5.5.1 Experimental Arrangement for Digital Imagery

The experimental arrangement for the digital imagery is shown in Figure 5-17. The digital camera was mounted to a vertical traverse at an angle of 45° from the horizontal. The lens of the camera was focused on the centre of the Lambertian target, which was a 500mm × 500mm × 50mm thick ceramic fibre board. The front of the lens of the camera was approximately 985mm from the centre of the target board. The X,Y axis transducer traverse and fibre board platform could be raised in the Z axis direction as was required for the measurements of the shorter radiation path lengths. The camera was also raised together with the platform to maintain the same angle and distance for these shorter radiation path lengths.

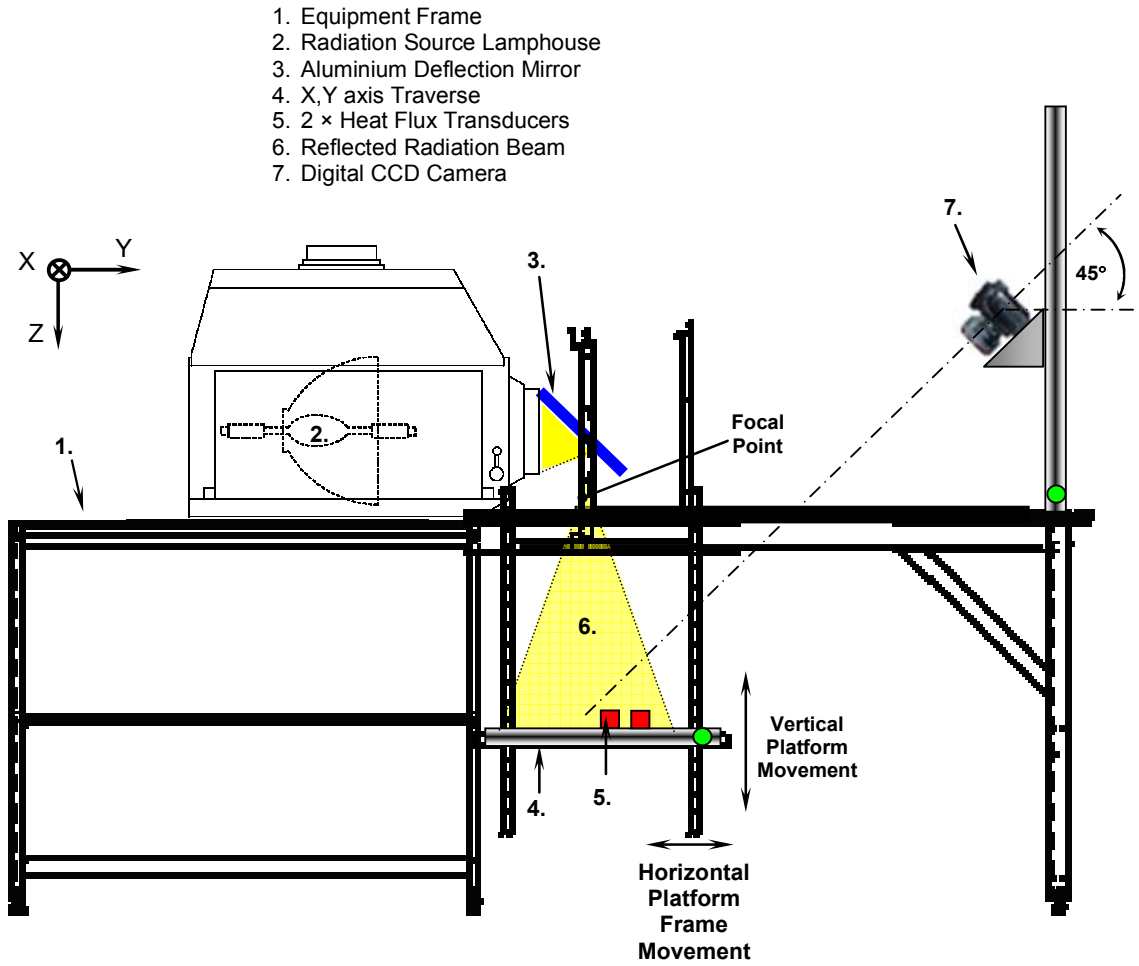

Figure 5-17: Pictorial diagram of the experimental setup used for the heat flux measurements using digital imagery.

5.5.1.1 Image Capturing

A Canon EOS D60 SLR digital camera with a Canon 50 mm EF f/1.8 lens was used to capture the heat flux images required during the experiments. The images were captured in Raw file format using an ISO sensitivity of 100. The aperture (f-stop) of the camera was set to 22 and the shutter speed varied between 60 and 90 according to the desired exposure level of the CMOS photoelectric light sensor. The lower shutter speed (60) provided a higher pixel level count and thus a greater measurement range, although at high heat flux intensities over-exposure was possible.

The CMOS imaging element was a high sensitivity, high resolution, single-plate sensor with 6.52 million effective pixels (3152 x 2068). Each pixel provided a 12 bit output and thus 4096 discrete tone levels were available, as described in Fraser (2004). A primary colour filter (Bayer-filter with colour filter of red, green and blue) and non removable low-pass filter were located in front of the CMOS sensor as designed by the manufacturer, Canon. The Raw

image files were stored on a removable 156 MB compact flash memory card until transferred to a personal computer.

5.5.1.2 Neutral Density Filter

A Hoya HMC Multicoated neutral density Filter ND400 was fitted to the 50 mm lens on the camera to reduce the overall exposure of the CMOS to the high intensity radiation. The ND400 filter has an attenuation factor of 400 which is an optical density of 2.7 or an *f* stop reduction of 9 or a transmittance of 1/500 (or 0.2%).

5.5.2 Image File Conversion

The images from the camera were transferred to a personal computer for processing and analysis. The Raw file images are unprocessed files and contain the intensity information for each Red, Green, and Blue pixel as was generated by the Bayer filter in front of the CMOS sensor. An advantage of using Raw file images is that it is not gamma (γ) corrected (i.e. γ = 1), which means that the pixel value is directly proportional to the irradiance, as discussed by Fraser (2004).

The calculation of the heat flux from the images was carried out in MatLab. Unfortunately MatLab does not support the direct usage of Raw file images without the image structure code and compression code which Canon Australia would not provide stating that it “was not for public disclosure”. Therefore the Canon raw files (*.CRW) from the camera were converted into TIFF file images.

Tagged Image Files Format (TIFF or TIF) are the standard for many digital images. Described within Wikipedia.org, the TIFF is a flexible, adaptable file format for handling images and data within a single file, by including the header tags (size, definition, image-data arrangement, applied image compression) defining the image's geometry. Adobe Systems, now holds the copyright to the TIFF specification which is widely supported by many image-manipulation applications. Most TIFF images and readers remain based upon uncompressed 32-bit CMYK or 24-bit RGB images. The use of TIFF to store images acquired using scientific CCD cameras can provide up to 16 bits per pixel of intensity resolution.

The commercially available *Raw Image Converter 2* software from Canon Australia was used for converting the Raw-images to Tiff file format. The 12 bit per channel CRW files were converted to 16 bit per channel TIFF format. This expansion was required because TIFF did not support 12 bit images. The chosen conversion was achieved without loss of data, as would have occurred were the 8 bit/channel TIFF format to have been selected. The expansion conversion essentially creates the missing pixels by interpolation between adjoining pixels. Unsigned integer 16 bit images were therefore produced which provided a pixel depth (bit count) of up to 65,536.

The conversion processing was conducted using “shot settings”, thereby not changing the white balance, sharpness or colour biasing within the image. Linear conversion was also selected so that no ‘gamma correction’ was applied to the image.

5.5.3 Background Light and Measurement Noise

To correctly scale the measurement of light from the heat flux illumination on the fibre board platform, the background light and sensor noise needed to be taken into consideration. The background light was measured by recording an image of the platform before each experiment with the radiation beam turned off. The measurement noise (dark noise) was measured by taking an image with no light coming into the lens, for example with the lens cap on.

Because the background image also includes the dark noise, only the background image had to be subtracted from the desired heat flux image. The camera settings and position remained the same for both the background images and the heat flux images so that direct pixel level subtraction could occur. The time between recording the background image and recording the heat flux image was kept as small as possible.

5.5.4 Image Intensity Adjustment

Lambert's Cosine Law in Optics states that “the radiant intensity observed from a *Lambertian* surface is directly proportional to the cosine of the angle θ between the observer's line of sight and the surface normal”. This concept is shown in Figure 5-18; where dA is the area of interest and $d\Omega$ is the solid angle subtended by the aperture from the viewpoint of the emitting area element. In the case of these experiments, the area of the photoelectric sensor and the area of the illumination were assumed the same and therefore cancel. The solid

angle $d\Omega$ was also assumed equivalent and therefore cancel. The angle θ between the ceramic fibre board and the camera lens was measured as 45° from the normal of the platform board.

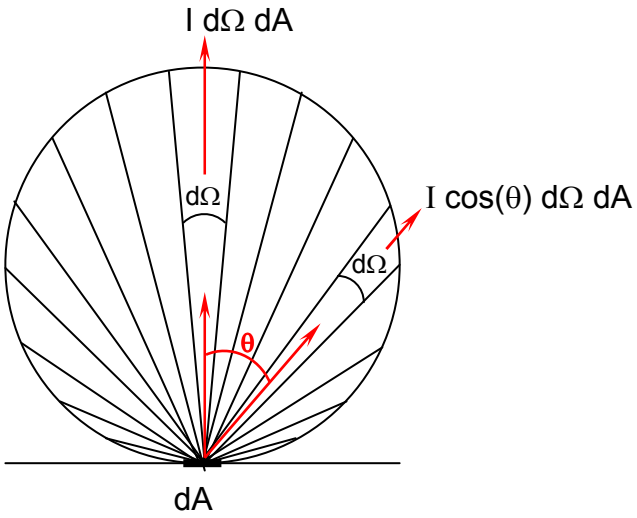

Figure 5-18: Diagram showing observed intensity from a Lambertian surface for a normal and off-normal observer.

The intensity of the heat flux normal to the board can be written as:

$$I_{Measured} = I_n \times Cos(\theta) \qquad [5.7]$$

Where: I_n is the irradiation normal to the surface.

$I_{measured}$ is the measured intensity

θ is the angle of the photoelectric sensor to the surface normal, 45°

Each pixel value for each image was therefore divided by cos(45°) to calculate the total irradiation normal to the board.

5.5.5 Image Perspective Transformation

The visual perspective of each image was also adjusted to display the heat flux intensity profile on the ceramic fibre board as seen from above. The transformation accounts for the linear perspective which caused the circular shape of the profile to become ellipsoidal.

The images were processed using a MatLab code specifically written for this application. The transformation involved taking two images of a geometric grid pattern, one at the 45° angle of the heat flux measurements and the second, normal to the surface of the grid (called

the base image). The two images were taken at the same distances as each other and at the same distance as the heat flux measurements. The 'Control Point Selection Tool' within the 'Image Processing Toolbox' of MatLab, was used to select four pairs of control points, one for each corresponding corner of each grid. The control point pairs infer the spatial transformation within '*cp2tform*' using the '*projective*' transformation. The control point transformation was then used within '*imtransform*' to apply the two dimensional spatial transformation using '*bicubic interpolation*' to the desired image.

5.5.6 Image Processing Program

MatLab Version 6.5 Release 13 and MatLab Image Processing Toolbox, Version 3.2 by MathWorks were used for processing the images. A 'head file' program was written to import the image of interest, transform the data, calculate and then display the energy intensity profile within the captured image. Calibration of the energy intensity to the measured heat flux was then carried out.

The head file for the image processing was structured as follows:

1. Import the 'Image-of-interest'.
2. Import the corresponding 'Background' image.
3. Find the maximum level pixel of all images.
4. Divide the images into its three colour components, Red Green and Blue.
5. Subtract the Background image from the Image-of-interest.
6. Adjust the pixel intensity to account for the angle of the camera. Intensity adjusted using Lambert's Law, cos(45°) factor higher than the measured intensity.
7. Transform (morph) the image to account for the visual perspective.
8. Crop image to remove unnecessary surrounding background.
9. Display and save processed image.

The energy intensity displayed within the processed image could then be quantified using the calibration measurements of heat flux.

5.5.7 Calibration of Image to Heat Flux

The calibration of the digital images involved measuring the maximum heat flux using the total heat flux transducers at a particular distance from the focal point and comparing it with the maximum pixel level at that same distance. Using the same camera position and settings, the heat flux could then be measured at any distance from the focal point by comparing scaled calibration level with the measured pixel level. This method assumes a directly proportional linear relationship, between pixel level and light intensity striking the sensor.

This method of calibration evolved from several other methods which were tried during this research investigation. These other methods are not discussed in detail here, other than to say that they were time consuming, due to the number of measurement locations, and computationally difficult, due to the amount of data collected which needed to be sorted and analysed.

To achieve the goal of maintaining the same camera settings for both the high intensity heat fluxes (close to the focal point) and at an intensity where the heat flux transducers could be used, many images where taken and subsequent processing conducted. The two camera settings which provided adequate coverage over the entire intensity range are shown in Table 5-15.

Table 5-15: Camera settings used for the calibration and measurement of the heat flux intensity.

Camera Setting	Shutter Speed (seconds)	Aperture Stop
A	1/60	22
B	1/90	22

The calibration measurement plane which best provided a reasonable pixel count in addition to producing a reasonable heat flux transducer measurement, was 525mm from the focal point. At this location the maximum heat flux measured by the transducers was 17.166 kW/m^2.

The two pixel level images of the ceramic fibre board at the 525mm location after processing are seen in Figures 5-19 and 5-20. The maximum pixel level for Figure 5-19 (camera setting **A**) was 2413 and for Figure 5-20 (camera setting **B**) was 1869.

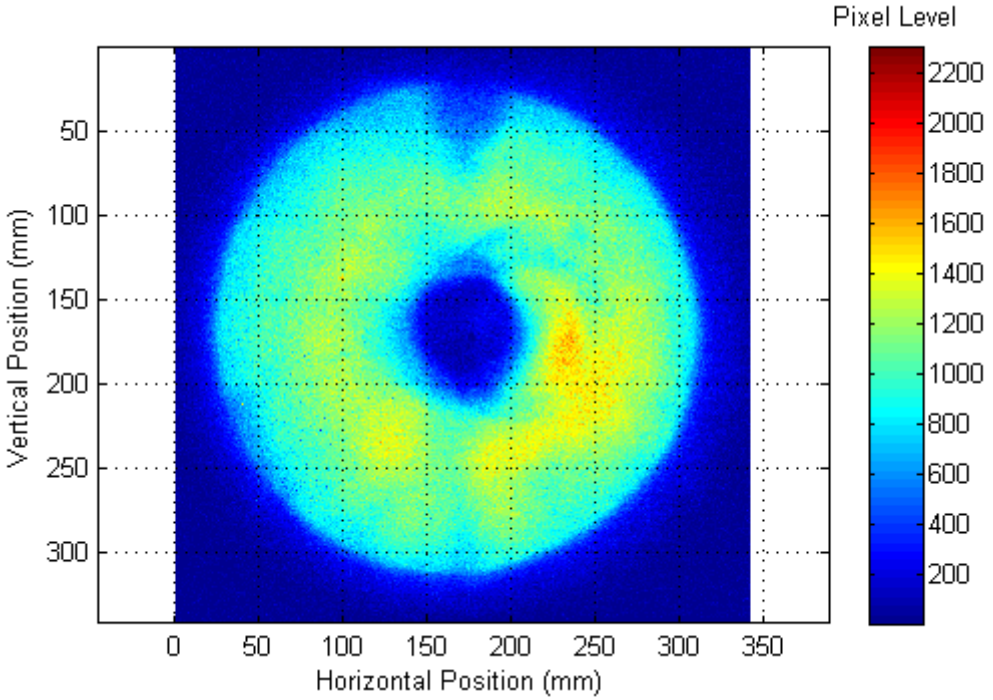

Figure 5-19: Calibration pixel gradient of illumination at 525mm from focal point using 1/60 shutter speed and 22 aperture stop.

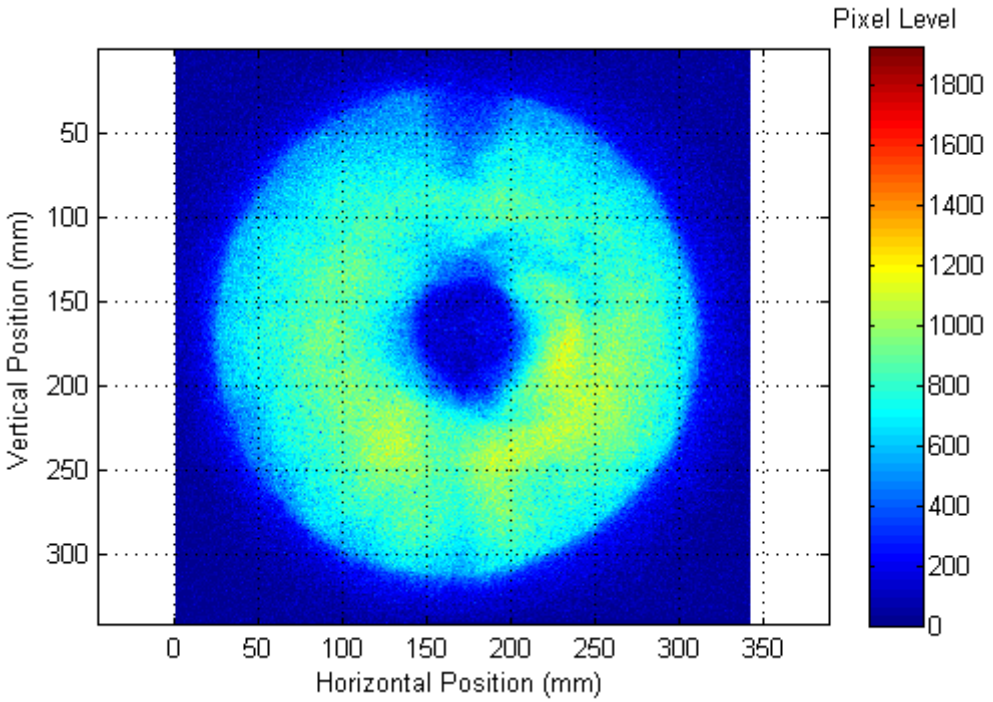

Figure 5-20: Calibration pixel gradient of illumination at 525mm from focal point using 1/90 shutter speed and 22 aperture stop.

To equate the pixel level with the measured heat flux Equation [5.8] was used.

$$\dot{q} = \mathrm{I}_{measured} \times \left(\frac{\dot{q}_{calibration}}{\mathrm{I}_{calibration}} \right) + \dot{q}_{ambient} \qquad [5.8]$$

Where: $\dot{q}$ is the calculated heat flux

$I_{measured}$ is the bit level of each pixel within the image

$\dot{q}_{calibration}$ is **17.166** kW/m^2

$I_{calibration}$ is either **2413** or **1869**, for the 1/60 or 1/90 camera shutter speed respectively

$q_{ambient}$ is the ambient light measured within the laboratory = 0.084 kW/m^2

It should be noted that two different pixel levels are used within the calibration equation depending upon the camera settings used.

5.5.8 Calculation of Heat Flux at the Near Focal Region

Images of the ceramic fibre board were taken at locations closer to the focal point. The images where then processed using the methods described previously with the calibration equation being used to convert the pixel levels to heat flux. Table 5-16 shows the calculated maximum heat fluxes for various distances from the focal point and for the two different shutter speeds.

Table 5-16: Calculated heat flux between S = 100mm and S = 30mm using two different camera shutter speeds.

Distance from Focal Point "S" mm	**Shutter Speed (seconds)**	**Calculated Maximum Heat flux $q_{max,90}$ kW/m^2**	**Shutter Speed (seconds)**	**Calculated Maximum Heat flux $q_{max,60}$ kW/m^2**	**Difference between measurements $\frac{q_{max,90} - q_{max,60}}{q_{max,60}}$ (%)**
100	1/90	166.8	1/60	180.3	- 7.44
90	1/90	197.6	1/60	216.7	- 8.84
80	1/90	250.7	1/60	255.7	- 1.96
70	1/90	292.3	1/60	316.2	- 7.57
60	1/90	363.5	1/60	377.9	- 3.82
50	1/90	429.0	1/60	454.9	- 5.70
40	1/90	550.7	1/60	549.2	+ 0.26
30	1/90	708.7	1/60	Saturation	-

As can be seen within Table 5-16, there is a difference in calculated heat flux between the two shutter speeds. The maximum difference is 8.8% for the 90mm case. These differences are thought to be due to measurement errors which are discussed later in this chapter. The calculated heat flux values for each distance from the radiation beam focal point are displayed graphically in Figure 5-21.

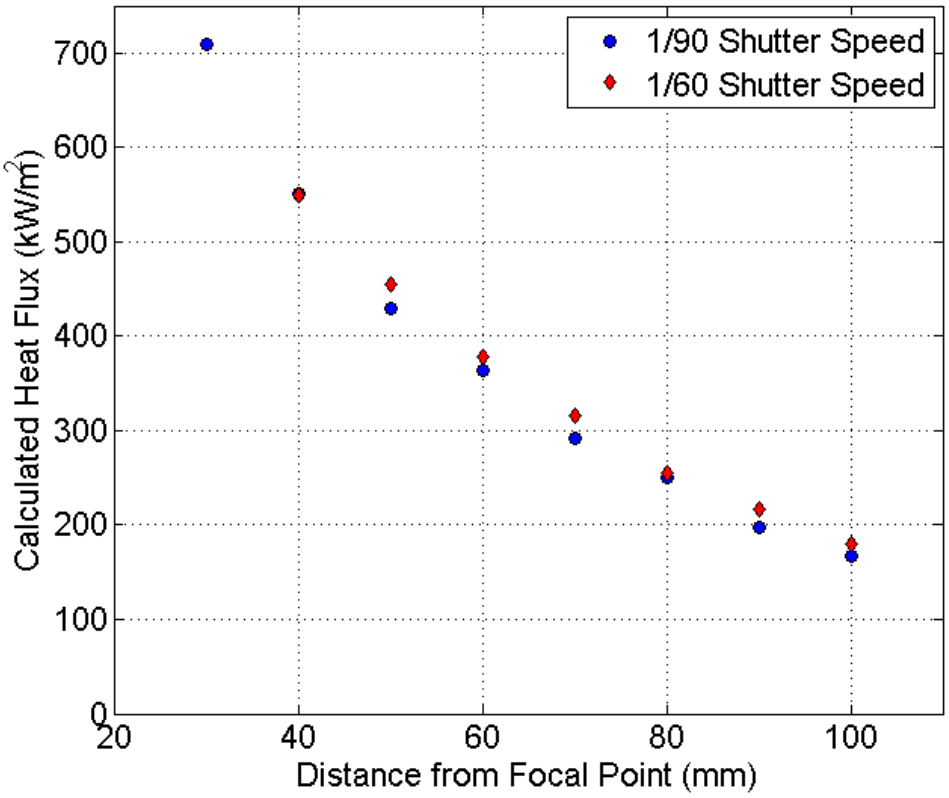

Figure 5-21: Plot of the calculated heat fluxes for distances of 100mm to 30mm from the focal point using two different camera shutter speeds.

Figures 5-22 and 5-23 show the calculated heat flux profile for the 100mm measurement location. Figure 5-22 is the original digital image displaying the heat flux profile which was calculated through the image processing technique. Figure 5-23 shows the isorad contour image of the heat flux profile. The isorad were set at 20 kW/m^2 intervals. These figures show that the illumination spot was approximately 70mm in diameter. A crescent of high heat flux is shown to the right of the profile with the maximum located immediately right of the centre. To the left of centre, there is a region of relatively even heat flux with a heat flux of approximately 100 kW/m^2. Also seen are lines radiating at 45° intervals from the centre of the profile. These lines were drawn onto the ceramic fibre board using a lead pencil to visually identify the location of the centre of the board.

Figures 5-24 and 5-25 show the calculated heat flux profile for the 50mm measurement location. The isorad contour image of the heat flux profile was set to have a 50 kW/m^2 interval. The figures show that the illumination spot was approximately 35mm in diameter. The kidney shaped crescent of high heat flux is right of the centre of the image.

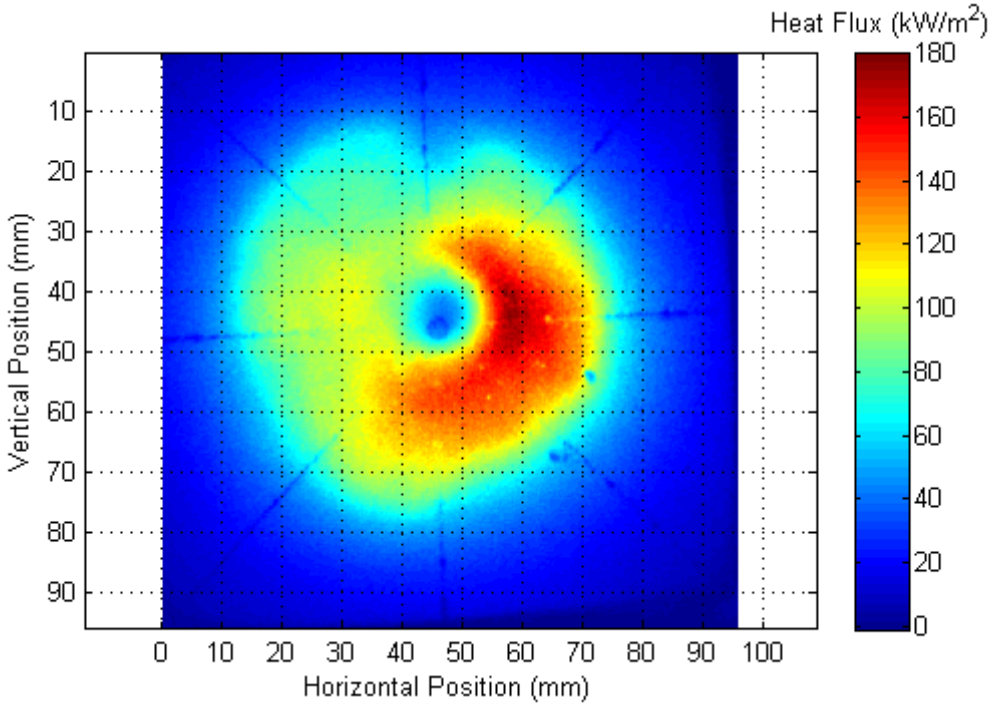

Figure 5-22: Measured heat flux distribution at S = 100mm from the focal point using a shutter speed of 1/60.

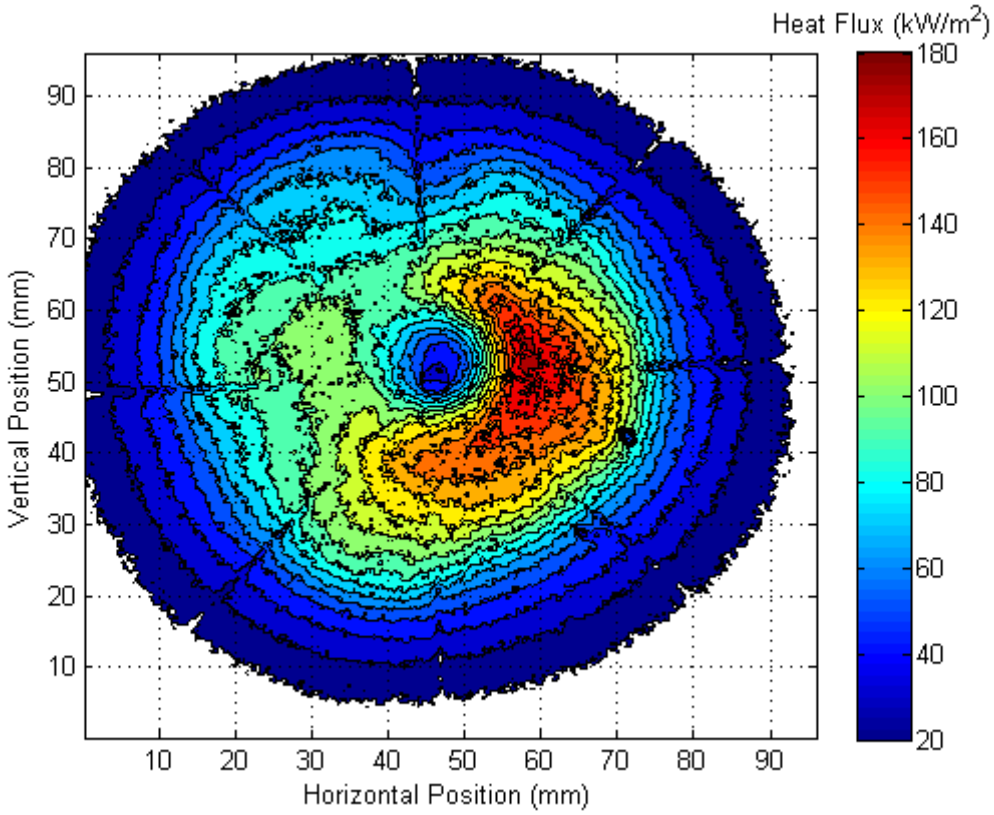

Figure 5-23: Calculated isorad contour image at S =100mm from the focal point using a shutter speed of 1/60.

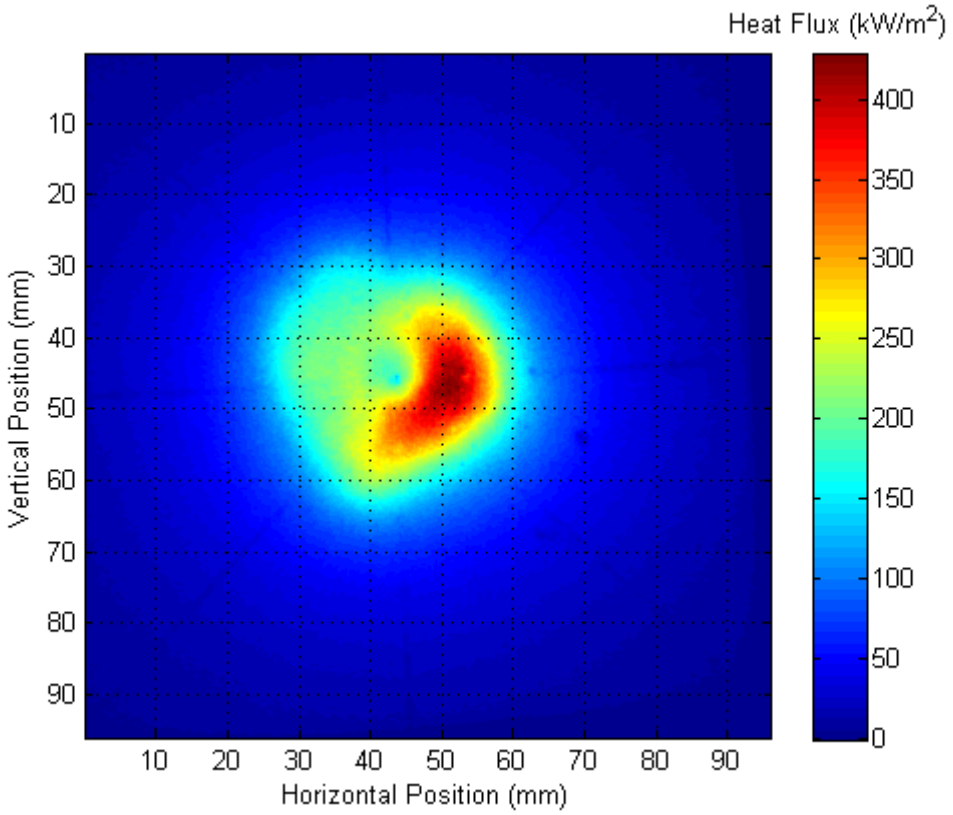

Figure 5-24: Measured heat flux distribution at S = 50mm from the focal point using a shutter speed of 1/90.

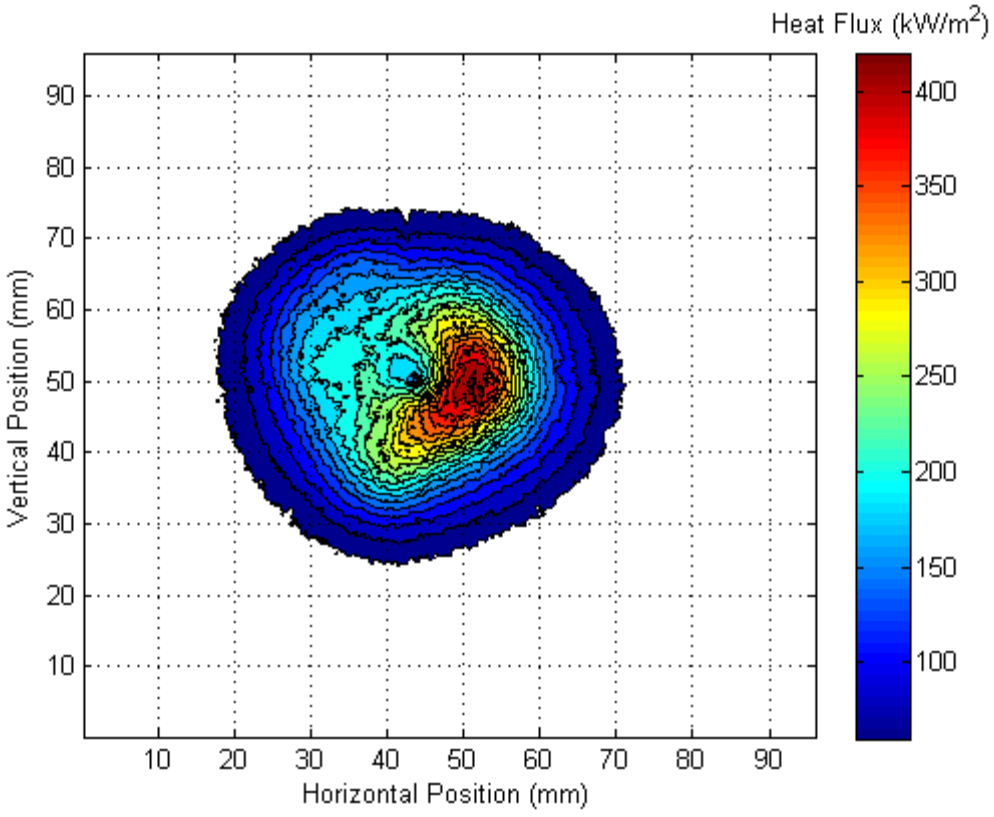

Figure 5-25: Calculated isorad contour image at S = 50mm from the focal point using a shutter speed of 1/90.

5.5.9 Error Analysis for Digital Imagery

The measurement accuracy from the transducers is discussed in detail in Section 5.5.4. The uncertainty in the measurement is approximately ± 3% resulting in a maximum difference of ± 515 W/m^2 for a 17.166 kW/m^2 measurement.

The accuracy in the measurement distance, S, from the focal point of the radiation beam to the transducer plane was estimated to be approximately ± 5 mm which could cause a difference of approximately ± 265 W/m^2 or ± 1.6% in the measurement.

There was also a discrepancy in the measurement distance from the focal point to the ceramic fibre target board. It is estimated that the accuracy in this measurement distance was ± 3 mm. For the 525mm measurement this discrepancy represents ± 0.6% in the measured pixel level (remembering that the pixel level is directly proportional to the light intensity from the board, Equation [5.6]). This variation causes the equivalent percentage change in the calibration equation which in turn varies the 'calibrated' heat flux at the other distances to have a variation of ± 0.6%. For the 100mm distance case this represents 717 W/m^2 and for the 50mm distance case represents 1839 W/m^2.

Following on from the target board distance discrepancy above, is the error produced by the inconsistency of the distance between the camera and the centre of the target board for different measurement heights. While all due care was taken to maintain the 985mm distance it is estimated that there was variation of approximately ± 5 mm. This distance difference results in a possible pixel level variation of ± 1%, using Equation [5.8]. For the 525mm measurement this discrepancy represents 135 W/m^2, for the 100mm distance case this represents 1195 W/m^2 and for the 50mm distance case represents 3064 W/m^2.

The 45° angle of camera to target board was measured manually, with an estimated accuracy of ± 0.5°. Using Equation [5.7], the variation of the image intensity adjustment equates to approximately 0.43%, which for the 525mm measurement is 18 W/m^2, 160 W/m^2 for the 100mm measurement and 407 W/m^2 for the 50mm measurement.

Two additional sources of error exist using this measurement technique. 1) The calibration system depends on a single heat flux measurement and equates it with a single pixel level measurement, and 2) the maximum background noise is approximately one quarter of the maximum pixel level for the calibration measurement. These sources are because of the limited operating range of the heat flux transducers and the variation in the response of the

CMOS sensor. It was established by comparing two images of the same location using the same camera settings, that a difference of up to 8.4% was possible between the maximum pixel levels. The maximum error here can cause a difference of up to 1138 W/m^2 in the 525mm measurement, 10.0 kW/m^2 in the 100mm measurement and 25.7 kW/m^2 in the 50mm measurements. It is recommended that a large number of images be taken for each measurement location. The images could then be overlaid and the root mean squared of each pixel location be calculated. This averaging would smooth out the inconsistencies which can occur.

Table 5-17 shows a summation of all the above errors, should the "worst case" in the measurements occur.

Table 5-17: Maximum possible variation in the digital imagery heat flux measurements.

Nominal Optical Path Length S (mm)	**Possible Difference in heat flux W/m^2**	**Percentage Difference**
525	± 2,071	± 12.06 %
100	± 14,875	± 8.25%
50	± 31,044	± 7.24%